

NEW SPATIO-TEMPORAL HAWKES PROCESS MODELS FOR SOCIAL GOOD

by

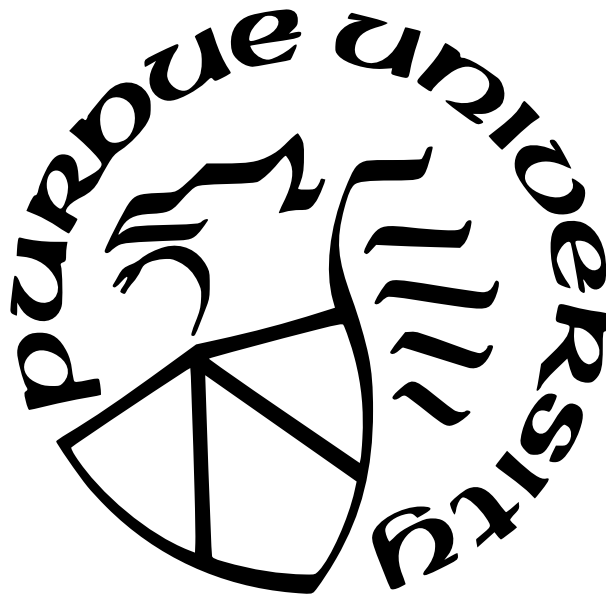
Wen-Hao Chiang

A Dissertation

Submitted to the Faculty of Purdue University

In Partial Fulfillment of the Requirements for the degree of

Doctor of Philosophy



Department of Computer and Information Science

Indianapolis, Indiana

May 2022

**THE PURDUE UNIVERSITY GRADUATE SCHOOL
STATEMENT OF COMMITTEE APPROVAL**

Dr. George Mohler, Chair

Department of Computer and Information Science

Dr. Mohammad Al Hasan

Department of Computer and Information Science

Dr. Murat Dundar

Department of Computer and Information Science

Dr. Jeremy Carter

Paul H. O'Neill School of Public and Environmental Affairs

Approved by:

Dr. Shiaofen Fang

ACKNOWLEDGMENTS

I would like to express my gratitude to my primary supervisor, George Mohler, who guided me throughout my projects and each stage of the process. He has been very helpful to offer valuable suggestions from the brainstorming of the research problem, algorithm design and the analysis of the experimental results. Without his kindness and invaluable assistance, it would have been impossible for me to finish this journey to the Ph.D. degree. I would also like to thank my committee members, Dr. Mohammad Al Hasan, Dr. Murat Dundar, Dr. Snehasis Mukhopadhyay and Dr. Jeremy Carter for all of their help and suggestions especially in my preliminary exam. I also wish to thank the collaborators whose assistance was crucial in the completion of each of the projects. I would like to acknowledge the support and great love from my family and friends, my significant other Seth, my mother Mei-Chin, my father Ming-Tsao, my sister Yi-Han, my cat Zeus and the many Ph.D. students in our program. They encouraged me and kept me motivated and this thesis would not have been achievable without their help. I wish to extend my special thanks to my previous advisor Dr. Xia Ning in my first two Ph.D. years. Without the training in her team, I wouldn't be able to build a strong background knowledge in this field.

TABLE OF CONTENTS

LIST OF TABLES	8
LIST OF FIGURES	9
ABSTRACT	11
1 INTRODUCTION	13
1.1 Motivation	13
1.1.1 Early Warning for Overdose Spike	13
1.1.2 Search and Rescue Resource Management	14
1.1.3 Forecasting of Pandemic Spread	16
2 BACKGROUND	19
2.1 A Brief Review of Hawkes Processes	19
2.1.1 Multi-variate Hawkes Processes	20
2.1.2 Spatio-temporal Hawkes Processes	20
2.1.3 Model Inference	21
2.2 A Brief Review of Multi-armed Bandit Problems	22
3 SOS-EW: SYSTEM FOR OVERDOSE SPIKE EARLY WARNING USING DRUG MOVER’S DISTANCE-BASED HAWKES PROCESSES	26
3.1 Method	27
3.1.1 Related Work	27
3.1.2 Overdose Categorization	28
3.1.3 Spatio-temporal Hawkes Process	31
3.2 Comparison Methods	32
3.2.1 Non-parametric Hawkes Processes: SimpHP	33
3.2.2 Spatial-temporal Hawkes Processes: SpatHP	33
3.2.3 Dirichlet Hawkes Processes: SpatHP	33
3.3 Experiments	34

3.3.1	Data	34
3.3.2	Evaluation Protocols and Metrics	35
3.3.3	Experimental Results	38
3.4	Implications for Practice	39
4	HAWKES PROCESS MULTI-ARMED BANDITS	41
4.1	Methodology	41
4.1.1	Problem Formulation	41
4.1.2	Theoretical Expected Number of Events	42
4.1.3	Construction of Upper Confidence Bound on Future Expectation	43
4.1.4	Regret Analysis of HpUCB	44
4.2	Experiments	48
4.2.1	Baseline Methods	48
4.2.2	Datasets	49
	Temporal Synthetic Data (\mathcal{D}_{SIM}):	49
	Records of Worldwide Earthquakes ($\mathcal{D}_{\text{EARW}}$):	49
	Records of Earthquakes in Alaska and California ($\mathcal{D}_{\text{EACA}}$):	49
	Records of Crime Activities in Vancouver (\mathcal{D}_{VAN}):	50
	Records of Crime Activities in Los Angeles (\mathcal{D}_{LA}):	50
4.2.3	Reward Performances	50
5	HAWKES PROCESS MULTI-ARMED BANDITS FOR SEARCH AND RESCUE	54
5.1	Methodology	54
5.1.1	Spatio-temporal MAB Problem Formulation	54
5.1.2	Hawkes Process Multi-armed Bandits	55
5.1.3	Spatial Upper Confidence Bound on Event Intensities	56
5.1.4	Combining Hawkes Process Bandits with Existing Methods	57
5.2	Experiments	59
5.2.1	Datasets	59
	Spatial-temporal Synthetic Data (\mathcal{D}_{Syn}):	59
	City of Houston 311 Service Requests (\mathcal{D}_{Hry}):	60

	Reports of IED attack in Iraq (\mathcal{D}_{IED}):	61
5.2.2	Experimental Protocol	61
5.2.3	Evaluation Metrics	62
5.2.4	Experimental Results	63
	Performances on the Synthetic Datasets \mathcal{D}_{syn} :	63
	Performances on Houston 311 Service Requests \mathcal{D}_{Hry} :	64
	Performances on IED Attack Reports \mathcal{D}_{IED} :	67
5.3	Conclusion	67
6	HAWKES PROCESS MODELING OF COVID-19 WITH MOBILITY LEADING INDICATORS AND SPATIAL COVARIATES	69
6.1	Hawkes Process Model of COVID-19 Transmission	69
6.1.1	Incorporating Covariates into the Hawkes Process	69
6.1.2	Mathematical Connection between Hawkes Processes and Compartmental Models	70
6.1.3	EM Algorithm for Parameter Inference	72
	Expectation Step	73
	Maximization Step	74
6.1.4	Connection of EM algorithm for Hawkes Process and Dynamic R estimator of Wallinga and Teunis	76
6.1.5	Hawkes Process Forecasting	78
6.2	Experiments and Results	78
6.2.1	Datasets	78
	Covid-19 Daily Cases and Deaths Reported by The New York Times	78
	Google Mobility Index Reports	80
	County-level Demographic Covariates	81
6.2.2	Baseline Models and Experimental Setup for Retrospective Forecasting Comparison	82
6.2.3	Experimental Results	83
	Importance of Covariates	87

COVID-19 Forecasting and Reproduction Number Analysis	88
Example of Estimated Event Intensities and Weekly Forecasts	90
Dynamic Background Rate μ_c Modeling	90
6.2.4 State-level Comparison to COVID-19 Forecast Hub	92
Weighted Interval Score WIS	93
Selection Criteria and Comparison Results	93
6.3 Conclusion	95
7 SUMMARY	97
REFERENCES	102
VITA	116
PUBLICATIONS	117

LIST OF TABLES

1.1	Changes for each model based on the application	18
3.1	Statistics on Overdoes Event	35
3.2	Overall Performance on Different Spike Window Size w	38
3.3	Overall $NDCG$ Performance	39
4.1	Simulation Dataset \mathcal{D}_{Tem}	51
4.2	Best Performance on Earthquake in Worldwide $\mathcal{D}_{\text{EARW}}$	51
4.3	Earthquake in AK and CA $\mathcal{D}_{\text{EACA}}$	52
4.4	Crime Activities in Vancouver \mathcal{D}_{VAN}	52
4.5	Crime Activities in Los Angeles \mathcal{D}_{LA}	52
5.1	Best Performance on \mathcal{D}_{Hry}	64
5.2	Best Performance on \mathcal{D}_{IED}	67
6.1	MAE on predicted confirmed cases $\mathcal{D}_{\text{conf}}$	83
6.2	MAE on predicted confirmed cases $\mathcal{D}_{\text{death}}$	84
6.3	PE on predicted confirmed cases $\mathcal{D}_{\text{conf}}$	84
6.4	PE on predicted confirmed cases $\mathcal{D}_{\text{death}}$	85
6.5	$NDCG$ on predicted confirmed cases $\mathcal{D}_{\text{conf}}$	86
6.6	$NDCG$ on predicted confirmed cases $\mathcal{D}_{\text{death}}$	86
6.7	Model coefficients ($\mathcal{D}_{\text{conf}}$)	87
6.8	Model coefficients ($\mathcal{D}_{\text{death}}$)	87
6.9	Performance and improvements of \mathbf{HkPR}_{μ} on $\mathcal{D}_{\text{conf}}$ and $\mathcal{D}_{\text{death}}$	92
6.10	Relative \mathbf{WIS} and \mathbf{MAE} on the JHU dataset	95

LIST OF FIGURES

3.1	Overview of the SOS – EW system for early warning of opioid spikes. The initial overdose toxicology report shows fentanyl, benzodiazepine, and heroin present. Each drug is vectorized using SMILES and the event is assigned an overdose category using spectral clustering based on earth mover’s distance of the drug vectors (“drug mover’s distance”). The increase in the intensity of the Hawkes process is determined by the category and allows for the prediction of an opioid overdose spike, those events triggered in the branching process by the initial overdose.	26
3.2	Gephi visualization of graph used for spectral clustering (edges correspond to adjacency weight greater than .9) and the most frequent drugs in each of the 5 overdose categories.	30
3.3	Number of Events per Year	35
3.4	An illustration for an initial event and its triggered events in one of the categories (i.e., one of the Hawks processes). The initial overdose event marked in triangle symbol consists of four drug substances and it triggered four neighboring events consisting of different number of drug substances respectively.	36
4.1	Expected number of events at the 2000 th round ($d = 2000$) from a simulated Hawkes processes dataset. We use the sets of estimated parameters from $j = 1$ to $j = 1999$ to calculate the expect number of events at round 2000 and plot out the histogram. The distribution pass the D’Agostino and Pearson’s normality test with a p-value of 1.07×10^{-97}	43
4.2	Cumulative rewards of records of worldwide earthquakes $\mathcal{D}_{\text{EARW}}$	53
4.3	Cumulative earthquake rewards of records in AK CA $\mathcal{D}_{\text{EACA}}$	53
5.1	Top-20 clusters in \mathcal{D}_{syn} . Different clusters are color-coded and the parameters under this simulation are $T = 3.6 \times 10^6$ seconds, $\eta = 8 \times 10^{-5}$, $\phi = 0.99$, $\omega = 10^{-4}$ and $\sigma = 10^{-2}$	60
5.2	Flooding Events in Houston \mathcal{D}_{Hry} . Each event is scaled and color-coded by its timestamps, and x-axis and y-axis represents the grid cell ID.	61
5.3	Performance on $\overline{\text{reward}}$ on \mathcal{D}_{syn} under different simulation scenarios with various of ω, ϕ and σ . We run simulations by changing only one of the parameters at a time and the other parameters, i.g., ω, ϕ and σ , are fixed at $10^{-4}, 0.99$ and 10^{-2} , respectively.	64
5.4	Number of events	65
5.5	Number of visits	65
5.6	Map on (4,1)	66

6.1	(Main figure) The red plot shows new infections (μE) from the SEIR differential equation $\frac{dS}{dt} = -\beta \frac{SI}{N}$, $\frac{dE}{dt} = \beta \frac{SI}{N} - \mu E$, $\frac{dI}{dt} = \mu E - \gamma I$, $\frac{dR}{dt} = \gamma I$, where $\beta = \gamma R_0$, $\gamma = .1$, $R_0 = 2$, $\mu = 1$, and $N = 5 \cdot 10^8$. The blue squares show the linear Hawkes process $\lambda_t = \mu + \sum_{t > t_i} R_0 w(t - t_i)$ fit to the SEIR curve of new infections. Inset: Non-parametric histogram estimate for $w(t)$	72
6.2	Distribution of cumulative cases reported at 11/30/2020 at different quantiles.	79
6.3	Example of the daily # of confirmed cases/deaths.	80
6.4	Heat map of mobility indices across counties in $\mathcal{D}_{\text{conf}}$ and over time.	81
6.5	Examples of spatial demographic and health features at the county-level.	82
6.6	Forecasting for 28 days from 10/28/2020 - 11/25/2020	88
6.7	Estimated R of confirmed cases $\mathcal{D}_{\text{conf}}$ and lagged mobility changes ($\Delta = 14$ days)	89
6.8	Estimated R of deaths $\mathcal{D}_{\text{death}}$ and lagged mobility changes ($\Delta = 21$ days)	89
6.9	Example of the fitted effect from mobility and demographics	91
6.10	Example of the weekly forecasts	91

ABSTRACT

As more and more datasets with self-exciting properties become available, the demand for robust models that capture contagion across events is also getting stronger.

Hawkes processes stand out given their ability to capture a wide range of contagion and self-excitation patterns, including transmission of infectious disease, earthquake aftershock distributions, near-repeat crime patterns, and overdose clusters. The Hawkes process is flexible in modeling these various applications through parametric and non-parametric kernels that model event dependencies in space, time and on networks. In this thesis, we develop new frameworks that integrate Hawkes Process models with multi-armed bandit algorithms, high dimensional marks, and high-dimensional auxiliary data to solve problems in search and rescue, forecasting infectious disease, and early detection of overdose spikes.

In Chapter 3, we develop a method applications to the crisis of increasing overdose mortality over the last decade. We first encode the molecular substructures found in a drug overdose toxicology report. We then cluster these overdose encodings into different overdose categories and model these categories with spatio-temporal multivariate Hawkes processes. Our results demonstrate that the proposed methodology can improve estimation of the magnitude of an overdose spike based on the substances found in an initial overdose.

In Chapter 4, we build a framework for multi-armed bandit problems arising in event detection where the underlying process is self-exciting. We derive the expected number of events for Hawkes processes given a parametric model for the intensity and then analyze the regret bound of a Hawkes process UCB-normal algorithm. By introducing the Hawkes Processes modeling into the upper confidence bound construction, our models can detect more events of interest under the multi-armed bandit problem setting. We apply the Hawkes bandit model to spatio-temporal data on crime events and earthquake aftershocks. We show that the model can quickly learn to detect hotspot regions, when events are unobserved, while striking a balance between exploitation and exploration.

In Chapter 5, we present a new spatio-temporal framework for integrating Hawkes processes with multi-armed bandit algorithms. Compared to the methods proposed in Chapter 4, the upper confidence bound is constructed through Bayesian estimation of a spatial

Hawkes process to balance the trade-off between exploiting and exploring geographic regions. The model is validated through simulated datasets and real-world datasets such as flooding events and improvised explosive devices (IEDs) attack records. The experimental results show that our model outperforms baseline spatial MAB algorithms through rewards and ranking metrics.

In Chapter 6, we demonstrate that the Hawkes process is a powerful tool to model the infectious disease transmission. We develop models using Hawkes processes with spatial-temporal covariates to forecast COVID-19 transmission at the county level. In the proposed framework, we show how to estimate the dynamic reproduction number of the virus within an EM algorithm through a regression on Google mobility indices. We also include demographic covariates as spatial information to enhance the accuracy. Such an approach is tested on both short-term and long-term forecasting tasks. The results show that the Hawkes process outperforms several benchmark models published in a public forecast repository. The model also provides insights on important covariates and mobility that impact COVID-19 transmission in the U.S. Finally, in chapter 7, we discuss implications of the research and future research directions.

1. INTRODUCTION

1.1 Motivation

1.1.1 Early Warning for Overdose Spike

Criminology and public health disciplines have leveraged spatio-temporal event modeling in attempts to predict social harm for effective interventions [1]–[3]. Fifty percent of crime has been shown to concentrate within just 5 percent of an urban geography [4]. Geographic concentrations of drug-related emergency medical calls for service [5], drug activity [6], and opioid overdose deaths mirror those of crime [7]. Patterns of repeat and near-repeat crime in space and time further suggest that not only does crime concentrate in place but that such events are an artifact of a contagion effect resulting from an initiating criminal event [8]. Similar observations have also explained the diffusion of homicide events [9]. Experiments of predicting policing models using spatio-temporal Hawkes and self-exciting point processes demonstrates that such empirical realities can be harnessed to direct police resources to reduce crime [10]. Thus, the inter-dependence and chronological occurrence of event types in crime and public health lend promise to how to best predict other social harm events, such as opioid overdoses.

The United States is experiencing an overdose epidemic with more than a half million drug overdose deaths since 2000 and over 70,000 drug overdose deaths in 2017 alone [11]. A majority of these deaths have been opioid-related overdoses; however, the role of opioids has varied dramatically across three waves of the epidemic, each resulting in increasing death rates [12]. This first wave began in the 1990s and was driven by prescription opioid-related deaths [13]. The reduced availability of these prescription medications is said to have resulted in the second wave of the epidemic, which began in 2010, and was driving by heroin-related deaths [13]–[15]. The third wave started in 2013 and has largely been driven by illicit fentanyl, a synthetic opioid that is 50 to 100 times more potent than morphine [16]. National estimates suggest that in 2016 nearly half of opioid-related deaths contained fentanyl [17], and there is evidence showing that fentanyl is being mixed into heroin and cocaine which is likely contributing overdose deaths involving these substances [18], [19].

Recent research has also shown that opioid overdoses cluster in space and time, where over half of opioid overdose deaths may occur in less than 5% of a city [7].

As the overdose epidemic has progressed researchers and policy makers have revealed shortcomings in official data sources, namely vital records data. One limitation is that vital records data rely on the International Classification of Diseases, 10th Revision (ICD-10) codes which do not record the specific substances related to an overdose fatality [20]–[23]; for example, there is no ICD code for fentanyl. Another limitation though has been the undercounting of opioid-related fatalities as 20 to 35 percent of drug overdose deaths are unspecified [24], meaning no substance was indicated as a primary or contributing cause of death. Moreover, rates of undercounting vary geographically as they are the result of state policies for death investigation procedures [24]. While researchers have developed measures to adjust for these limitations [24], better data collection systems are being implemented [25], and state policies are changing [26], it remains clear that we lacked sufficient data to quickly detect and identify the substances driving this overdose epidemic at the national level. However, one source of local information that can be used to address these gaps are toxicology results collected as part of an overdose death investigation. Our goal in the present work is to develop a statistical framework for modeling and prediction of opioid overdose clusters in space and time, leveraging information provided in the toxicology report of the initial overdose in the cluster.

1.1.2 Search and Rescue Resource Management

There are a variety of scenarios where a sequential set of decisions is made, each followed by some gain in information, that allows us to refine our future decisions or “strategies”. Often this information may come in the form of a reward or payoff (that may be negative). Examples of such scenarios include online advertising [27] where spending can occur in a known, profitable channel or in a new, possibly better channel, personalized recommendations [28], [29] of a past product purchase or a new, possibly better product, and clinical trials [30] between an established drug and a new treatment. In each of these cases a balance

must be struck between maximizing payoffs using known information on treatment units and retrieving more information from those under-sampled treatment units.

One application area where such a decision process occurs is that of disaster search and rescue. During hurricane Harvey in 2017, Houston experienced significant flooding and a number of citizens required rescue by boat. Information on when and where these rescues needed to occur resided in disparate data feeds, for example some citizens were rescued by government first responders via 911 or 311 calls, others were rescued through social media posts by the “Cajun Navy,” a volunteer rescue group [31]. During disasters, a particular dataset may be over sampled in one area and undersampled in another due to power outages, cell tower outages, demographic disparities on the use of social media, etc. For a group like the Cajun Navy who relied on under-sampled social media data, along with random search, machine learning based optimal search strategies that can adapt to spatio-temporal clustering in disaster event data would be beneficial. Similar strategies are also needed in other space-time searching scenarios, such as searching for and clearing improvised explosive devices (IED). Certain regions of a road network may be over-sampled due to previously identified or detonated devices, whereas other areas may be unknown and contain IEDs yet to be detonated.

We believe multi-armed bandits (MAB) are well suited for this task of balancing geographical exploration during disaster search and rescue vs. exploiting known, biased data on locations needing help. In the classic MAB problem setup, a gambler chooses a lever to play at each round over a planning horizon and only the reward from the pulled lever is observed. The gambler’s goal is to maximize the total reward while using some trials (with negative payoff) to improve understanding of the distribution of the under-observed levers. For the disaster search and rescue scenario, each geographic region and window of time may be viewed as a lever, where information may be known about areas previously visited or having historical data, but is not known about other areas. Here the reward is discovery of a citizen needing rescue. We note there has been past research on mining spatio-temporal disaster data. Some research has been dedicated to disaster mitigation and management in order to minimize casualties [32]. Data mining tasks include but are not limited to decision tree modeling for flood damage assessment [33], statistical model ensembles for susceptible

flood regions prediction [34], and text mining social media for key rescue resource identification [35]. However, no work to date has tackled the problem from a MAB framework. Furthermore, there are few existing spatial MAB algorithms and, to our knowledge, no MAB algorithm has been developed for data exhibiting clustering both in space and time. For this purpose, we develop the Hawkes process multi-armed bandit. The method is capable of detecting spatio-temporal clustering patterns in data, while capturing uncertainty of estimated risk in under-sampled geographical regions. The output of the model is a decision strategy for optimizing spatio-temporal search and rescue decisions.

1.1.3 Forecasting of Pandemic Spread

Mathematical modeling and forecasting are playing a pivotal role in the ongoing SARS-CoV-2 (COVID-19) pandemic. In mid-March 2020, a report out of Imperial College London [36] forecasted severe consequences in the U.S. and U.K. in the absence of significant public health interventions. In both nations, governments responded by closing schools, non-essential businesses and releasing general stay-at-home (shelter-in-place) orders. In the U.S., state and local policymakers are using mathematical models and projections to inform decisions about when and how to relax public health measures that have been put in place. By and large, compartmental models that explicitly incorporate transmission characteristics of infectious diseases have been favored over other statistical modeling approaches. High profile Susceptible-Exposed-Infected-Removed (SEIR) models include those out of the Institute for Health Metrics and Evaluation (IHME) [37], Columbia University [38], MIT [39], The Johns Hopkins University [40], and UCLA [41] (in the case of the UCLA model, an SEIR-variant with an unreported compartment is fit using least-squares to reported infection and recovery data).

Other strategies apart from SEIR models are CMU-TimeSeries ¹ and GT-DeepCOVID ². CMU-TimeSeries uses an auto-regressive time series model fit to case counts and deaths. GT-DeepCOVID is a purely data-driven approach using end-to-end deep learning models to predict mortality on a weekly basis.

¹<https://delphi.cmu.edu/>

²<https://deepcovid.github.io/>

Our goal is to show that Hawkes processes, widely used in the statistical learning community to model contagion patterns in event data, are well suited for modeling and forecasting COVID-19 case and mortality data. They have several advantages that we will highlight, including being highly flexible in accommodating auxiliary spatio-temporal features such as county-level demographics and temporal mobility patterns, yet mathematically they are connected to compartmental models [42] and allow for explicit incorporation of transmission dynamics (which we briefly review in the following section). Furthermore, extensive research has been conducted in the past several years on incorporating machine learning techniques into the point process framework. Non-parametric Hawkes processes can be constructed where the triggering kernel is learned [43] and, more recently, fully neural network based point processes have been developed [44], [45]. Sparse linear combinations of Hawkes processes were a winning solution in the 2017 NIJ Crime Forecasting Challenge [46]. In certain cases a mixture of Hawkes processes may be needed to model more complex event contagion with high dimensional marks through Dirichlet processes [47], [48]. Hawkes processes can also be used for causal inference on networks [49] and recent efforts have also focused on training point processes through reinforcement learning [50], [51]. Hawkes processes also can take as input auxiliary covariates [1], [52], [53], including spatio-temporal features to model earthquake occurrences [54]–[57] and environmental and demographic variables to model crime [1], [53]. We believe all of these methods have potential applications to modeling infectious diseases that are highly complex due to heterogeneity in the population, environment, and disparate public policies across regional and local jurisdictions. Despite these advantages, to our knowledge, the only U.S. state where a Hawkes process is being used to inform COVID-19 policy is in New Jersey (a collaboration with Facebook AI Research) ³. In this work, we develop our Hawkes process model whose productivity (reproduction number) is dynamic and depends on spatio-temporal covariates. We also investigate which covariates and mobility indices are most important for building forecasts of COVID-19 in the U.S.

³<https://ai.facebook.com/blog/using-ai-to-help-health-experts-address-the-covid-19-pandemic>

Table 1.1. Changes for each model based on the application

Model	How model changes for each application according to the applications
SOS – EW (Chapter 3)	In modeling the popularity of social media posts such as Twitter and Reddit, we can categorize the posts by topic based on the texts. In the application of modeling earthquakes, following the same framework, we can cluster the events based on their geolocation. We can replace the drug structure vector with longitude and latitude.
HpUCB (Chapter 4) and HpSpUCB (Chapter 5)	Some financial research application has also formulated the portfolio choice problems as MAB problem. In our model, the Hawkes processes component can be used to model the risk-at-value. Most recently, a line of work uses MAB to maximize influence on social media. As viral content can be infectious, our model can be applied to this type of application. The geolocation covariates can be replaced by the contexts in the content, and Hawkes process components can be used to model the popularity.
HawkPR (Chapter 6)	In infectious disease modeling, $R(t)$ depends on time t , whereas in earthquake modeling it depends on magnitude and the space-time kernel is a power law. In other application such as modeling criminal activities, the covariates can be changed to crime types and officer demographics to infer the association.

2. BACKGROUND

2.1 A Brief Review of Hawkes Processes

Given a set of N events with corresponding timestamps, t_1, t_2, \dots, t_N , we first consider a temporal point process where the set of timestamps is modeled by its conditional intensity function $\lambda(t)$. The conditional intensity function represents the rate of events happening at time t conditional on the previous event history before time t , denoted as H_t . In specific, the conditional intensity function $\lambda(t)$ is defined as follows:

$$\lambda(t) = \lim_{\Delta t \rightarrow 0} \mathbb{E} \left[\frac{N(t + \delta t) - N(t)}{\Delta t} \middle| H_t, \right. \quad (2.1)$$

where $N(t)$ is the counting process, i.e., number of events up to time t .

One type of point-process model is the Poisson process. In the Poisson process, the number of events in any time interval follows a Poisson distribution. Such Poisson process is homogeneous when its rate remains constant, i.e., $\lambda(t) = \text{constant}$. Therefore, the expected number of events to occur given a unit time is constant. When the conditional intensity function $\lambda(t)$ changes throughout the time, e.g., $\lambda(t) = e^{-t}$, such process is considered to be inhomogeneous.

We consider one specific type of inhomogeneous point process, the Hawkes process, a self-exciting point process where the occurrence of past points makes the occurrence of future points more probable. The conditional intensity function of a uni-variate temporal Hawkes process is defined as follows:

$$\lambda(t) = \mu(t) + \sum_{t_i < t} K g(t - t_i), \quad (2.2)$$

where productivity $K > 0$ is the expected number of events that are triggered by one single event. The productivity K is typically $0 \leq K < 1$ to ensure the process is stationary and stable. The background rate $\mu(t) > 0$ is to describe how the likelihood evolves through time. These characteristics are independent of the previous historical events. For example, crime events are more likely to occur during the night than during the day. The flooding

events tend to happen in the rainy season. On the other hand, the summation of $g(t - t_i)$ represents the self-excitation. The past events can increase the current intensity. Here, $g(t)$ is often referred as the triggering density and $\int_{t=0}^{\infty} g(t)dt = 1$. It describes the distribution of infectivity of an event at different times. One example is a Hawkes Process where the kernel follows an exponential distribution $g(t) = \omega e^{-\omega t}$. The influence on the intensity of each event decays exponentially and ω governs how fast the influence decays to zero.

2.1.1 Multi-variate Hawkes Processes

We consider a multivariate Hawkes process, where there are U different Hawkes processes (nodes) and we denote their conditional intensity function as $\lambda_u(t)$ ($u = 1, \dots, U$). One example is the multivariate Hawkes process with an exponential decay kernel. The intensity of such a multivariate Hawkes process takes the following form:

$$\lambda_u(t) = \mu_u(t) + \sum_{t_i < t} K_{u_i, u} g_{u_i}(t - t_i), \quad (2.3)$$

where event t_i belongs to Hawkes processes u_i and $K_{u_i, u} > 0$ is the expected number of events in u_i that are triggered by events in u . In this form, each node has its own triggering kernel, and the influence of intensity from an event depends on to which node it belongs. For simplicity, we can assume a uniform background rate in time μ_u and the spectral norm of a triggering matrix $\mathbf{K} \in \mathbb{R}^{U \times U}$ satisfy that $\|\mathbf{K}\| < 1$. The triggering kernel follows exponential decay distribution:

$$\lambda_u(t) = \mu_u + \sum_{t_i < t} K_{u_i, u} \omega e^{-\omega(t-t_i)}. \quad (2.4)$$

2.1.2 Spatio-temporal Hawkes Processes

In the real-world datasets, sometimes they don't include only just timestamps but also the corresponding spatial information, such as the longitude and latitude at which the event occurs. This information can be important for us to better understand the dynamics within the dataset. For example, a major earthquake can trigger some aftershocks, and usually, those aftershocks tend to occur in the neighboring area geographically. Moreover, when

modeling crime activity, the incidents may cluster in space due to the limited mobility of offenders and hotspots in the cities. These situations indicate that we can benefit from examining spatiotemporal point processes rather than just temporal ones. Considering a spatiotemporal point process, the conditional intensity λ is as the following:

$$\lambda(t, x, y) = \mu(x, y) + K \sum_{t > t_i} g(x - x_i, y - y_i, t - t_i). \quad (2.5)$$

In this scenario, one event is likely to trigger events locally in time and space. Choices of triggering kernel $g(t, x, y)$ include a modified Omori formula (a power-law) and other more specific kernels (e.g. exponential kernels) that are easy to compute. In this work, we use an exponential kernel to model the overdose spikes decaying in space and time. More details are discussed in Chapter 3.

2.1.3 Model Inference

One approach to infer the parameters for point processes is to leverage its likelihood function. The log-likelihood for the point process with the intensity $\lambda(t)$ over a certain space R is as the following:

$$\log p(X|\Theta) = \sum_{i=1}^N \log(\lambda(t_i)) - \int_R \lambda(t) dt, \quad (2.6)$$

where the second term here can be seen as a normalization term for the likelihood. In the case of the multivariate temporal point process, we can estimate the set of parameters Θ by minimizing the following negative log-likelihood function:

$$-\log p(L(\Theta)) = - \sum_{i=1}^N \log(\lambda_{u_k}(t_i)) + \sum_{u=1}^U \int_R \lambda(t) dt. \quad (2.7)$$

Several approaches of MLE for the multivariate Hawkes process were proposed to estimate the parameters. One of them is to impose regularization terms to improve the accuracy and avoid over-fitting [58]. For example, [59] infer Hawkes processes by imposing some regularity on the model parameters through maximum-penalized likelihood estimation. Some MLE solutions focused on speeding up the estimation by learning the the matrix \mathbf{K} through an

online learning framework on streaming data [60]. In our work, we use an expectation-maximization (EM) based maximum likelihood estimation (MLE) to infer the parameters for our Hawkes processes model.

2.2 A Brief Review of Multi-armed Bandit Problems

The multi-armed bandit problem is an optimization problem of limited resource allocation in a way that maximizes the expected gain. The properties of each action are only partially observed during the time of allocation. As time passes or as we allocate more resources, the properties of each action can become better understood. Such a problem falls down to the category of a reinforcement learning problem that tackles the exploration-exploitation trade-off dilemma. Considering a set of K choices, we repeatedly select a single every round. After each selection, a reward is drawn from either an unknown distribution that may or may not depend on the action that you selected. Each draw from this distribution is independent of other draws, meaning that one action will not affect the rewards obtained from other actions. Our goal is to maximize the total expected reward obtained over some time period. Another approach to assessing the performance is to compare it against the best-arm benchmark. Given the optimal action a^* , then the best-arm performance over the time period T is just $q(a^*) * T$, where $q(\cdot)$ is the function that returns the reward given an action. Therefore, we can further define regret at round T , i.e., $R(T)$ as:

$$R(T) = q(a^*) * T - \sum_{i=1}^T X_i. \quad (2.8)$$

Here we review existing literature on multi-armed bandits (MAB). Several categories of algorithms exist, including ϵ -greedy, Bayes rule, and upper confidence bound algorithms. In ϵ -greedy strategy, one action is selected with probability $1 - \epsilon$, and action is selected randomly with probability ϵ . The algorithm, ϵ -greedy, is then presented in algorithm 1. Note that $Q(A)$ is the average of rewards of action A .

In the case of ϵ -greedy algorithms, many adaptations have been proposed. [61] follow a probability distribution to select levers during the exploration phase, and such probability

Algorithm 1 ϵ -greedy algorithm optimization

```
1: procedure  $\epsilon$ -GREEDY( $\mathbf{A}, k, T$ )
2:   Initialize, for  $a = 1$  to  $k$ :
3:      $Q(a) \leftarrow 0$ 
4:      $N(a) \leftarrow 0$ 
5:   for  $t = 1, 2, \dots, T$  do
6:      $A \leftarrow \begin{cases} \arg \max_a Q(a), & \text{with probability } 1 - \epsilon. \\ \text{a random action,} & \text{with probability } \epsilon. \end{cases}$ 
7:      $R \leftarrow \text{bandit}(A)$ 
8:      $N(A) \leftarrow N(A) + 1$ 
9:      $Q(A) \leftarrow Q(A) + \frac{1}{N(A)}[R - Q(A)]$ 
10:  end for
11: end procedure
```

is calculated through a softmax function, where a “temperature” parameter is introduced to adjust how often random actions are chosen during exploration. In the line of work from [62], budgets for pulling levers are further considered. Levers are uniformly pulled within the budget limit during the first ϵ rounds (i.e., the exploration phase). In the rest of $1 - \epsilon$ rounds, [62] then solve the exploitation optimization as an unbounded knapsack problem by viewing costs, values, and budgets as weights, estimated rewards, and knapsack capacity, respectively. One of the most popular approaches in the Bayes rule family of MAB problems is Thompson sampling [63]. It starts with a fictitious prior distribution of rewards, and the posterior gets updated as actions are played. Here is an example of Thompson sampling for Gaussian MAB. We consider a special case when observations/rewards are generated from $\mathcal{N}(\mu, 1)$. Our goal is to learn μ as we play more rounds. Starting with prior distribution $\mathcal{N}(0, 1)$, the posterior distribution for parameter μ is $\mathcal{N}(\hat{\mu}_n, 1/(n+1))$, where $\hat{\mu}_n$ is empirical average of the n samples ($\hat{\mu}_0$ is defined as 0). The overall Thompson sampling MAB algorithm is presented in algorithm 2. While in some cases, sampling from the complex posterior may be intractable, [64] replaces the posterior distribution with a bootstrap distribution. In the work of [65], they focus on scenarios with drifting rewards and tackle such a problem by assigning larger weights to more recent rewards when updating the posterior distribution.

Finally, upper confidence bound (UCB) algorithms [66] is one of the most popular strategies in MAB. Essentially, a UCB algorithm builds a bounded interval that captures the true

Algorithm 2 Thompson Sampling using Gaussian priors

```
1: procedure THOMPSON SAMPLING( $\mathbf{A}, k, T$ )
2:   Initialize, for  $a = 1$  to  $k$ :
3:      $Q(a) \leftarrow 0$ 
4:      $N(a) \leftarrow 0$ 
5:      $t \leftarrow K + 1$ 
6: end procedure
```

reward with high possibility, and levers with higher bounds tend to be selected. The following is an example of one of the simplest UCB algorithms (algorithm 3). Under the condition

Algorithm 3 UCB1

```
1: procedure UPPER CONFIDENCE BOUND ALGORITHM(K)
2:   Initialize, for  $a = 1$  to  $k$ :
3:      $Q(a) \leftarrow 0$ 
4:      $N(a) \leftarrow 0$ 
5:   Play each of the  $K$  arms once, and update  $Q(a)$  accordingly
6:   for  $t = 1, 2, \dots, T$  do
7:     Play arm  $a_t = \arg \max_a Q(a) + \sqrt{\frac{2 \log t}{N(a)}}$ 
8:     Observe reward  $r_t$  and update  $Q(a)$ 
9:      $N(a) \leftarrow N(a) + 1$ 
10:  end for
11: end procedure
```

that reward distribution is with support $[0, 1]$, the expectation regret after any number of plays n is bounded by the following:

$$E[R(n)] \leq 8 \sum_{i: a_i \neq a^*} \frac{\log n}{\Delta_i} + \left(1 + \frac{\pi^2}{3}\right), \quad (2.9)$$

where $\Delta_i = q(a^*) - q(a_i)$. UCB algorithms are also widely studied within the setting of contextual bandit problems where rewards or actions are characterized by features (i.e., context). Given the observations on the features of rewards, [67] and [68] model the reward function through linear regression, and the predictive reward is further bounded by predictive variance. Such an idea is shared by [69] where the authors adopt Gaussian process regression (\mathcal{GP}) to bound the predicted rewards by the posterior mean and standard deviation conditioned on the past observations. [70] take a further step by encoding geoloca-

tion relations between levers into features when rewards are collected in a domain of space. Even though \mathcal{GP} regression modeling takes spatial relations among levers into account in Wu, Schulz, Speekenbrink, *et al.*'s line of work, the lack of consideration for non-stationary rewards or temporal clustering patterns makes it inapplicable in many real-world problems such as those considered in this paper. To overcome such shortcomings, we develop an upper confidence bound strategy using Bayesian Hawkes processes (\mathcal{HP} s) in this work. \mathcal{HP} s have been widely studied and applied in many areas from earthquake modeling [71] and financial contagion [72], to event spike prediction [73] and crime prevention [74]. However, \mathcal{HP} s have not been combined with MAB strategies to date, and we show how they can be seamlessly integrated with existing UCB algorithms to build a spatial and temporal aware MAB algorithm. Furthermore, we will develop a Hawkes processes multi-armed bandits algorithm that leverages the theoretical expected number of events to infer the potential optimal arms and investigate its expected regret.

3. SOS-EW: SYSTEM FOR OVERDOSE SPIKE EARLY WARNING USING DRUG MOVER’S DISTANCE-BASED HAWKES PROCESSES

In this study, we use a robust toxicology dataset from Marion County, Indiana [Indianapolis] that were collected as part of the CDCs Prevention for States funding initiative [75]–[77]. In the toxicology dataset, we observe spatio-temporal clustering patterns [7]. These shift patterns demonstrate that overdose events concentrate within micro places in a short time window and shift through time, which motivates our present work. ¹

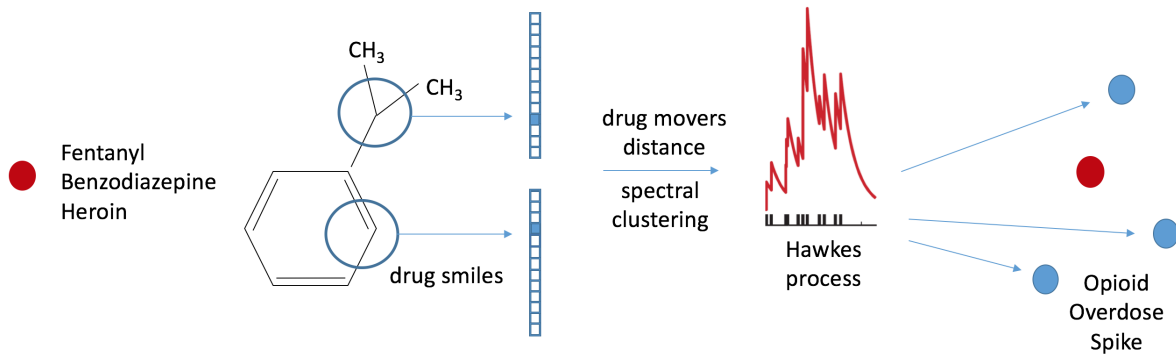


Figure 3.1. Overview of the SOS – EW system for early warning of opioid spikes. The initial overdose toxicology report shows fentanyl, benzodiazepine, and heroin present. Each drug is vectorized using SMILES and the event is assigned an overdose category using spectral clustering based on earth mover’s distance of the drug vectors (“drug mover’s distance”). The increase in the intensity of the Hawkes process is determined by the category and allows for the prediction of an opioid overdose spike, those events triggered in the branching process by the initial overdose.

An overview of our proposed system, SOS-EW, is given in Figure 3.1. We use a Hawkes process to model overdoses as a branching process. Each event may trigger offspring events nearby in space and time. The branching ratio of the process, determining the average number of offspring, depends on the drugs contained in the toxicology report of each parent event in the branching process. To reduce the dimension, we use spectral clustering with earth mover’s distance on bags of drug SMILES [78] vectors corresponding to each toxicology

¹↑This work has been accepted by the 4th Workshop on Data Science for Social Good. Chiang, Wen-Hao, et al. “Sos-EW: System for overdose spike early warning using drug mover’s distance-based Hawkes processes.” *Joint European conference on machine learning and knowledge discovery in databases*. Springer, Cham, 2019.

report (we refer to in the rest of the paper as “drug mover’s distance”). The resulting method outperforms existing Dirichlet-based Hawkes topic models in the task of early warning of opioid overdose spikes (clusters) based on an initial event and its toxicology report.

3.1 Method

SOS – EW system for early warning of opioid spikes is mainly comprised of the following two components:

1. Overdose category clustering;
2. Marked spatio-temporal Hawkes process kernel estimation and simulation.

Given a toxicology report, overdose events are first clustered into several overdose categories through spectral clustering [79]. The distance between overdose events in spectral clustering is measured based on earth mover’s distance [80] of drug vectors which characterize drug’s two-dimensional molecular structure (in particular we use SMILES, one hot encoded molecular substructures [78]). Drug overdose events over continuous time are then modeled through spatio-temporal Hawkes processes. We estimate the productivity for each category based on historical overdose events and simulate future events to generate a short ranked list of hotspots containing overdose spikes. Figure 3.1 presents an overview of the SOS – EW system.

3.1.1 Related Work

Self-exciting (Hawkes) point processes have been used to model space-time clustering in urban crime patterns [81] and Hawkes process-based learning to rank algorithms were recently a top-performing solution in the 2017 NIJ Crime Forecasting competition [46], which focused on ranking the top crime hotspots in a city according to short-term crime risk. Other point process models, for example, log-Gaussian Cox Processes, can model spatial diffusion of events and have also proven accurate at modeling crime hotspots [82], [83]. More recently, self-exciting point processes have been used to model clustering in emergency call data [84].

In more extreme security settings spatio-temporal point process models for event prediction have been applied to conflict [85] and terrorism [86] datasets.

In the above studies, the models either only used as input the spatial coordinates and time of the events, or in some cases an additional low-dimensional (< 10) event category. However, event data often is accompanied by a high dimensional mark, for example, text data, imagery, sensor data, or in our case a 133 dimensional vector indicating drugs in a toxicology screen.

Recent work in the machine learning and information retrieval literature has focused on extending temporal and network-based Hawkes processes to handle text information in the events [87], [88]. Dirichlet Hawkes processes [47], [88] have been introduced for this purpose, where document clustering is jointly learned with a temporal Hawkes process. In the network setting, Hawkes processes have been used to model coupled information and event diffusion on networks [89]. However, these studies have not dealt with spatio-temporal data, which is critical in studying the spread of opioid overdoses.

Our work offers several contributions to the above-related literature. First, we investigate the applicability of existing Hawkes-topic models in the spatial setting and then we improve upon the accuracy of these models in several prediction tasks related to early warning of opioid overdose clusters. Second, we introduce a novel clustering method for drug overdoses based upon drug mover’s distance. Related to word mover’s distance [90] that has shown higher coherence than LDA based topic models, we believe our drug mover’s distance-based spectral clustering may be useful in a variety of applications where sets of molecules need to be compared and clustered.

3.1.2 Overdose Categorization

To categorize overdose events through clustering, we first measure the similarity between two overdose events in terms of a “distance” based on the drugs involved in the events. Each event consists of a mark indicating one or more drug substances found in the victim’s system. We denote an event i containing m drug substances as $\mathbf{E}_i = \{\mathbf{d}_1, \mathbf{d}_2, \dots, \mathbf{d}_m\}$, where drug m is denoted as \mathbf{d}_m . Each drug is represented by a set of 2D substructures, i.e.,

$\mathbf{d} \in \{s_1, s_2, \dots, s_k\}$, where the substructure k is denoted as s_k . The distance between each drug event is then calculated by earth mover's distance [80].

Earth mover's distance (EMD) is a metric to measure a distance between two distributions. EMD is based on the minimal cost that must be paid to move one distribution into the other. Given two events, \mathbf{E}_p and \mathbf{E}_q , with m and n drugs, respectively, we want to find a transportation flow $\mathbf{F} \in \mathbb{Z}_2^{m \times n}$, where $\mathbb{Z}_2 = \{0, 1\}$, that minimizes the overall cost:

$$\begin{aligned} & \min \sum_{i=1}^m \sum_{j=1}^n F_{ij} C_{ij}, \\ \text{subject to } & \sum_{j=1}^n F_{ij} \leq 1 \quad 1 \leq i \leq m, \\ & \sum_{i=1}^m F_{ij} \leq 1 \quad 1 \leq j \leq n, \\ & \sum_{i=1}^m \sum_{j=1}^n F_{ij} \leq \min(m, n). \end{aligned} \tag{3.1}$$

C_{ij} is the cost for moving \mathbf{d}_i to \mathbf{d}_j . We define such cost as Jaccard distance [91] and it can be calculated by dividing the difference of the sizes of the union and the intersection of two sets of substructure by the size of the union:

$$C_{ij} = \frac{|\mathbf{d}_i \cup \mathbf{d}_j| - |\mathbf{d}_i \cap \mathbf{d}_j|}{|\mathbf{d}_i \cup \mathbf{d}_j|}. \tag{3.2}$$

Such an optimization problem 3.1 can be further solved through the transportation simplex method [92]. Once the optimal transportation flow is found, the EMD between event \mathbf{E}_p and \mathbf{E}_q is defined as the resulting overall cost normalized by the total transportation flow:

$$\text{EMD}(\mathbf{E}_p, \mathbf{E}_q) = \frac{\sum_{i=1}^m \sum_{j=1}^n F_{ij} C_{ij}}{\sum_{i=1}^m \sum_{j=1}^n F_{ij}}. \tag{3.3}$$

After calculating the EMD between each overdose events, we then construct a similarity matrix (i.e., adjacency matrix). The similarity between \mathbf{E}_p and \mathbf{E}_q is calculated using a radial basis function kernel, i.e., $\exp \left(\frac{-\text{EMD}(\mathbf{E}_p, \mathbf{E}_q)^2}{2\epsilon^2} \right)$. To categorize drug overdose events into different clusters, we apply spectral clustering [93] on all the events. The spectral clustering algorithm takes in the adjacency matrix and uses the eigenvalues and eigenvectors from the

adjacency matrix of the events to perform dimensionality reduction before clustering. Each

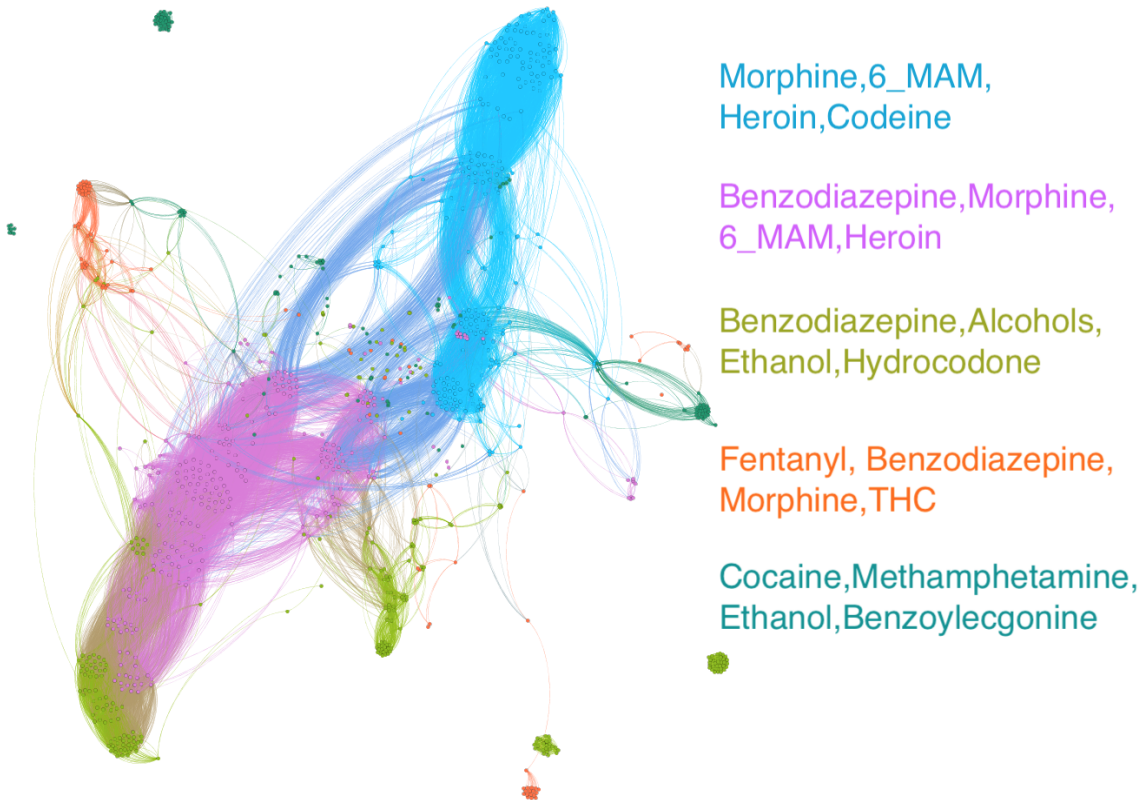


Figure 3.2. Gephi visualization of graph used for spectral clustering (edges correspond to adjacency weight greater than .9) and the most frequent drugs in each of the 5 overdose categories.

overdose event is then assigned to a category u . Therefore, each event $\mathbf{E}_i = (t_i, x_i, y_i, u_i)$ consists of four pieces of information: t_i is the timestamp of the date of death (D.o.D) of the victim; x_i and y_i are the latitude and longitude of where the victim is found; and u_i is the drug overdose category. Our approach to overdose categorization can seamlessly integrate the molecular substructure similarities across different drug overdoses and produce more pharmacokinetic-aware categories. Figure 3.2 shows the top 5 overdose categories, along with the most frequent drugs in each category, computed using our drug mover’s distance-based spectral clustering approach.

3.1.3 Spatio-temporal Hawkes Process

Clustering in space-time drug overdose event data may occur for a variety of reasons; for example, an increase in the prevalence of a new street drug may appear in a neighborhood leading to a spike in overdoses; or a particular batch of drugs may contain a higher than usual amount of a dangerous substance, for example, fentanyl. Motivated by the observed clustering of overdose data [7], we further characterize drug overdose events through a cross-exciting spatio-temporal Hawkes process [94] that models the contagiousness of events across overdose categories (computed using DMD spectral clustering).

Given a drug overdose sequence $\{\mathbf{E}_i\}_i^N$ with N events, we characterize a multivariate spatio-temporal Hawkes process through the following conditional intensity function for each category u :

$$\lambda_u(x, y, t) = \mu_u(x, y) + \sum_{t > t_i} K_{u_i u} g(x - x_i, y - y_i, t - t_i). \quad (3.4)$$

In Equation (3.4), the background rate $\mu_u(x, y)$ for each category is assumed to be a constant in time, while inhomogeneous in space. The historical events increase the likelihood of the near-future events through the spatio-temporal triggering density function g . $\mathbf{K}(u_i, u_j) = K_{u_i, u_j}$ is the productivity (or triggering) matrix to quantify the self or cross-exciting impact of the events associated with category u_i on the subsequent events in the category u_j . Specifically, K_{u_i, u_j} denotes the mean number of events in process u_j that are triggered by each event in the process u_i .

We introduce a parametric form of the triggering density with an exponential function in time and a Gaussian density in space. These choices allow for a weighted sample mean estimation of the parameters in the maximization (M) step of expectation-maximization (EM) based maximum likelihood estimation (MLE) [95].

Our kernel density-based background rate and triggering density function take the following form:

$$\begin{aligned}\mu_u(x, y) &= \sum_{i=1}^N \frac{\beta_{u_i u}}{2\pi\eta^2 T_{\text{span}}} \times \exp\left(-\frac{(x-x_i)^2 + (y-y_i)^2}{2\eta^2}\right), \\ g(x, y, t) &= \omega \exp(-\omega t) \times \frac{1}{2\pi\sigma^2} \exp\left(-\frac{x^2 + y^2}{2\sigma^2}\right),\end{aligned}\tag{3.5}$$

where T_{span} denotes the time spanned through the whole training dataset; $\beta_{u_i u}$ measures the extent to which events in process u_i contribute to the background rate in the process u_j ; ω controls how fast the rate $\lambda_u(x, y, t)$ returns to its baseline level $\mu_u(x, y)$ after an event occurs; and η and σ dictate the spreading scale of the triggering effect in space.

We perform the M step of the EM-type algorithm following the framework of Algorithm 1 in [94] to estimate the parameters. We use the “optimal” parameters from the previous M step to update the latent variables and alternately iterate E and M step. After parameter estimation, we utilize the branching structures [96] of self-exciting point processes to simulate self and cross-exciting events (See Algorithm 3 in [94]) for the next T days for 1,000 times. The simulated events are denoted as $\hat{\mathbf{E}} = (\hat{t}, \hat{x}, \hat{y}, \hat{u})$.

To make recommendations for early warning of overdose spikes, we generate a short ranked list of hotspots in the domain of interest. We first partition the domain of interest into $N \times N$ fine-grained grid cells by dividing the latitude and longitude span into N parts with equal length. Based on the latitude and longitude (i.e., \hat{x} and \hat{y}) from the simulated events, we calculate the average number of the simulated events for each grid cell from 1,000 repeated simulations. We denote the average number of the simulated events in the i^{th} and j^{th} grid in terms of latitude and longitude as $\chi(i, j)$. Finally, we sort the grids according to the average number of the simulated events in descending order and retain the top- N grids as the recommended short ranked list.

3.2 Comparison Methods

We compare our model with several state-of-the-art methods including the following: Non-parametric temporal Hawkes Processes; Spatio-temporal univariate Hawkes Processes;

and Dirichlet Hawkes Processes that learn the category assignment while estimating the intensity function. None of the existing point process methods jointly learn the spatio-temporal self and cross-exciting density together for different overdose categories based on the drug substance structure; methods either exist for spatio-temporal point processes or for time-only topic point processes, but not both. The details of our implementation for these baseline methods are presented in the following sections.

3.2.1 Non-parametric Hawkes Processes:SimpHP

Our first baseline model utilizes a non-parametric Hawkes process [59] that takes a series of time stamps and then uses a penalized MLE to simultaneously estimate the background rate $\mu(t)$ and triggering kernel $g(t)$ without prior knowledge of their form. Given a set of overdose events, we partition the training dataset into $N \times N$ subsets according to which fine-grained grid cell they belong (as defined in Section 3.1.3). Each subset of events corresponds to an independent Hawkes process. Once the estimation is done, the simulation for the next T interval is done through thinning [97]. Each Hawkes process is first simulated 1,000 times and the average number of simulated events is calculated. The top- N grids cell with the largest average number of simulated events is recommended. We denote this baseline method as **SimpHP** [59].

3.2.2 Spatial-temporal Hawkes Processes:SpatHP

We compare **SOS – EW** with a sub-model that only uses the geolocation and time stamps for estimation, without clustering events into different categories (univariate). The model estimation and recommendation follow the same framework in Section 3.1.3. Such a baseline model is denoted as **SpatHP** [94].

3.2.3 Dirichlet Hawkes Processes:SpatHP

The Dirichlet Hawkes process [88] is a random process which takes into account both text information from documents and temporal dynamics of their arrival pattern to cluster the document streams. The model is estimated through an online inference algorithm that

jointly learns the pattern of the clusters and the parameters of the Hawkes process for each cluster. To adapt to this model, we view each overdose event as a document and each drug as a word. Spatial information is integrated into each event by adding a grid cell index as an additional word. After model estimation, we then use thinning [97] based simulation and average the number of events for each grid cell and topic (over 1,000 simulations) to generate a recommendation of the top- N grid cells with the most number of simulated events.

3.3 Experiments

3.3.1 Data

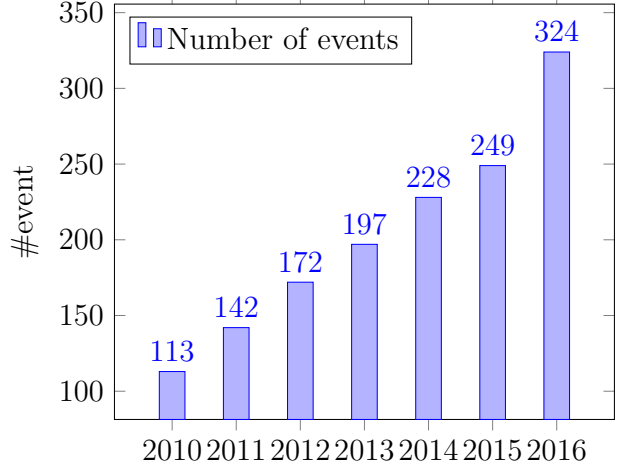
We analyze a toxicology dataset from Marion County, Indiana that was collected as part of the CDCs Prevention for States funding initiative [75]–[77]. The dataset contains toxicology reports of 1,489 overdose death events in Indianapolis, Indiana, U.S.A. from 2010 to 2016. Each overdose event includes the date of death (D.o.D) of the victim and the geolocation (latitude and longitude) of where the victim was found. In addition, every event also contains forensic toxicology testing results that screen for 164 drug substances. A binary indicator represents whether a specific drug substance was found in the victim’s body. In our analysis, we restricted to a subset of 133 drugs whose 2D chemical structure representation can be found in the chemical molecules database, Pubchem [98], for further feature generation. We also restricted our analysis to the 1,425 overdose events that include geolocation information and occurred within the city of Indianapolis boundary, where the latitude ranges from 39°37’58.8”N to 39°55’30.3”N and the longitude ranges from 87°06’41.1”W to 85°56’18.7”W. Table 3.1 presents the statics of the pruned dataset. Figure 3.4 presents the example of some overdose events.

Features for each drug are extracted by identifying its molecular substructure fingerprints. Specifically, each drug is represented by a set of substructures s (i.g., $\mathbf{d} \in \{s_1, s_2, \dots, s_k\}$). We further used RDKit [99], open-source software that allows us to search the substructures based on 2D chemical structures representation, to generate a feature vector of dimension 1,024 for each drug. The pruned dataset is then used for model evaluation.

Table 3.1. Statistics on Overdoes Event

start date	01-14-2010
end date	12-30-2016
#event	1,425
$\overline{\#d}$	6.3698
$\overline{\#ent_d}$	68.2481

In this table, “#event” represents the number of events in the toxicology report; “ $\overline{\#d}$ ” represents the average number of drug substances in each event; and “ $\overline{\#ent_d}$ ” is the average number of events involved in each drug.

**Figure 3.3.** Number of Events per Year

3.3.2 Evaluation Protocols and Metrics

The domain of Indianapolis covered by the pruned dataset is first partitioned into $N \times N$ grid cells by dividing the latitude and longitude span into N parts with equal length in each direction. For each time interval t^{th} , we recommend a ranked list of grid cells based on how likely those grid cells are to have overdose events in the near future, using the history of the process up to t^{th} time interval. The performance is then evaluated through walk forward optimization [95]. Specifically, in our experimental setting, we first train our model over a fixed amount of the most recent historical events, which is 255 events (the number of events in the first two years). We then test the model on the next time period starting on 01/01/2012 and report the performance. Finally, the overall performance is the average from all the time periods that we have tested.

At each time interval T , models recommend a ranked list of size K for potential overdose events. In our experimental setting, we set T as 5 days and partition the domain of interest into 100×100 grid cells. The time window is consistent with the time scale on which police and health services can respond and the grid cell size is similar to those used in field trials of predictive policing [10]. The ranking performance is evaluated through normalized discounted cumulative gain at K ($NDCG@K$), which is a measurement of ranking quality and

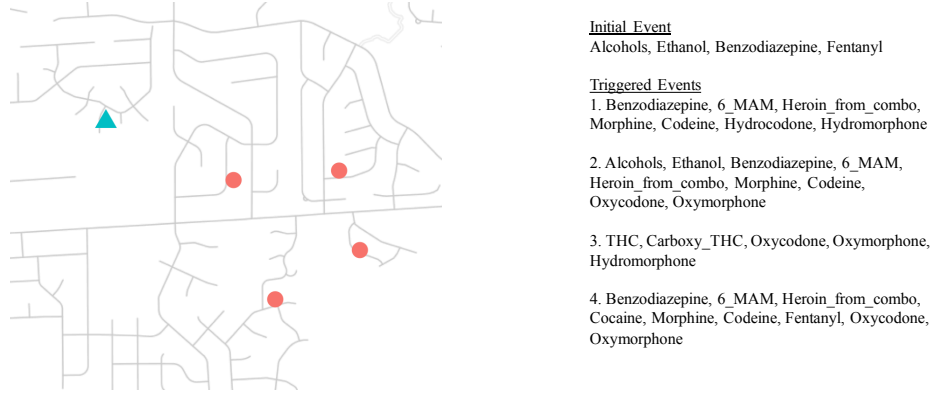


Figure 3.4. An illustration for an initial event and its triggered events in one of the categories (i.e., one of the Hawks processes). The initial overdose event marked in triangle symbol consists of four drug substances and it triggered four neighboring events consisting of different number of drug substances respectively.

commonly used in information retrieval. $NDCG@K$ is calculated by normalizing discounted cumulative gain (denoted as $DCG@K$) with ideal $DCG@K$ (denoted as $IDCG@K$). The definition are as follows:

$$DCG@K = \sum_{i=1}^K \frac{2^{rel_i} - 1}{\log_2(i + 1)}, \quad NDCG@K = \frac{DCG@K}{IDCG@K}, \quad (3.6)$$

where rel_i is the i^{th} relevance value of the i^{th} grid in the ranked list \mathbf{r} ; $IDCG@K$ is the ideal $DCG@K$ when the ranked list \mathbf{r} is perfectly ranked based on its relevance values; and then we define relevance value rel_i as the number of overdose events that happen in the i^{th} grid cell in the ranked list \mathbf{r} and t^{th} time interval.

In a certain time interval, a spike of overdose events may occur. To evaluate our model's ability to forecast future spikes, we first define an event spike at the t^{th} time interval in a grid cell (i, j) as follows: If the total number of events in the neighboring cells between the $(t - 1)^{th}$ and $(t + 1)^{th}$ intervals is more than a threshold, then we consider that there is an

event spike in (i, j) grid within these time intervals. The set of grids with an event spike is defined as the following:

$$\mathbf{s} = \left\{ (i, j, t) \mid \sum_{\hat{i}=i-w}^{i+w} \sum_{\hat{j}=j-w}^{j+w} \sum_{\hat{t}=t-1}^{t+1} \chi(\hat{i}, \hat{j}, \hat{t}) \geq \xi \right\} \quad (3.7)$$

where $\chi(i, j, t)$ is the count of events in grid cell (i, j) and time interval t , w is the spatial window size defining how many neighboring cells we should consider; and ξ is the spike threshold: we set $\xi = 2$ (for $w = 2$ and 4) and $\xi = 10$ (for $w = 10$ and 15) in our evaluation setting. With larger w and ξ , more grid cells will be considered to have an event spike. We choose w and ξ to ensure a reasonable amount of event spikes for further evaluation while an event spike includes a huge amount of overdose events. We adopt modified reciprocal hit rank [100], precision and recall at different ranked list size K , denoted as $MRHR$, $Prec$, and Rec to evaluate the performance. $MRHR$ is a modified version of average reciprocal hit rank (ARHR), which is feasible for ranking evaluations where there are multiples relevant items (i.e., multiple spikes events), and it is calculated as the following:

$$MRHR = \frac{1}{|\mathbf{s}|} \sum_{i=1}^K \left(\frac{hit_i}{rank_i} \right), \quad (3.8)$$

$$\text{where } hit_i = \begin{cases} 1 & \text{if } r_i \in \mathbf{s} \\ 0 & \text{if } r_i \notin \mathbf{s} \end{cases}, rank_i = \begin{cases} rank_{i-1} & \text{if } hit_{i-1} = 1 \\ rank_{i-1} + 1 & \text{if } hit_{i-1} = 0, \end{cases}$$

where each hit is rewarded based on its position in the ranked list. $Prec$ and Rec are commonly used to evaluate the performance in recommendation system. $Prec$ evaluates how precisely the model can predict for future spike events while Rec measures the ability of retrieving spikes. We also evaluate average precision, denoted as APC , to account for both precision and recall without choosing K :

$$Prec = \frac{|\mathbf{s} \cap \mathbf{r}|}{|\mathbf{r}|}, \quad Rec = \frac{|\mathbf{s} \cap \mathbf{r}|}{|\mathbf{s}|}, \quad APC = \frac{\sum_{\{k:1,\dots,K | r_k \in \mathbf{s}\}} Prec@k}{|\mathbf{s} \cap \mathbf{r}|}. \quad (3.9)$$

3.3.3 Experimental Results

Table 3.2. Overall Performance on Different Spike Window Size w

w	mdl	<i>MRHR</i>			<i>Prec</i>			<i>Rec</i>			<i>APC</i>
		@1%	@3%	@5%	@1%	@3%	@5%	@1%	@3%	@5%	
2	SOS – EW	.0172	.0188	.0191	.0277	.0174	.0124	.2534	.5038	.6110	.0451
	SimpHP	.0088	.0089	.0090	.0034	.0019	.0018	.0289	.0496	.0842	.0103
	SpatHP	.0017	.0021	.0023	.0036	.0029	.0025	.0375	.1129	.1590	.0043
	TopicHP	.0080	.0082	.0082	.0130	.0085	.0055	.1258	.2386	.2748	.0125
4	SOS – EW	.0218	.0236	.0240	.1091	.0724	.0555	.2690	.5196	.6699	.1187
	SimpHP	.0059	.0060	.0060	.0126	.0070	.0060	.0279	.0475	.0660	.0118
	SpatHP	.0016	.0018	.0020	.0114	.0111	.0112	.0274	.0784	.1294	.0102
	TopicHP	.0082	.0089	.0090	.0474	.0315	.0205	.1089	.2226	.2434	.0250
10	SOS – EW	.0219	.0254	.0259	.2000	.1526	.1229	.1911	.6734	.8554	.1851
	SimpHP	.0029	.0031	.0032	.0189	.0119	.0111	.0128	.0662	.0854	.0125
	SpatHP	.0003	.0007	.0007	.0167	.0181	.0193	.0109	.0691	.1025	.0151
	TopicHP	.0096	.0097	.0098	.0856	.0548	.0360	.1974	.2868	.3121	.0335
15	SOS – EW	.0620	.0718	.0726	.4387	.3275	.2549	.3234	.6470	.8025	.3644
	SimpHP	.0070	.0072	.0072	.0445	.0291	.0254	.0336	.0526	.0676	.0301
	SpatHP	.0016	.0019	.0020	.0516	.0506	.0503	.0220	.0746	.1119	.0387
	TopicHP	.0083	.0091	.0092	.1739	.1212	.0802	.1035	.2081	.2267	.0622

The column “mdl” corresponds to different models. The best overall performance is **bold**.

Table 5.1 presents the overall performances on overdose spikes prediction under different breadth definition of spike events (Equation 3.7). Our SOS – EW system consistently outperforms other baseline methods by a large margin in terms of *MRHR*, *Prec*, *Rec*, and *APC*. *MRHR* is used to evaluate the ranking quality while *Prec*, *Rec*, and *APC* evaluate the retrieval for events spikes. This shows our proposed method not only can successfully recommend the regions with potential event spikes considering the ranking position but it can also precisely generate a short ranked list for those event spikes precisely. As the ranking list size increases, performances of *MRHR* remains similar after *MRHR* @3%; *Prec* decreases while *Rec* increases due to the natural trade-off between these two metrics. SOS – EW estimates the model parameters and makes predictions specifically for different overdose categories compared to SpatHP which estimates the same parameters for all event data aggregated together. This indicates that strategically clustering overdose events based on the

drug molecular structure can achieve better performances than the model which solely relies on spatio-temporal information. **TopicHP** jointly learns the clustering structure and model parameters and it can be viewed as a competitive baseline. However, only the drug distribution in each event is taken into account and drugs’ chemical structure is not included in the model training. This may explain why **TopicHP** falls short of spikes recommendation metrics compared to **SOS – EW** but is still better than other baselines. Overall, **SOS – EW** leverages the information from geo-locations, event triggering dynamics, and drugs’ high level physical and chemical properties based on 2D structures altogether and precisely makes the recommendations for future overdose event spikes.

Table 3.3. Overall *NDCG* Performance

mdl	@1%	@3%	@5%
SOS – EW	.0322	.0637	.0842
SimpHP	.0191	.0236	.0265
SpatHP	.0092	.0179	.0262
TopicHP	.0492	.0733	.0750

The column “mdl” corresponds to different models. The best overall performance is **bold**.

Table 3.3 presents the overall model performances on *NDCG* when only evaluating each models ability to rank grid cells (equivalent to $\omega = 0$). The ranking quality increases as the size of the ranked list grows larger (i.e., from 1% to 5%). Our proposed **SOS – EW** outperforms the second best baseline method **TopicHP** by 12.27% at *NDCG* @5%, however, **TopicHP** is the top performing model at 1% and 3%. These results indicate that for the very highest risk cells, spatial diffusion may play less of a role and **TopicHP** and **SOS – EW** have similar performance. However, for flagging neighborhoods instead of individual cells for spikes, **SOS – EW** is superior due to its ability to model spatial diffusion of risk.

3.4 Implications for Practice

Results from our proposed system can be translated into more effective social service delivery and intervention programming. When flagging the top 1% of predicted spikes defined in neighborhoods of approximately $O(1km^2)$ in size and 5 days in length, the method captures

around 25% of opioid spikes. These spatial and temporal scales are similar in size to those used in predictive policing [10] and by efficiently predicting the geographic diffusion of opioid-related toxins (such as fentanyl), social service programs and first responders can develop dynamic programs to best target areas where people face the highest risk of overdose. Further research is needed to verify whether or not the results found in Indianapolis in this study extend to other cities and rural areas.

Studies have revealed polydrug patterns whereby fentanyl is being detected alongside cocaine and methamphetamines, which is contributing to overdose deaths involving these substances [18], [19]. Given the nature of this supply-side poisoning among illicit drugs, the most feasible approach may be to empower and provide persons who used drugs with the ability to test these substances. Drug testing technologies (i.e., fentanyl test strips) allow drug users to understand whether the drugs they use are contaminated with lethal substances, such as fentanyl, which can allow them to adjust behaviors and prevent a potentially fatal overdose [101]. Furthermore, the average of dispatch and response time for emergency medical services (EMS) personnel to arrive when an overdose event is reported is seven minutes on average ² and the time to results of many drug test strips is usually less than minutes nowadays. Therefore, our system can make a prediction in a short time so that the health/social workers can react accordingly. More research is needed to extend the method in this paper, that utilizes toxicology reports, to the application of drug test strips and other drug testing tools (which may not be as thorough as a coroner's report).

Public health services can deploy syringe services, such as retractable syringes or exchange programs, that have been shown to reduce fatal opioid use [102], [103]. From a policing perspective, officers can be equipped with nasal naloxone (or Narcan) within high-risk opioid locations to reduce the likelihood of death from an opioid overdose [104], [105].

²<https://www.medicalnewsbulletin.com/response-time-emergency-medical-services/>

4. HAWKES PROCESS MULTI-ARMED BANDITS

4.1 Methodology

In this section, we introduce Hawkes Processes based UCB algorithm, denoted as HpUCB. First, we define the problem setting and the reward distribution. We then derive the expected number of events given the Hawkes processes parameters within a specific time period. After we present the algorithm, we will attempt to analyze its regret bound following the regime of UCB1-Normal.

4.1.1 Problem Formulation

Given a spatial domain, we first divide it into a set of subregions, where self-exciting events take place. We then divide a time span T into several time intervals by δt . Each round d , each multi-armed bandit (MAB) algorithm recommends a short ranked list of subregions to visit and the events that happen in the visited regions are discovered. We then consider the number of discovered events as rewards. The events in each subregion are generated through its own independent Hawkes process. Each Hawkes process follows a simple exponential decay kernel in the following form:

$$\lambda_k(t) = \nu_k + \sum_{\substack{t > t_i \\ t_i \in \mathcal{T}_k}} \alpha_k e^{-\beta_k(t-t_i)}, \quad (4.1)$$

where λ_k is the event intensity and \mathcal{T}_k is the set of timestamps for events in arm k ; and ν_k , α_k and β_k represent the background rate, reproduce number and decay rate, respectively, for arm k . We denote them as $\theta_k = (\nu_k, \alpha_k, \beta_k)$. The rewards of action k is then defined as the number of events in round d , that is $|\mathcal{T}_k^d|$. Each round lasts for δt .

Our goal is to maximize total rewards, i.e., the total number of observed events in the visited sub-regions after a total of D visits.

4.1.2 Theoretical Expected Number of Events

During each visit of the multi-armed bandit process, we observe a set of self-exciting events. With these events, we can estimate a set of Hawkes process parameters based on the observed events. For example, in the round d , we visit the subregion k and observe events \mathcal{T}_k^d . We then estimate the parameters based on \mathcal{T}_k^d , denoted as $\theta_k^d = (\nu_k^d, \alpha_k^d, \beta_k^d)$. Given the estimated parameters, we can infer the expected number of events for the future and build upper confidence bound based on the inference. The key ingredient of such a strategy is the derivation of the theoretical expected number of events for Hawkes processes.

In the work of [106], an elementary approach is introduced to obtain moments of Hawkes processes and/or the intensity of a number of marked Hawkes processes, in which the detailed outline is given step-by-step.

Following the framework in [106], one can obtain the expected number of events for a simple Hawkes processes accumulated up to any time t given the parameter θ as the following:

$$E[N(t)|\theta] = \begin{cases} \frac{-\beta\nu}{\alpha-\beta}t + \frac{\alpha\nu}{(\alpha-\beta)^2} \left[\exp\{(\alpha-\beta)t\} - 1 \right] & \alpha \neq \beta \\ \nu t + \frac{1}{2}\nu\alpha t^2 & \alpha = \beta \end{cases}. \quad (4.2)$$

For simplicity, we use θ to represent the parameters estimated at round d from region k (i.e., θ_k^d) in general.

In the multi-armed problem setting, we are more interested in the expected number of events during the time period/rounds when we visit the sub-region instead of an accumulation up to any given time. Given the equation 4.2, the expected number of events during round d , denoted as $E[\Psi(d)|\theta]$ can be calculated as in equation 4.3.

$$\begin{aligned} E[\Psi(d)|\theta] &= E[N(\delta t \times D) - N(\delta t \times (D-1))|\theta_k] \\ &= E[N(\delta t \times D)] - E[N(\delta t \times (D-1))|\theta] \\ &= \begin{cases} \frac{-\beta\nu}{\alpha-\beta}\delta t + \frac{\alpha\nu}{(\alpha-\beta)^2} \exp\{(\alpha-\beta)\delta t \times d\} \left[\exp\{(\alpha-\beta)\delta t\} - 1 \right] & \alpha \neq \beta \\ \nu\delta + \frac{1}{2}\nu\alpha(\delta t)^2(2d+1) & \alpha = \beta \end{cases}. \end{aligned} \quad (4.3)$$

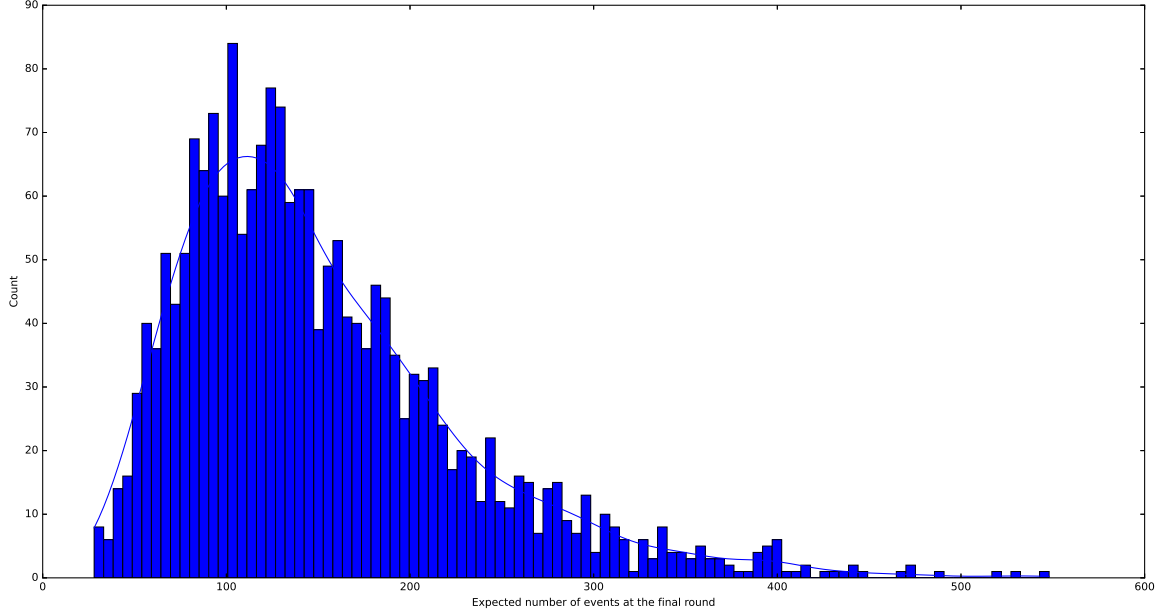


Figure 4.1. Expected number of events at the 2000th round ($d = 2000$) from a simulated Hawkes processes dataset. We use the sets of estimated parameters from $j = 1$ to $j = 1999$ to calculate the expect number of events at round 2000 and plot out the histogram. The distribution pass the D’Agostino and Pearson’s normality test with a p-value of 1.07×10^{-97} .

4.1.3 Construction of Upper Confidence Bound on Future Expectation

After a couple of rounds of visits, we have visited region k possibly non-consecutively with n_k times. Combining with equation 4.3, for any given round d in the future, we calculate the expected number of events for each θ_k^j in Θ_k , respectively. We then denote them as $\Psi_k^j(d)$, where $j = 1, \dots, n_k$. With a number of observations and multiple estimations, we can construct upper confidence bound based on the estimation. Before we introduce the overall algorithm, we assume that the estimation error of Ψ_k follows a normal distribution. Therefore, as Ψ_k is significantly large, Ψ_k also follows a normal distribution. Fig. 4.1 shows the example of the approximately normal distribution of Ψ_k from a realization of the simulated Hawkes processes dataset.

Most of the UCB algorithms require the reward distribution to be bounded for the guaranteed regret bound [107]. One particular algorithm, UCB-normal [108], only requires the reward distribution to be a normal distribution. Under the assumption of Ψ_k approximately

following normal distribution, we then can build the upper confidence bound for Ψ_k at round d using UCB-normal:

$$\overline{\Psi}_k(d) + \sqrt{16\eta \frac{\sum_{j=1}^{n_k} [\Psi_k^j(d)]^2 - n_k [\overline{\Psi}_k(d)]^2 + \epsilon \ln(d-1)}{n_k - 1} \frac{1}{n_k}}, \quad (4.4)$$

where $\overline{\Psi}_k(d) = \frac{1}{n_k} \sum_{j=1}^{n_k} \Psi_k^j(d) = \frac{1}{n_k} \sum_{j=1}^{n_k} E[\Psi_k(d)|\theta_k^j]$. Hyper-parameter η is used to adjust the trade-off between the exploration and exploitation. A small number of ϵ can prevent the case when the first couple rounds have no events and the model stops exploring.

Algorithm 4 Hawkes Processes Multi-armed bandit Algorithm

```

1: procedure HpUCB( $K, \eta, \epsilon$ )
2:   for  $d = 1, 2, \dots, D$  do
3:     If there exists an arm that is played less then  $\lceil 8\ln(d) \rceil$ , play the arm.
4:     Otherwise play  $\hat{k} = \arg \max_k \overline{\Psi}_k(d) + \sqrt{\eta * 16 \frac{\sum_{j=1}^{n_k} [\Psi_k^j(d)]^2 - n_k [\overline{\Psi}_k(d)]^2 + \epsilon \ln(d-1)}{n_k - 1} \frac{1}{n_k}}$ ,
5:     Update  $n_k$ 
6:   end for
7: end procedure

```

Overall algorithm is presented in algorithm 4 and we denoted it as HpUCB.

4.1.4 Regret Analysis of HpUCB

In this section, we demonstrate the regret analysis of HpUCB. To make the regret analysis tractable, we consider the case where η and ϵ are set to 0. The performance of different hyper-parameter settings is investigated empirically instead.

Following the work of [108], we can adapt the regret analysis of UCB-Normal into HpUCB. The regret bound in [108] for UCB-Normal is based on two conjectures which are only verified numerically.

Conjecture 1. *Given a Student random variable X with s degrees of freedom, for all $0 \leq a \leq \sqrt{2(s+1)}$,*

$$P(X \geq a) \leq e^{-\frac{a^2}{4}}, \quad (4.5)$$

Conjecture 2. *Given a random variable X following a Chi-squared distribution with s degrees of freedom,*

$$P(X \geq 4s) \leq e^{-\frac{(s+1)}{2}}, \quad (4.6)$$

We first define $Q_k(d) = \sum_{j=1}^{n_k} [\Psi_k^j(d)]^2$ and $U_k(d) = \sqrt{16 \frac{Q_k(d) - n_k [\overline{\Psi}_k(d)]^2}{n_k - 1} \frac{\ln(d-1)}{n_k}}$.

The expected regret can be calculated as the following:

$$E[R(D)] = \sum_{k=1}^K \left\{ \sum_{d=1}^D P(A_d = k) \Delta_k^d \right\}, \quad (4.7)$$

where A_d is the random variable represents the action at round d ; Δ_k^d is the difference between the optimal action and action k , that is, $\Delta_k^d = q^d(k^*) - q^d(k)$. Note that $q^d(k)$ is a function that returns the reward at region k at round d . To bound the regret, we take the maximal of Δ_k^d across all the rounds that we play up to D and denote it as $\tilde{\Delta}_k = \max_d \Delta_k^d$, where $0 \leq d \leq D$.

$$E[R(D)] \leq \sum_{k=1}^K E[T_k(D)] \tilde{\Delta}_k, \quad (4.8)$$

where $T_k(D)$ is the number of times arm a_k is played in the first D trials. With this, our goal is then to bound $E[T_k(D)]$. We start with initialization process where we play all the arms one time:

$$T_k(D) \leq 1 + \sum_{d=K+1}^D \mathbf{1}(A_d = k). \quad (4.9)$$

After the initialization, we select arms according to the upper confidence bounds. The bound can be further loosen by assuming that arm a_k has been played l times:

$$T_k(D) \leq l + \sum_{d=K+1}^D \mathbf{1}\{A_d = k, T_k(D-1) \geq l\}. \quad (4.10)$$

In specific, the event $A_d = k$ means that on the previous time step, the upper confidence bound of action k was greater than that of the optimal one k^* based on our estimates:

$$\begin{aligned} T_k(D) \leq l + \sum_{d=K+1}^D \mathbf{1} \left\{ \overline{\Psi}_{k^*}(d-1) + U_{k^*}(d-1) \leq \overline{\Psi}_k(d-1) + U_k(d-1), \right. \\ \left. T_k(D-1) \geq l \right\}. \end{aligned} \quad (4.11)$$

where n_{k^*} in $U_{k^*}(d-1)$ is $T_{k^*}(d-1)$ and n_k in $U_k(d-1)$ is $T_k(d-1)$.

Moreover, the minimum of the upper bounds on the optimal arm in all the time steps must be less than the maximum of the upper bounds on the arm k (after l trials).

$$T_k(D) \leq l + \sum_{d=K+1}^D \mathbf{1} \left\{ \min_{0 \leq s < d} \overline{\Psi}_{k^*}(s) + U_{k^*}(s) \leq \max_{l \leq b \leq d} \overline{\Psi}_k(b) + U_k(b) \right\}, \quad (4.12)$$

where n_{k^*} in $U_{k^*}(s)$ is $T_{k^*}(s)$ and n_k in $U_k(b)$ is $T_k(b)$.

Since the particular indices for which they occur are unknown, we consider all possible pairs of indices to loosen this bound further.

$$\begin{aligned} T_k(D) &\leq l + \sum_{d=K}^D \sum_{s=1}^{D-1} \sum_{b=l}^{D-1} \mathbf{1} \left\{ \overline{\Psi}_{k^*}(s) + U_{k^*}(s) \leq \overline{\Psi}_k(b) + U_k(b) \right\} \\ E[T_k(D)] &\leq l + \sum_{d=1}^{\infty} \sum_{s=1}^{D-1} \sum_{b=l}^{D-1} P \left(\left\{ \overline{\Psi}_{k^*}(s) + U_{k^*}(s) \leq \overline{\Psi}_k(b) + U_k(b) \right\} \right). \end{aligned} \quad (4.13)$$

To make sure the event $\overline{\Psi}_{k^*}(s) + U_{k^*}(s) \leq \overline{\Psi}_k(b) + U_k(b)$ happens, one of the following three must also occur:

1. $\overline{\Psi}_{k^*}(s) + U_{k^*}(s) \leq q^s(k^*)$;
2. $\overline{\Psi}_k(b) \geq q^b(k) + U_k(b)$;
3. $q^s(k^*) < q^b(k) + 2U_k(b)$.

We can loosen the bound through a union of three events.

$$\begin{aligned} E[T_k(D)] &\leq l + \sum_{d=1}^{\infty} \sum_{s=1}^{D-1} \sum_{b=l}^{D-1} P \left(\left\{ \overline{\Psi}_k(b) \geq q^b(k) + U_k(b) \right\} + \right. \\ &\quad \left. \left\{ \overline{\Psi}_{k^*}(s) + U_{k^*}(s) \leq q^s(k^*) \right\} + \left\{ q^s(k^*) < q^b(k) + 2U_k(b) \right\} \right). \end{aligned} \quad (4.14)$$

In [108], they show that the random variable $\frac{\overline{\Psi}_k(b) - q^b(k)}{\sqrt{\frac{Q_k(b) - n_k [\overline{\Phi}_k(b)]^2}{n_k(n_k - 1)}}}$ has a Student distribution with $n_k - 1$ degrees of freedom. Note that n_k here is $T_k(b)$. We then use Conjecture 1 by letting $s = n_k - 1$ and $a = 4\sqrt{\ln(d)}$, and we bound the probability:

$$P(\{\overline{\Psi}_k(b) \geq q^b(k) + U_k(b)\}) = P(\{\frac{\overline{\Psi}_k(b) - q^b(k)}{\sqrt{\frac{Q_k(b) - n_k [\overline{\Phi}_k(b)]^2}{n_k(n_k - 1)}}} \geq 4\sqrt{\ln(d)}\}) \leq d^{-4}, \quad (4.15)$$

for $n_k \geq 8\ln(d)$. We can bound $\{\overline{\Psi}_{k^*}(s) + U_{k^*}(s) \leq q^s(k^*)\}$ through a similar fashion. The last one is $\{q^s(k^*) < q^b(k) + 2U_k(b)\}$. In [108], they also show that the random variable $\frac{Q_k(b) - n_k [\overline{\Phi}_k(b)]^2}{[\sigma_k^b]^2}$ follows a chi-square distribution with $n_k - 1$ degree of freedom. Through Conjecture 2 with $s = n_k - 1$ and $a = 4s$, we have

$$\begin{aligned} P(\{q^s(k^*) < q^b(k) + 2U_k(b)\}) &= P(\{\frac{Q_k(b) - n_k [\overline{\Phi}_k(b)]^2}{[\sigma_k^b]^2} > (n_k - 1) \frac{[q^s(k^*) - q^b(k)]^2}{[\sigma_k^b]^2} \frac{n_k}{64\ln(d)}\}) \\ &\leq P(\{\frac{Q_k(b) - n_k [\overline{\Phi}_k(b)]^2}{[\sigma_k^b]^2} > 4(n_k - 1)\}) \\ &\leq e^{-\frac{n_k}{2}} \leq d^{-4}, \end{aligned} \quad (4.16)$$

as long as $n_k \geq \max\left\{256 \frac{[\sigma_k^b]^2}{[q^s(k^*) - q^b(k)]^2}, 8\right\} \ln(d)$. This means that as long as we play arm k for more than $\lceil \max\left\{256 \frac{[\sigma_k^b]^2}{[q^s(k^*) - q^b(k)]^2}, 8\right\} \ln(d) \rceil$, we can guarantee that $E[T_k(D)]$ in Equation 4.14 can be bounded:

$$\begin{aligned} E[T_k(D)] &\leq l + \sum_{d=1}^{\infty} \sum_{s=1}^d \sum_{b=l}^d 3d^{-4} = l + \sum_{d=1}^{\infty} 3d^{-2} \\ &\leq 1 + 256 \frac{[\sigma_k^b]^2}{[q^s(k^*) - q^b(k)]^2} \ln(d) + 8\ln(d) + \frac{\pi^2}{2} \\ &\leq 256 \ln(d) \frac{\hat{\sigma}_k^2}{\hat{\Delta}_k^2} + \left(1 + \frac{\pi^2}{2} + 8\ln(d)\right), \end{aligned} \quad (4.17)$$

where $\hat{\sigma}_k = \max_b [\sigma_k^b]^2$, $1 < b < D$ and $\hat{\Delta}_k = \min_{s,b} [q^s(k^*) - q^b(k)]$, $1 < s, b < D$.

The regret bound of HpUCB takes the form:

$$E[R(D)] \leq \sum_{k=1}^K E[T_k(D)] \tilde{\Delta}_k \leq \sum_{k=1}^K \left[256 \ln(d) \frac{\hat{\sigma}_k^2}{\hat{\Delta}_k^2} \tilde{\Delta}_k + \left(1 + \frac{\pi^2}{2} + 8 \ln(d) \right) \tilde{\Delta}_k \right]. \quad (4.18)$$

In UCB-Normal, the mean and standard deviation of the reward distribution remain the same across the time periods. In the setting of Hawkes Processes MAB problem, the properties are dynamic, and therefore, each round has its own expectation and standard deviation values. We show that under the assumption that the estimation of the expected number of events at round d follows a normal distribution, the regret can still be bounded by $O(K \ln(d))$. However, it also depends on the variance of the estimation $\hat{\sigma}_k$ and the difference between the $\hat{\Delta}_k$. The larger the variance, the larger the regret bound is. The smaller $\hat{\Delta}_k$ is, which means it is harder to differentiate the optimal arm from the other, the larger the regret bound is as well.

4.2 Experiments

4.2.1 Baseline Methods

We compare our model HpUCB with several multi-armed bandit baselines and these baseline models are tailored to tackle the multi-armed bandit problems with a non-stochastic reward distribution. Starting with algorithms that update the reward observation with exponential weights, **exp3** and its variation **exp3S** [109]. The name **exp3** stands for “Exponential-weight algorithm for Exploration and Exploitation.” Essentially, this type of algorithm keeps the estimations by a list of weights. The arms are then randomly selected based on their weight. After the rewards are received, it updates the weights with respect to this returned value of the payoff. Beside of the simplest UCB algorithm **UCB1** [108], other non-stochastic variation are established. In the work of [110], discounted UCB **dUCB** and sliding-window UCB **slideUCB** are presented. In **dUCB** algorithm, the contribution of each observation to the mean estimation and upper bound construction decays exponentially. On top of **dUCB**, **slideUCB** relies on a local empirical average of the observed rewards. More recent work in [111], monitored-UCB **mUCB** is proposed. It introduces a change-point detection component

into a classic Upper Confidence Bound (UCB) algorithm. Once the property change-point of reward distribution is detected, \mathbf{mUCB} will reset and learn the new optimal arm.

4.2.2 Datasets

Temporal Synthetic Data (\mathcal{D}_{SIM}):

We first test our methodology on a synthetic dataset. We generate the dataset by a thinning algorithm and apply our model directly to the dataset. In total, we simulate 20 nodes of independent Hawkes Processes.

Records of Worldwide Earthquakes ($\mathcal{D}_{\text{EARW}}$):

We collect the spatial and temporal records of earthquakes from the United States Geological Survey [112], and we curate the dataset starting from the year 1990. Earthquakes are known to occur in some earthquake-prone regions. We first separate these events into subregions and then we can test our model by considering each subregion as an arm. One way to categorize each earthquake record into different subregions is clustering based on its geolocation. We apply k-nearest neighbors algorithms to the earthquake dataset and categorize them into 20 subregions. We denote the dataset as $\mathcal{D}_{\text{EARW}}$.

Records of Earthquakes in Alaska and California ($\mathcal{D}_{\text{EACA}}$):

To validate our model on a more fine-grained dataset, we further curate the dataset from $\mathcal{D}_{\text{EARW}}$ and retain the records in Alaska and California in the USA. Alaska and California states are in between Pacific Plate and North American Plate, which makes these two states the most earthquake-prone areas in the USA. We map each earthquake record to the closest county or county equivalent area. Since most of the earthquakes happen in the coastal area, we further retain the top-18 subregions with the most earthquakes. The pruned dataset is then denoted as $\mathcal{D}_{\text{EACA}}$.

Records of Crime Activities in Vancouver (\mathcal{D}_{VAN}):

Besides the earthquakes, crime activities are also known for their self-exciting properties. We collect the crime records from Vancouver Open Data Catalogue ¹. In this dataset, the events are separated into 24 subregions/beats by the local police office. We then remove the top-2 subregions with the most frequent crime activities, which have more criminal activities compared to other subregions by a large margin. We remove these 2 subregions since it can be easily learned by multi-armed bandits algorithms. Therefore, the algorithms may result in similar performances. The dataset is then denoted as \mathcal{D}_{VAN} .

Records of Crime Activities in Los Angeles (\mathcal{D}_{LA}):

One other crime-related dataset is crime activities in Los Angeles ². This dataset reflects incidents of crime in the City of Los Angeles dating back to 2010. The events are categorized into 21 divisions. We also removed the top-2 subregions with the most frequent crime activities. We then denote this dataset as \mathcal{D}_{LA} .

4.2.3 Reward Performances

In the simulation dataset, we separate the time horizon into 2000 rounds and 350 of them are used to tune the hyper-parameters for all the models. In the real-world dataset, we separate the time horizon into 500 rounds, and 150 of them are used in searching the hyper-parameters.

In table 4.1, 4.2, 4.3, 4.4, and 4.5, we present the performances of all models in various of datasets. We evaluate the performance through accumulated rewards. Each round, we visit 1, 3, and 5 regions and record the rewards. We then denote the metrics as $\overline{\text{reward}} @1$, $\overline{\text{reward}} @3$, and $\overline{\text{reward}} @5$, respectively. Overall, the proposed method HpUCB consistently outperforms all the other baseline methods in all $\overline{\text{reward}} @1$, $\overline{\text{reward}} @3$, and $\overline{\text{reward}} @5$. The only exceptions are $\overline{\text{reward}} @1$ in the datasets $\mathcal{D}_{\text{EACA}}$, \mathcal{D}_{LA} and \mathcal{D}_{VAN} . However, our model HpUCB maintains competitive performances compared to the best model UCB1 in these

¹<http://data.vancouver.ca/datacatalogue/crime-data.htm>

²<https://www.kaggle.com/cityofLA/crime-in-los-angeles>

cases. It could be because in these datasets, the best region has more events of interest than the others, and it remains at a constant rate throughout time. Therefore, the simple stationary model UCB1 can easily find the best choice, and our model HpUCB can also learn from the background rate component. As we intend to visit more sub-optimal regions which have more dynamic patterns, the edge of HpUCB starts to show. That is, the improvements in performance against the baseline methods start to increase as we visit more regions. This trend can be observed across all the datasets. In general, the experiments show that HpUCB performs well on both the simulated and the real-world datasets. Given the nature of self-exciting properties in criminal activities and earthquakes, the proposed model HpUCB can leverage temporal information between the events and make good choices for the future.

Table 4.1. Simulation Dataset \mathcal{D}_{Tem}

Model	$\overline{\text{reward}} @1$	$\overline{\text{reward}} @3$	$\overline{\text{reward}} @5$
exp3	22082.04	66204.84	110369.52
exp3S	22077.62	66216.92	110815.02
mUCB	26265.64	69635.68	113784.50
dUCB	22080.98	66682.14	116890.50
UCB1	26127.42	70433.06	114255.68
slideUCB	23723.02	74205.02	119480.26
HpUCB	26852.66	79581.46	129435.24

Table 4.2. Best Performance on Earthquake in Worldwide $\mathcal{D}_{\text{EARW}}$

Model	$\overline{\text{reward}} @1$	$\overline{\text{reward}} @3$	$\overline{\text{reward}} @5$
exp3	35036.98	107201.78	182437.32
exp3S	38214.14	105540.68	176299.54
mUCB	76027.06	154577.96	218291.04
dUCB	35199.30	184907.30	285493.22
UCB1	74553.12	135262.34	222301.98
slideUCB	60541.08	224853.94	279058.86
HpUCB	82733.12	226576.80	332122.48

In Figure 4.2 and Figure 4.3, we show the cumulative rewards for all models from $\mathcal{D}_{\text{EARW}}$ and $\mathcal{D}_{\text{EACA}}$. In Figure 4.2, our model HpUCB learns the optimal arm in the first 200 rounds and consistently choose the optimal ones. In Figure 4.3 where the number of arm is 1, HpUCB has a similar performance as UCB1 until the very end of the time horizon. Selection strategies,

Table 4.3. Earthquake in AK and CA $\mathcal{D}_{\text{EACA}}$

Model	$\overline{\text{reward}} @1$	$\overline{\text{reward}} @3$	$\overline{\text{reward}} @5$
exp3	27348.74	84980.46	142215.24
exp3S	28185.16	87948.66	137464.80
mUCB	44527.22	109739.32	161888.84
dUCB	27373.84	114044.32	186503.26
UCB1	47902.72	107992.10	166784.96
slideUCB	34088.48	125104.70	190080.82
HpUCB	47304.70	140628.14	221007.26

Table 4.4. Crime Activities in Vancouver \mathcal{D}_{VAN}

Model	$\overline{\text{reward}} @1$	$\overline{\text{reward}} @3$	$\overline{\text{reward}} @5$
exp3	8467.18	25517.68	42729.38
exp3S	8434.34	25269.72	42111.20
mUCB	16619.18	40339.22	57674.34
dUCB	11468.04	39930.84	61504.18
UCB1	17552.16	44436.14	61726.74
slideUCB	16945.46	44027.14	61444.04
HpUCB	17311.86	50971.72	80531.40

Table 4.5. Crime Activities in Los Angeles \mathcal{D}_{LA}

Model	$\overline{\text{reward}} @1$	$\overline{\text{reward}} @3$	$\overline{\text{reward}} @5$
exp3	41110.18	123348.12	205715.82
exp3S	41102.44	123235.70	205530.36
mUCB	46108.64	131706.22	214805.94
dUCB	43018.02	131227.52	215557.94
UCB1	46579.32	133710.34	215999.10
slideUCB	46399.08	133618.60	215751.74
HpUCB	46277.78	139447.44	226297.88

such as exp3 and exp3S don't perform well in general. One possible explanation is that the probability to sample the arms grows exponentially based on the rewards. As the rewards grow larger, the probability for multiple competitive arms to be sampled may be saturated. Thus, the algorithms may fail to distinguish those arms.

Overall, mUCB and UCB1 are competitive algorithms when the number of the pulled arm is small. On the other hand, HpUCB has the better performance when multiple competing arms with different event spikes are present.

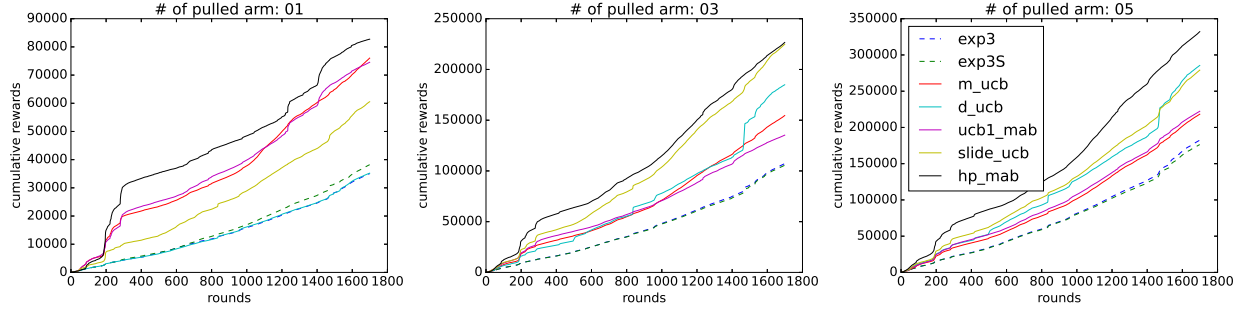


Figure 4.2. Cumulative rewards of records of worldwide earthquakes $\mathcal{D}_{\text{EARW}}$

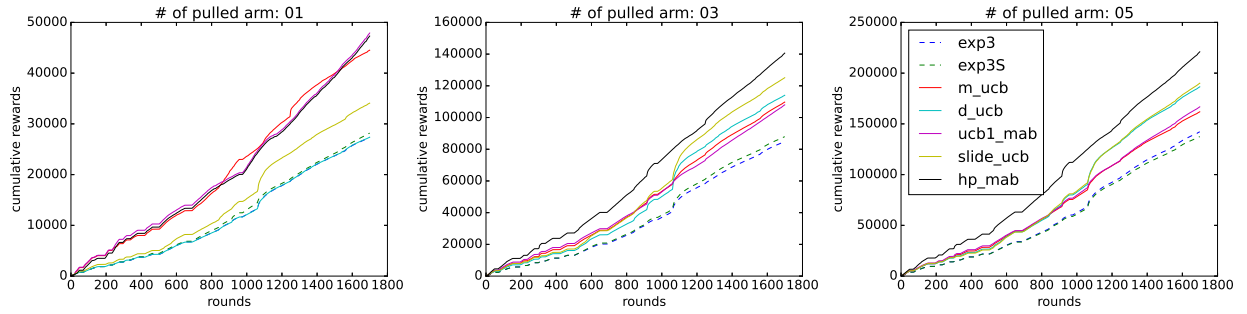


Figure 4.3. Cumulative earthquake rewards of records in AK CA $\mathcal{D}_{\text{EACA}}$

5. HAWKES PROCESS MULTI-ARMED BANDITS FOR SEARCH AND RESCUE

Following the previous work, in this chapter, we introduce a novel spatio-temporal Hawkes process multi-armed bandit algorithm. In this project, we incorporate the spatial information into the context and fill up the gaps of observations through simulations. The detailed methodology is presented in the following section.

5.1 Methodology

Here we provide the details of our MAB Hawkes process methodology. We view each sub-region of space as a MAB “lever” and the count of disaster events observed in a pulled lever as the reward. In each round we select several sub-regions to search and our goal is to maximize the cumulative number of events observed over time in pulled levers.

5.1.1 Spatio-temporal MAB Problem Formulation

We first partition the entire spatial domain into a set of grid cells, and we denote this set of cells as $\mathcal{A} = \{a_1, a_2, \dots\}$. We divide the range of longitude and latitude evenly into X and Y grids, i.e., $X \times Y$ cells in total. Each grid cell is characterized by a feature vector \mathbf{x}_a . In this manuscript, we use the grid indicators as features to describe the geolocation of a cell, i.e., $\mathbf{x}_a = [x, y]^T$. Given a time span T , each multi-armed bandit (MAB) algorithm recommends a short ranked list consisting of N cells to visit, denoted as \mathbf{a} , for every W time units. For each visit v at cell $a \in \mathbf{a}$, we observe the events that occurred in the cell, denoted as \mathcal{T}_v^a , and we consider the number of discovered events $|\mathcal{T}_v^a|$ as rewards r_v^a . Our goal is to maximize total rewards, i.e., the total number of observed events in the visited cells after a total of V visits. This type of sequential decision-making task is a spatio-temporal multi-armed bandit problem in which each cell is viewed as a lever, and each visit to the set of chosen grid cells (constrained by resources) can be viewed as pulling the levers of the MAB machine.

5.1.2 Hawkes Process Multi-armed Bandits

We model the occurrence of events in space and time using a Hawkes process where the intensity is given by,

$$\lambda(t|\theta, \mathcal{T}) = \mu + \sum_{t_i < t, t_i \in \mathcal{T}} \alpha \beta \exp^{-\beta(t-t_i)}. \quad (5.1)$$

Here, θ represents the parameters (μ, α, β) where μ is the background intensity; α is the infectivity factor (when viewed as a branching process this is the expected number of direct offspring an event triggers); and β is the exponential decay rate capturing the time scale between generations of events. Here \mathcal{T} is the set of timestamps for inference.

At each round of the multi-armed bandit (MAB) process, we select N cells with the highest estimated risk to visit, and we observe the events. However, time has elapsed between consecutive visits to a cell and there is a gap that needs to be filled. Therefore, to fill up these gaps, we simulate Hawkes processes (\mathcal{HP} s) by thinning [113] based on the inferred parameters. A combination of actual observations and simulated events is then defined as a set of timestamps that represents our best guess on the missing gap for each grid cell. We denote these sets of timestamps as $\hat{\mathcal{S}} = \{\hat{\mathcal{S}}^a | a \in \mathcal{A}\}$. After each visit, we update each $\hat{\mathcal{S}}^a$ by choosing the most likely \mathcal{HP} realization and defining that as the event history.

To estimate the Hawkes process parameters, we use Bayesian inference¹ to estimate $\hat{\mathcal{S}}^a$ for each visited cell $a \in \mathcal{A}$ and to estimate the parameters of \mathcal{HP} s [114]. The likelihood function is given by Equation 5.2, where $\hat{\mathcal{S}}^a = \{t_1, t_2, \dots, t_n\}$.

$$\mathcal{L}(\hat{\mathcal{S}}^a | \mu, \alpha, \beta) = \prod_{i=1}^{|\hat{\mathcal{S}}^a|} \lambda(t_i) \exp^{-\int_0^{t_n} \lambda(u) du}. \quad (5.2)$$

If we denote the prior by $p(\mu, \alpha, \beta)$, we get the posterior $p(\mu, \alpha, \beta | \hat{\mathcal{S}}^a) \propto p(\mu, \alpha, \beta) \mathcal{L}(\hat{\mathcal{S}}^a | \mu, \alpha, \beta)$, where $0 < \mu, \beta < \infty$ and $0 < \alpha < 1$. Here, we choose a gamma distribution (\mathcal{G}) as a prior for μ and β , and we choose a beta distribution

¹<https://github.com/canerturkmen/hawkeslib>

(\mathcal{B}) as a prior for α . That is, $p(\mu), p(\beta) \sim \mathcal{G}(k_p, k_c)$, where k_p and k_c are the shape and scale parameter for \mathcal{G} , respectively ; and $p(\alpha) \sim \mathcal{B}(m, n)$, where m and n are both shape parameters for \mathcal{B} .

We use Metropolis-Hastings [115] to draw samples from the posterior distribution. We then denote such a set of parameters as $\Theta = \{\theta_1, \theta_2, \dots, \theta_L\}$, where $\theta_l = (\mu_l, \alpha_l, \beta_l)$. For each θ_l , we simulate a \mathcal{HP} realization and denote them as $\tilde{\mathcal{S}}^a = \{\tilde{\mathcal{S}}_l^a | l = 1, 2, \dots, L\}$. Together with all $\tilde{\mathcal{S}}^a$ where $a \in \mathcal{A}$, we denote them as $\tilde{\mathcal{S}}$. Note that the base intensity is a function of time, i.e., $\mu(t)$, contributed by the best guess $\hat{\mathcal{S}}_a$. Given the newly observed timestamps \mathcal{T}_v^a , together denoted as $\mathcal{T}_v = \{\mathcal{T}_v^a | a \in \mathcal{A}\}$, we then fill up the gap between the best guess $\hat{\mathcal{S}}^a$ and the observed timestamps by selecting the set of simulated timestamps, denoted as $\tilde{\mathcal{S}}_l^a$, where \mathcal{T}_v^a has the largest likelihood as in Equation 5.3. Finally, we update our best guess for observed cells by Equation 5.4.

$$\hat{l} = \underset{l}{\operatorname{argmax}} \mathcal{L}(\mathcal{T}_v^a | \theta_l, \{\tilde{\mathcal{S}}_l^a, \hat{\mathcal{S}}^a\}). \quad (5.3)$$

$$\hat{\mathcal{S}}^a = \{\mathcal{T}_v^a, \tilde{\mathcal{S}}_l^a, \hat{\mathcal{S}}^a\}. \quad (5.4)$$

5.1.3 Spatial Upper Confidence Bound on Event Intensities

While the epsilon-greedy algorithm considers the cells with the largest mean value of rewards during exploitation, and the upper confidence bound (UCB) algorithm selects the most optimistic cells, neither considers the spatial relationship between the cells and the corresponding events. To introduce such geolocation information into MABs, Wu, Schulz, Speekenbrink, *et al.* propose a space-aware UCB algorithm utilizing a Gaussian Process regression model (\mathcal{GP}) [116] and building up a spatial UCB from the predicted expectation and uncertainty for each lever. After each visit, we collect the features of visited cells and their corresponding rewards, denoted as \mathcal{X} and \mathcal{Y} , respectively. Together with previous collections, i.e., $\mathcal{X} = \mathcal{X} \cup \{\mathbf{x}_a | a \in \mathcal{A}\}$ and $\mathcal{Y} = \mathcal{Y} \cup \{r_a | a \in \mathcal{A}\}$, we train the \mathcal{GP} regression model.

In the \mathcal{GP} , we hold a prior assumption that the correlations between two cells a and a' slowly decay following an exponential function of their distance. Thus, we select a radial basis kernel, \mathbf{k}_{RBF} , as the covariance of a prior distribution over the target functions. The kernel function \mathbf{k}_{RBF} is calculated as follows: $\mathbf{k}_{\text{RBF}}(\mathbf{x}_a, \mathbf{x}_{a'}) = \exp\left(\frac{-\|\mathbf{x}_a, \mathbf{x}_{a'}\|^2}{2\sigma_{\text{gp}}^2}\right)$, where σ_{gp} is a parameter that determines how far the correlation extends.

After each visit, we build the spatial UCB based on the prediction for each cell a by looking at its ζ_{gp} predicted uncertainty above the expected mean, and we denote such a UCB as s_{gp}^a (Equation 5.5).

Here, $\boldsymbol{\mu}$ and $\boldsymbol{\sigma}$ are the predicted expectations and uncertainties given cell a and ζ_{gp} governs how far we expend our upper confidence bound. Unlike ϵGdy and UCB1 in which only cells with the largest score are selected, the recommended cells are sampled for the next visit without replacement based on a probability distribution. Such probability distribution is calculated by a softmax function on s_{gp}^a as in Equation 5.6, where τ_{gp} can be viewed as a temperature parameter that adjusts the exploitation and exploration ratio. We further denote such a baseline method SpUCB .

$$s_{\text{gp}}^a = \boldsymbol{\mu}(\mathbf{x}_a) + \zeta_{\text{gp}}\boldsymbol{\sigma}(\mathbf{x}_a) \quad (5.5)$$

$$p_{\text{gp}}^a = \frac{\exp(s_{\text{gp}}^a/\tau_{\text{gp}})}{\sum_{a \in \mathcal{A}} \exp(s_{\text{gp}}^a/\tau_{\text{gp}})} \quad (5.6)$$

5.1.4 Combining Hawkes Process Bandits with Existing Methods

Even though the upper confidence bound (UCB) built upon the Hawkes process (\mathcal{HP}) can track the event intensities, here we show how to improve its accuracy during the early stages of the multi-armed bandit (MAB) process. We combine the score from the UCB on intensities, \bar{s}_{hp}^a in $\bar{\mathbf{s}}_{hp}$, with the score from the previously introduced method, that is, s_{ucb}^a from UCB1 or s_{gp}^a from SpUCB , respectively. We denote the combined score as \hat{s}^a . Finally, we use a softmax function to calculate the probability \hat{p}^a , and sample N cells without replacement based on the probability for our next visit. We then denote our model as $\text{SOS} - \text{EW}$.

Algorithm 5 Algorithm of SOS – EW

```

1: procedure HPSPUCB(  $\mathcal{A}, \gamma, \zeta_{\text{hp}}, \zeta_{\text{gp}}, \sigma_{\text{gp}}, \tau$  )
2:    $X \leftarrow \emptyset, \mathbf{y} \leftarrow \emptyset, \hat{\mathbf{S}} \leftarrow \emptyset, \tilde{\mathbf{S}} \leftarrow \emptyset, t_c \leftarrow W, \mathbf{a} \leftarrow$  select  $N$  cells at random
3:   for  $v = 1$  to  $V$  do ▷ MAB process
4:      $\mathcal{T} \leftarrow \{\mathcal{T}_v^a | a \in \mathcal{A}\},$ 
5:      $\mathcal{X} \leftarrow \mathcal{X} \cup \{\mathbf{x}_a | a \in \mathcal{A}\}, \mathcal{Y} \leftarrow \mathcal{Y} \cup \{r_a | a \in \mathcal{A}\}$ 
6:      $\boldsymbol{\mu}, \boldsymbol{\sigma} \leftarrow \mathcal{GP}(\mathcal{X}, \mathcal{Y} | \sigma_{\text{gp}})$  ▷ model and infer for  $\mathcal{GP}$ 
7:      $\mathbf{s}_{\text{gp}} \leftarrow \{s_{\text{gp}}^a = \boldsymbol{\mu}(\mathbf{x}_a) + \zeta_{\text{gp}} \boldsymbol{\sigma}(\mathbf{x}_a) | a \in \mathcal{A}\}$ 
8:      $\bar{\mathbf{s}}_{\text{hp}}, \hat{\mathbf{S}}, \tilde{\mathbf{S}} \leftarrow \text{HPUCB}(\hat{\mathbf{S}}, \tilde{\mathbf{S}}, \mathbf{a}, \sigma_{\text{gp}}, \zeta_{\text{hp}} t_c, \mathcal{A}, \mathcal{T})$ 
9:      $\hat{\mathbf{s}} \leftarrow \{\hat{s}^a = s_{\text{gp}}^a + \gamma \bar{s}_{\text{hp}}^a | a \in \mathcal{A}\}$ 
10:     $\hat{\mathbf{p}} \leftarrow$  apply softmax function on  $\hat{\mathbf{s}}$ 
11:     $\mathbf{a} \leftarrow$  sample  $N$  cells based on probability  $\hat{\mathbf{p}}$ 
12:     $t_c \leftarrow (v + 1) \times W$  ▷ update the current time  $t_c$ 
13:  end for
14: end procedure

```

More specifically, \hat{s}^a and \hat{p}^a are calculated as in Equation 5.7 and 5.8 where γ governs how much we rely on intensities estimated through \mathcal{HP} s, and we can adjust our model based on how much the dataset itself contains a self-excitation pattern. Note that we define \hat{s}^a and \hat{p}^a from all cells as $\hat{\mathbf{s}}$ and $\hat{\mathbf{p}}$, respectively.

$$\hat{s}^a = s^a + \gamma \bar{s}_{\text{hp}}^a. \quad (5.7)$$

$$\hat{p}^a = \frac{\exp(\hat{s}^a / \tau)}{\sum_{a \in \mathcal{A}} \exp(\hat{s}^a / \tau)}. \quad (5.8)$$

Based on the different choices of s^a to combine with the \mathcal{HP} component, we have two variations as our proposed models for comparison:

1. $\text{UCB1}_{\text{hpSp}}$ where $s^a = s_{\text{ucb}}^a$, that is, we combine \bar{s}_{hp}^a with scores from UCB1;
2. $\text{SOS} - \text{EW}$ where $s^a = s_{\text{gp}}^a$, that is, we combine \bar{s}_{hp}^a with scores from SpUCB.

Note that with $\text{SOS} - \text{EW}$ and $\text{UCB1}_{\text{hpSp}}$, we can compare when we choose different models to incorporate the proposed \mathcal{HP} component. The overall MAB process of $\text{SOS} - \text{EW}$ is presented in the algorithm 5, and algorithm 6 shows how our \mathcal{HP} component plays its part in $\text{SOS} - \text{EW}$.

Algorithm 6 Calculation of \bar{s}_{hp}^a

```
1: function HPUCB( $\hat{\mathcal{S}}, \tilde{\mathcal{S}}, \mathbf{a}, \sigma_{\text{gp}}, \zeta_{\text{hp}} t_c, \mathcal{A}, \mathcal{T}$ )
2:   for all  $a \in \mathbf{a}, \hat{S}^a \in \hat{\mathcal{S}}, \tilde{S}^a \in \tilde{\mathcal{S}}$  do
3:      $\hat{l} \leftarrow \text{argmax}_l \mathcal{L}(\mathcal{T}_v^a | \theta_l, \{\hat{S}^a, \tilde{S}_l^a\})$ , where  $\tilde{S}_l^a \in \tilde{\mathcal{S}}^a$ 
4:      $\hat{S}^a \leftarrow \{\hat{S}^a, \hat{S}_l^a, \mathcal{T}_v^a\}$ 
5:      $\Theta \leftarrow p(\mu, \alpha, \beta | \hat{S}^a)$ 
6:      $\tilde{S}^a \leftarrow \{\tilde{S}_l^a = \mathcal{HP}(\hat{S}^a | \theta_l) | \theta_l \in \Theta\}$ 
7:     update  $\hat{S}^a$  in  $\hat{\mathcal{S}}$  and  $\tilde{S}^a$  in  $\tilde{\mathcal{S}}$ 
8:   end for
9:    $\mathbf{s}_{\text{hp}} \leftarrow \{s_{\text{hp}}^a = \bar{\lambda}^a(t_c) + \zeta_{\text{hp}} \times \sigma_{\lambda^a(t_c)} | a \in \mathcal{A}\}$ , where
      $\lambda^a(t_c) = \{\lambda_l^a(t_c | \theta_l, \mathcal{T}_l^a) | l = 1, 2, \dots, L\}$  and  $\mathcal{T}_l^a = \{\tilde{S}_l^a \cup \hat{S}^a | \tilde{S}_l^a \in \tilde{\mathcal{S}}^a, \hat{S}^a \in \hat{\mathcal{S}}\}$ 
10:   $\bar{s}_{\text{hp}} \leftarrow \mathcal{GF}(\mathbf{s}_{\text{hp}} | \sigma_{\text{hp}})$ 
11:  return  $\bar{s}_{\text{hp}}, \hat{\mathcal{S}}, \tilde{\mathcal{S}}$ 
12: end function
```

5.2 Experiments

5.2.1 Datasets

Spatial-temporal Synthetic Data (\mathcal{D}_{Syn}):

We first validate our methodology using a simulated Hawkes process (\mathcal{HP}) [117]. We generate a synthetic dataset by first simulating a Poisson process for initial immigrant events, of which the average number follows a Poisson distribution $\mathcal{P}(\eta T)$, and distribute them uniformly in space. Note that η is the rate per second and T is the total time span. Next, we generate a Poisson process recursively for each event in each generation by the following steps:

1. Draw a sample following a Poisson distribution $\mathcal{P}(\phi)$ as the number of offspring, where ϕ governs the average number of offspring that an event spawns;
2. Sample the waiting time between parent and offspring following an exponential distribution $\mathcal{E}(\omega)$;
3. Sample the spatial distance between parent and offspring event according to a normal distribution $\mathcal{N}(\sigma)$; and

4. Accept and record the event only when it is within the domain of time and space. We then go back step 1. and move on to the next recent event.

The simulation stops when all of a generation are outside T . We then denote these synthetic datasets as \mathcal{D}_{syn} . In Figure 5.1, we present a realization of the synthetic data in \mathcal{D}_{syn} and

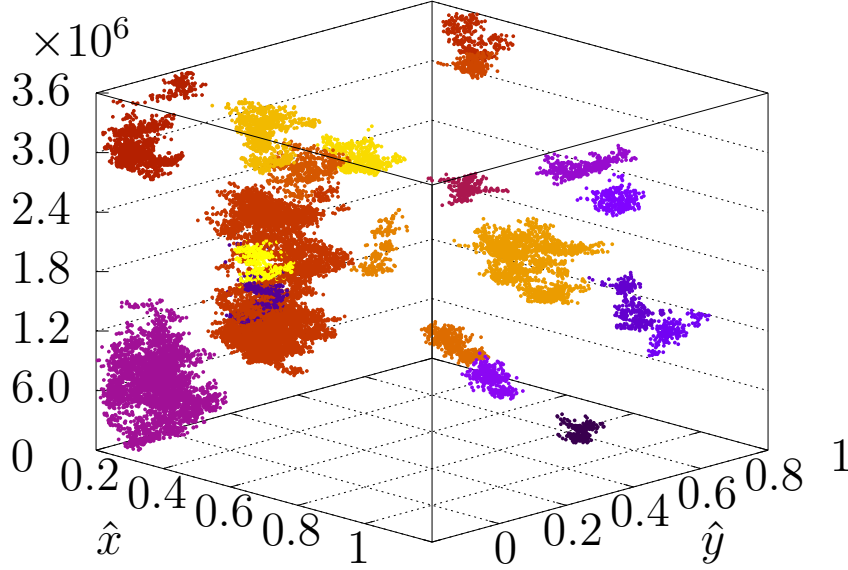


Figure 5.1. Top-20 clusters in \mathcal{D}_{syn} . Different clusters are color-coded and the parameters under this simulation are $T = 3.6 \times 10^6$ seconds, $\eta = 8 \times 10^{-5}$, $\phi = 0.99$, $\omega = 10^{-4}$ and $\sigma = 10^{-2}$.

show the top-20 largest clusters generated by the immigrants.

City of Houston 311 Service Requests (\mathcal{D}_{Hry}):

We apply the methodology to geolocated Houston 311 calls for service with time and geo-location labels during the time period of hurricane Harvey in 2017 in Houston (08/23/2017 to 10/02/2017).² Among all kinds of services, we focus on “flooding” events that contain complete timestamp, longitude and latitude information. In total, there are 4,315 311 flooding events within Houston, Texas, and we denote this dataset as \mathcal{D}_{Hry} . In Figure 5.2, we present the flooding events and color-code the timestamps. The color bar range starts

²<http://hfdapp.houstontx.gov/311/311-Public-Data-Extract-Harvey-clean.txt>

at 00:00:00 on 08/23/2017, and we can also observe the pattern of disaster-related events, where the events are reported mostly in urban regions and mostly clustered in space and time.

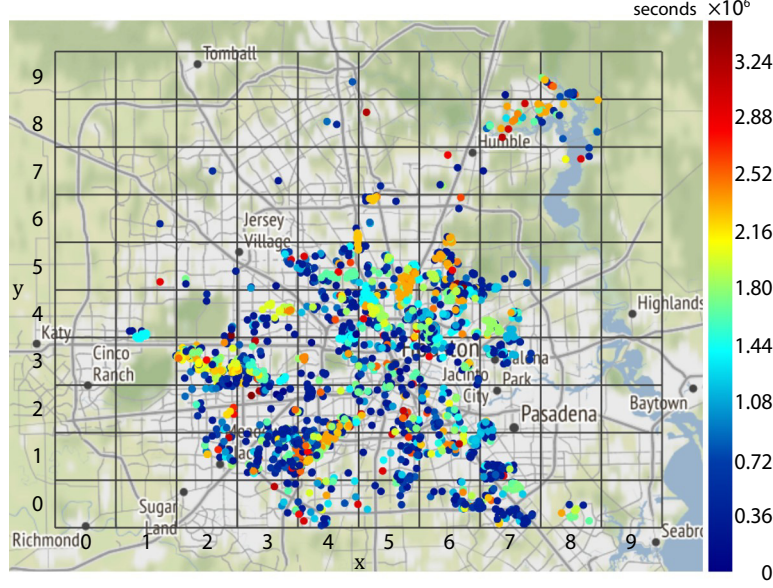


Figure 5.2. Flooding Events in Houston \mathcal{D}_{Hry} . Each event is scaled and color-coded by its timestamps, and x-axis and y-axis represents the grid cell ID.

Reports of IED attack in Iraq (\mathcal{D}_{IED}):

In addition to rescue mission during natural disaster, we also test our framework on a spatio-temporal bomb detection and removal task that also requires exploration in the under-sampled areas. In specific, we compare our model with baselines on the reports of improvised explosive device attack (IED) in Iraq. In total, we focus on the 28,593 incidents mainly in Iraq region between 02/04 and 02/24 in 2009, and denote them as \mathcal{D}_{IED} .

5.2.2 Experimental Protocol

Given a spatial domain, we first partition the range of longitude and latitude of \mathcal{D}_{Syn} and \mathcal{D}_{Hry} evenly into 10 disjoint intervals (i.e., $X = 10$ and $Y = 10$). Thus, there are 100

grid cells and every event of interest can be mapped to a unique grid cell. (We let $X = 20$ and $Y = 20$ as for \mathcal{D}_{IED} due to its larger domain.) Next, we validate the five competing models on both the synthetic datasets (\mathcal{D}_{syn}) and the real-world dataset (\mathcal{D}_{Hry} and \mathcal{D}_{IED}) by using the “walk-forward” validation approach. For example, for the 311 service request dataset \mathcal{D}_{Hry} , we discretize time starting from 08/23/2017 00:00:00 into intervals of 20 hours ($W = 72,000$ seconds). In each window of time we select $N = 10$ cells to visit.³ We then calculate the reward of the events that happen during our visits in the selected cells until the next visit. We also add these events to the historical training data set for updating the model in the next round, whereas events occurring in cells not visited are unseen by the model in the next round. We then slide the window and train the models on the historical observations up to the end of the previous observation window to make recommendations for the next visit. We then record the events that happen between 08/23/2017 20:00:00 and 08/24/2017 16:00:00. We repeat this process until the final date of 10/02/2020 24:00:00. For each grid cell, we sample 50 sets of parameters from the posterior distribution, i.e., $L = 50$. Since the selected cells at the beginning may result in different decisions and performances in the whole MAB process, for every parameter in all the models, we run MAB processes for 30 times with different initial visited cells, and we report the average of each evaluation score. Also, all parameters of the models are studied through an extensive grid search, and the best performances are reported for the model comparison. For the sake of reproducibility, all datasets and the source code are made publicly available in an anonymized repository⁴.

5.2.3 Evaluation Metrics

We first measure the performance of competing models by the cumulative reward, that is, the number of the observed events captured in visited cells. To compare the performances between different datasets in \mathcal{D}_{syn} , we then normalize the total reward by the most optimal reward, i.e., the maximum rewards if the choice of levers are optimal, and we denote it as $\overline{\text{reward}}$. At each visit, models generate a short ranked list for the next visit. Based on the

³↑We select 5 cells ($N = 5$) to visit for a duration of 5 hours ($W = 18,000$) for synthetic datasets \mathcal{D}_{syn} and we select 10 cells ($N = 10$) to visit for a duration of 40 days for \mathcal{D}_{IED} due to its longer time frame.

⁴↑<https://anonymous.4open.science/r/475a5b4d-9521-4c47-8bcb-94a5b2c1cae0/>

ranked lists, we can also evaluate the models through different ranking and recommendation metrics. One popular metric to evaluate the ranking quality is the normalized discounted cumulative gain (NDCG) [118]. We then calculate the NDCG at N for each visit, where N is the number of visited cells. The relevance value (i.e., gain) at cell a and visit v is then defined as the number of events, i.e., $|\mathcal{T}_v^a|$. Finally, we take the average across all the visits and denote it as NDCG.

From the recommendation point of view, we are interested in how many cells recommended by the models would actually contain events during our visit. We first consider that a cell is relevant if there are one or more events during the visit. We then evaluate such recommendation quality through the modified reciprocal hit rank [100], denoted as mRHR for evaluation. Modified reciprocal hit rank is a modified version of average reciprocal hit rank (ARHR), which is feasible for ranked recommendation evaluations where there are multiples relevant items (i.e., relevant cells). It can be calculated as follows:

$$\text{mRHR} = \frac{1}{|\mathbf{g}|} \sum_{i=1}^N \frac{\mathbf{h}_i}{\mathbf{r}_i}, \text{ where } \mathbf{h}_i = \begin{cases} 1 & \text{if } a_i \in \mathbf{g} \\ 0 & \text{if } a_i \notin \mathbf{g} \end{cases}, \quad \mathbf{r}_i = \begin{cases} \mathbf{r}_{i-1} & \text{if } \mathbf{h}_{i-1} = 1 \\ \mathbf{r}_{i-1} + 1 & \text{if } \mathbf{h}_{i-1} = 0, \end{cases} \quad (5.9)$$

where \mathbf{g} is a list of relevant cells; $a_i \in \mathbf{a}$; \mathbf{h} and \mathbf{r} represent hit and rank, respectively; and each hit is rewarded based on its position in the ranked list. Last, we evaluate the models on F1 score [119], which is simply the harmonic mean between recall and precision of the relevant cells.

5.2.4 Experimental Results

Performances on the Synthetic Datasets \mathcal{D}_{syn} :

We compare the performance of our model SOS – EW against competitive baseline methods, UCB1 and SpUCB, in terms of $\overline{\text{reward}}$ when applied to synthetic datasets \mathcal{D}_{syn} with different spatio-temporal patterns. The results of $\overline{\text{reward}}$ are presented in Figure 5.3. Figure 5.3 demonstrates the $\overline{\text{reward}}$ under different ω , while ϕ and σ while fixing the other parameters. Our SOS – EW outperforms the other baselines by a large margin, with the ex-

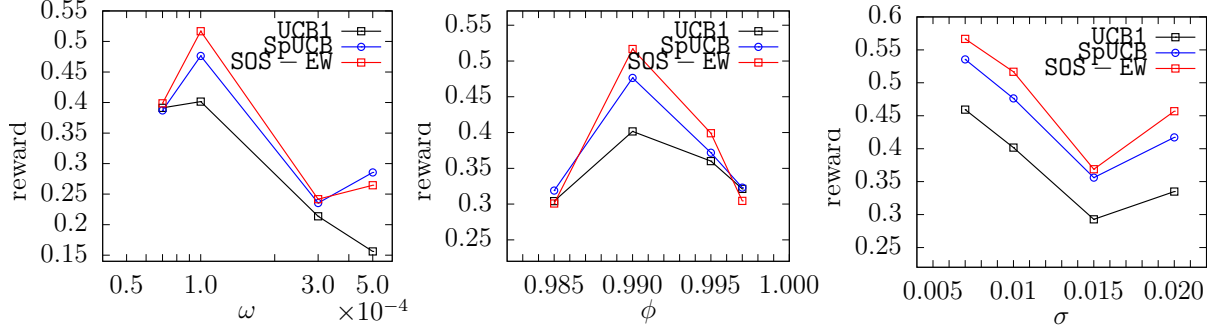


Figure 5.3. Performance on $\overline{\text{reward}}$ on \mathcal{D}_{syn} under different simulation scenarios with various of ω , ϕ and σ . We run simulations by changing only one of the parameters at a time and the other parameters, i.g., ω , ϕ and σ , are fixed at 10^{-4} , 0.99 and 10^{-2} , respectively.

Table 5.1. Best Performance on \mathcal{D}_{Hry}

Model	$\overline{\text{reward}}$	NDCG	mRHR	f1
ϵ Gdy	$0.302 \pm .059$	$0.309 \pm .116$	$0.169 \pm .050$	$0.277 \pm .050$
UCB1	$0.393 \pm .063$	$0.399 \pm .058$	$0.213 \pm .028$	$0.357 \pm .036$
UCB1 _{HpSp}	$0.426 \pm .047$	$0.438 \pm .028$	$0.243 \pm .017$	$0.385 \pm .015$
SpUCB	$0.435 \pm .076$	$0.411 \pm .070$	$0.210 \pm .041$	$0.365 \pm .025$
SOS – EW	$0.511 \pm .072$	$0.510 \pm .055$	$0.272 \pm .011$	$0.413 \pm .013$

ception of when the process is approximately stationary over moderate time scales. This occurs when ϕ or ω are too small or too large relative to the time scale of a visit, and in this scenario the Hawkes process loses its advantage over stationary models.

Performances on Houston 311 Service Requests \mathcal{D}_{Hry} :

Table 5.1 presents the best performance and its standard deviation of Houston 311 call dataset \mathcal{D}_{Hry} according to each evaluation metric. In general, our model SOS – EW outperforms all of the other baselines in every metric that we evaluate. In particular, by adding an event intensity tracking mechanism in the decision-making, the performance of SOS – EW is better than SpUCB both on reward optimization and high-risk cell recommendation. In terms of $\overline{\text{reward}}$, the proposed SOS – EW outperforms the second-best model, SpUCB, by 17.47% while it also surpasses SpUCB in NDCG by 24.09% from the ranking perspective. From the high-risk cell retrieval point of view, SOS – EW consistently outperforms SpUCB in mRHR and f1 by 29.52% and 13.15%, respectively. These improvements in accuracy illustrate SOS – EW’s

ability to recall events through event intensity tracking and provide better recommendations on the high-risk cells. By combining the method with the existing algorithm, stationary patterns of events are also taken into consideration and the combined model strikes a good balance between the \mathcal{HP} component and the other UCB component.

Compared to UCB1, $\text{UCB1}_{\text{HPSP}}$ contains the proposed \mathcal{HP} component. We can see from Table 5.1 that $\text{UCB1}_{\text{HPSP}}$ consistently outperforms UCB1 in all of the evaluation metrics. These results suggest that our proposed \mathcal{HP} component is out-performing traditional stationary MAB algorithms like UCB1 by tracking the space-time dynamic reward distribution.

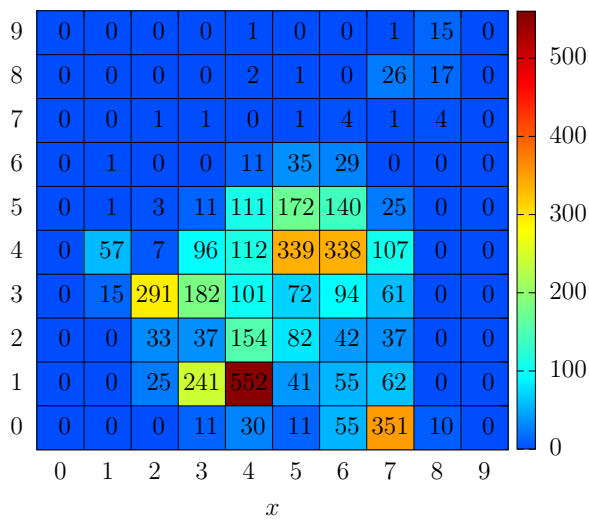


Figure 5.4. Number of events

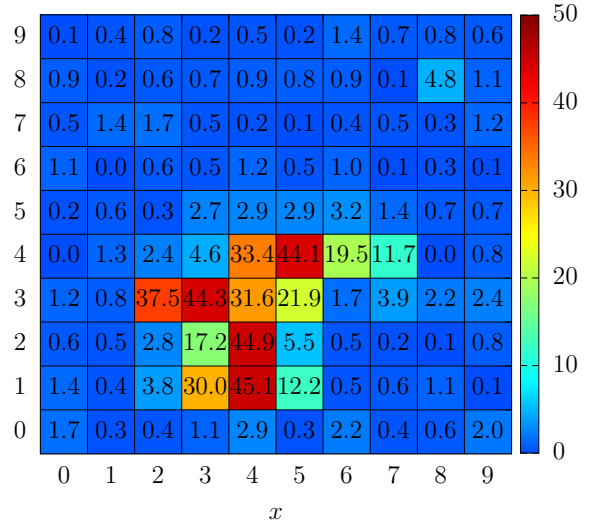


Figure 5.5. Number of visits

In Figure 5.4 and Figure 5.5, we compare the number of flooding events and the average number of total visits for each grid cell in \mathcal{D}_{Hry} among the first 10 MAB simulations from the best $\overline{\text{reward}}$ in our model $\text{SOS} - \text{EW}$. We can see that the number of flooding events in the cells is highly correlated to the average number of visits at the end of the MAB process. This suggests that after the trial of exploration, eventually, our $\text{SOS} - \text{EW}$ will learn those cells that are most susceptible to flooding and focus on these in terms of exploitation. Figure 5.6 is the snapshot of the flooding map in cell (4,1), that $\text{SOS} - \text{EW}$ gives the highest ranking on average. It is located by the watershed of The Brays Bayou, a slow-moving river which is notorious for its flooding history in Houston, Texas. This also indicates that $\text{SOS} - \text{EW}$ can identify hotspot areas for further investigation.

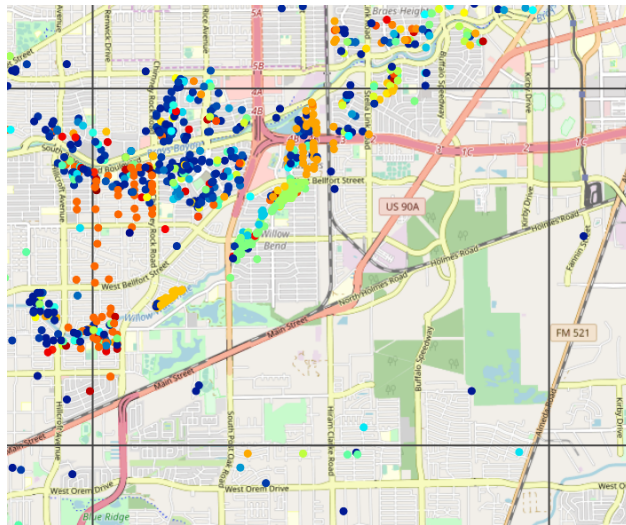


Figure 5.6. Map on (4,1)

Performances on IED Attack Reports \mathcal{D}_{IED} :

In table 5.2, we present the best performance and standard deviations of IED attack dataset \mathcal{D}_{IED} . Overall, the proposed **SOS – EW** consistently outperform all the other baseline methods in all four metrics while the competitive baseline **SpUCB** comes in second. In terms of $\overline{\text{reward}}$ and **NDCG**, **SOS – EW** improves 9.89% and 10.08% compared to **SpUCB**, respectively by a large margin. On the other hand, compared to $\overline{\text{reward}}$ and **NDCG**, our **SOS – EW** only has slight improvements on **mRHR** and **f1** (i.e., 4.23% and 2.04%, respectively) over **SpUCB**. This may be due to the fact that in \mathcal{D}_{IED} , there is a larger amount of grid cells and the bomb incidents are more evenly spread, which could cause the lack of quality on the recommendation of high-risk cells.

Table 5.2. Best Performance on \mathcal{D}_{IED}

Model	$\overline{\text{reward}}$	NDCG	mRHR	f1
ϵ -Gdy	$0.174 \pm .055$	$0.186 \pm .079$	$0.047 \pm .008$	$0.107 \pm .015$
UCB1	$0.122 \pm .016$	$0.169 \pm .028$	$0.028 \pm .004$	$0.082 \pm .004$
UCB1 _{HpSp}	$0.070 \pm .006$	$0.099 \pm .011$	$0.026 \pm .002$	$0.075 \pm .004$
SpUCB	$0.455 \pm .152$	$0.446 \pm .142$	$0.071 \pm .010$	$0.147 \pm .013$
SOS – EW	$0.500 \pm .154$	$0.491 \pm .139$	$0.074 \pm .009$	$0.150 \pm .013$

5.3 Conclusion

We introduced a novel framework **SOS – EW** that integrates Bayesian Hawkes processes (\mathcal{HP}) with a spatial multi-armed bandit (MAB) algorithm to forecast spatio-temporal events and detect hotspots where disaster search and rescue efforts may be directed. In particular, the model forecasts synthetic events between each visit to a geographical area to infer the intensity in the gap between between visits. An upper confidence bound on the estimated intensity is then built for dynamic event tracking. We then apply a Gaussian filter to incorporate the spatial relationships between grid cells. We compared our **SOS – EW** against competitive baselines through extensive experiments. In simulated synthetic datasets with space-time clustering, our **SOS – EW** improves upon existing stationary spatial MAB algorithms. In the case of Houston 311 service requests during hurricane Harvey and IED attack

reports in Iraq, **SOS – EW** outperforms the baseline models considered in terms of a variety of metrics including total reward and ranking quality. Overall, with the \mathcal{HP} component, we can enhance the performance of MAB algorithms. In the future, more contextual information may be used to further improve point process MAB algorithms. Furthermore, other types of point processes (log-Gaussian Cox processes, self-avoiding processes, etc.) may be combined with multi-armed bandits to solve other types of applications.

6. HAWKES PROCESS MODELING OF COVID-19 WITH MOBILITY LEADING INDICATORS AND SPATIAL COVARIATES

6.1 Hawkes Process Model of COVID-19 Transmission

In this section, we introduce a Hawkes process with spatio-temporal covariates for modeling COVID-19 case and death data. We then discuss the connection of the model to compartment models used in epidemiology and develop an expectation-maximization algorithm for inference.¹

6.1.1 Incorporating Covariates into the Hawkes Process

We propose a novel Hawkes process model that simultaneously estimates the intensity of events and tracks the dynamic reproduction number of the virus. Given the timestamps (or dates), $\mathcal{T} = \{t_1, t_2, \dots, t_n\}$, of daily reported positive test cases or deaths, we model the rate of new cases (or deaths) in each country c as follows:

$$\lambda_c(t) = \mu_c + \sum_{\substack{t > t_j \\ t_j \in \mathcal{T}}} R(\mathbf{x}_c^{t_j - \Delta}, \theta) w(t - t_j), \text{ where } \mathbf{x}_c^{t_j - \Delta} = \begin{bmatrix} \mathbf{d}_c \\ \mathbf{m}_c^{t_j - \Delta} \end{bmatrix}, \quad (6.1)$$

where μ_c is the background rate modeling imported infections, $w(t)$ is the inter-infection time distribution, $\mathbf{m}_c^t = [m_1^t, m_2^t, \dots]^\top$ are mobility indices on day t , and $\mathbf{d}_c = [d_1, d_2, \dots]^\top$ are static demographic features. The time-varying reproduction number $R(\mathbf{x}_c^{t_j - \Delta}, \theta)$ is a function of mobility indices and demographic features. It can be interpreted as the average number of secondary infections caused by a primary infection. Because we are modeling reported infections rather than time of exposure, we introduce the parameter Δ to capture a potential lag between a mobility change and the time t_j of a reported primary infection. Here, we combine the spatial and temporal covariates, and we model the dynamic reproduction

¹↑This work is accepted by International journal of forecasting. Chiang, Wen-Hao, Xueying Liu, and George Mohler. "Hawkes process modeling of COVID-19 with mobility leading indicators and spatial covariates." *International journal of forecasting* 38.2 (2022): 505-520.

number through a Poisson regression (Equation 6.2) where the coefficients θ are shared across the counties:

$$R(\mathbf{x}_c^{t_j-\Delta}, \theta) = \exp(\theta^\top \mathbf{x}_c^{t_j-\Delta}). \quad (6.2)$$

Our approach is related to those in recent preprints that incorporate mobility into compartment models [40], [120], however those approaches typically involve large-scale Monte Carlo simulations when performing inference. As we will show, the Hawkes process likelihood can be maximized without simulation via an efficient expectation-maximization algorithm.

6.1.2 Mathematical Connection between Hawkes Processes and Compartmental Models

Here we briefly review several variations of the Hawkes process in Equation 6.1 that can be connected to SEIR-type compartment models. The first variant is the SIR-Hawkes process. This model captures the long-term evolution of a pandemic by incorporating a pre-factor that accounts for the dynamic decrease in the number of susceptible individuals [42]:

$$\lambda^{\text{SIR}}(t) = \left(1 - \frac{I_c(t)}{N}\right) \left(\mu + \sum_{t_i < t} R_0 w(t - t_i)\right). \quad (6.3)$$

Here $I_c(t)$ is the cumulative number of infections that have occurred up to time t and N is the total population size. The point process governed by Equation 6.3 is a continuous time analog of a discrete stochastic SIR model when $w(t)$ is specified to be exponential [42]. When $w(t)$ is chosen to be gamma distributed, the Hawkes process also can approximate staged compartment models, like SEIR, if the average waiting time in each compartment is equal [121]. More complex parametric (or non-parametric) inter-infection time distributions $w(t)$ may be employed within the Hawkes process framework in situations where disease dynamics cannot be captured by a SIR or SEIR model. In the early exponential growth stage of an epidemic, before finite population effects play a role, the Hawkes process in Equation 6.1 without the prefactor can be used to model new infections arising from SIR and SEIR models, as $\frac{I_c(t)}{N}$ will be small.

While a pre-factor in the Hawkes process involving the cumulative number of infections is necessary to model long-term disease dynamics, in the early stages of transmission a linear Hawkes process can be used (as the prefactor will be close to 1),

$$\lambda(t) \approx \mu + \sum_{t_i < t} R_0 w(t - t_i). \quad (6.4)$$

To illustrate this, we simulate a SEIR differential equation,

$$\begin{aligned} \frac{dS}{dt} &= -\beta \frac{SI}{N}, & \frac{dR}{dt} &= \gamma I \\ \frac{dE}{dt} &= \beta \frac{SI}{N} - \mu E, & \beta &= \gamma R_0 \\ \frac{dI}{dt} &= \mu E - \gamma I, \end{aligned} \quad (6.5)$$

where the parameters are chosen similar to those of COVID-19 estimates reported in [122], [123]. In particular we let $\gamma = .1$, $R_0 = 2$, $\mu = 1$, and $N = 5 \cdot 10^8$ and note that these parameters are not from any specific locations. We then fit the linear Hawkes process model in Equation 6.4 to new infections, μE , generated by the SEIR model. We use a non-parametric histogram estimator for $w(t)$ and find a close fit between the Hawkes process and the SEIR model in Figure 6.1.

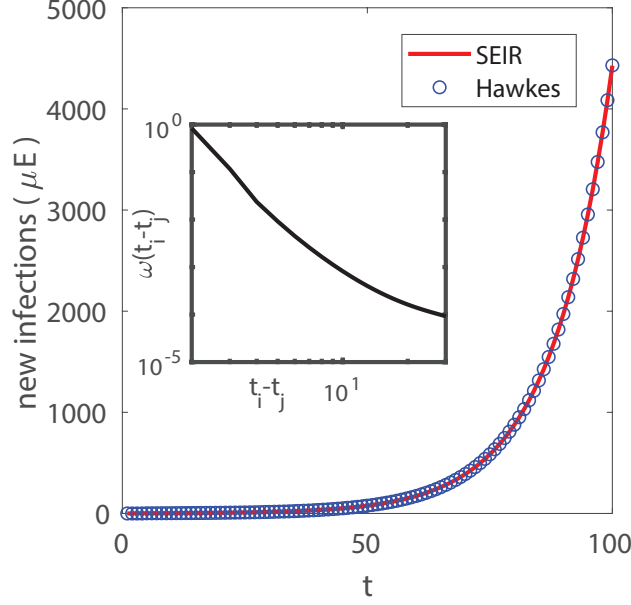


Figure 6.1. (Main figure) The red plot shows new infections (μE) from the SEIR differential equation $\frac{dS}{dt} = -\beta \frac{SI}{N}$, $\frac{dE}{dt} = \beta \frac{SI}{N} - \mu E$, $\frac{dI}{dt} = \mu E - \gamma I$, $\frac{dR}{dt} = \gamma I$, where $\beta = \gamma R_0$, $\gamma = .1$, $R_0 = 2$, $\mu = 1$, and $N = 5 \cdot 10^8$. The blue squares show the linear Hawkes process $\lambda_t = \mu + \sum_{t > t_i} R_0 w(t - t_i)$ fit to the SEIR curve of new infections. Inset: Non-parametric histogram estimate for $w(t)$.

In [42], the rate of events $\lambda(t)^{\text{SIR}}$ in a SIR-Hawkes process is established to be equal in expectation to new infections μE in the SEIR model after marginalizing out recovery events that are unobserved in a Hawkes process. In Figure 2, we show that in the early stage of spreading, the rate $\lambda(t)$ in a linear Hawkes process can also be used to approximate new infections μE .

6.1.3 EM Algorithm for Parameter Inference

We use an expectation-maximization (EM) algorithm to estimate the model in Equation 6.1, which has been widely used for Hawkes Process estimation [124]–[126]. First, we introduce latent random variables, $p_c(i, j)$, that represent the event that secondary infection i is

caused by primary infection j in county c . We let $p_c(i, i)$ represent the event that case i is imported. The complete data log-likelihood is then given by,

$$\mathcal{L} = \sum_{c=1}^{|C|} \left\{ \sum_{i=1}^n p_c(i, i) \log(\mu_c) - \int_0^T \mu_c dt + \sum_{j=1}^n \left\{ \sum_{i=j+1}^n p_c(i, j) \log[R(\mathbf{x}_c^{t_j-\Delta}, \theta) w(t_i - t_j | \alpha, \beta)] - \int_{t_j}^T R(\mathbf{x}_c^{t_j-\Delta}, \theta) w(t - t_j | \alpha, \beta) dt \right\} \right\}. \quad (6.6)$$

Here we use a Weibull distribution [127]–[129] with shape α and scale β to model inter-infection times, which we find accurately models the present data.

As the branching structure of the process is unobservable, we optimize the complete data log-likelihood in Equation 6.6 by iteratively alternating between an expectation step where the branching probabilities p_c are estimated and a maximization step where model parameters are updated by maximizing Equation 6.6. The EM-algorithm is equivalent to a projected gradient ascent on the likelihood of the Hawkes process [130].

Expectation Step

During the expectation step, we estimate the latent variables $p_c(i, j)$ for each county. Given the parameters θ , α , β , and μ_c estimated from the last iteration, the probabilities that case i was caused by case j (Equation 6.7a) or was imported (Equation 6.7b) are given by:

$$p_c(i, j) = \frac{R(\mathbf{x}_c^{t_j-\Delta}, \theta) w(t_i - t_j | \alpha, \beta)}{\lambda_c(t_i)}, \quad (6.7a)$$

$$p_c(i, i) = \frac{\mu_c}{\lambda_c(t_i)}. \quad (6.7b)$$

Note that the rate $\lambda_c(t_i)$ in Equation 6.1 is considered to be an aggregation of triggering kernels from all previous historical events (i.e., all $t < t_i$) and the background rate μ_c . Therefore, we can consider the probability of case i caused by case j , $p_c(i, j)$, as the contribution of primary infection j in the event rate at time t_i , i.e., $\lambda_c(t_i)$, and $p_c(i, i)$ can be seen as the contribution of the background rate.

Maximization Step

We then maximize the complete data log-likelihood with respect to the model parameters, conditioned on the estimated branching structure $p_c(i, j)$. During estimation we do not include event pairs (i, j) when j is within $\Psi = 14$ days of the last day of the dataset, as the offspring events i have not yet been realized and the inclusion of these incomplete data biases parameter estimates. We choose $\Psi = 14$ as the incubation period for COVID-19 is thought to extend to 14 days given by the Clinical Care Guidance from the CDC: <https://www.cdc.gov/coronavirus/2019-ncov/hcp/clinical-guidance-management-patients.html>. For simplicity, the summation over n in the likelihood function, Equation 5, is replaced with \hat{n} in the description for the maximization step. Here, \hat{n} represents the number of events that are within $T - \Psi$ ($\hat{n} = |t_i|t_i < T - \Psi|$).

Given the latent variable $p_c(i, j)$, the maximization of Equation 6.6 can be decoupled into three independent optimization problems. Starting with the coefficient θ from Poisson regression, the maximization of likelihood function can be rewritten as the following:

$$\hat{\theta} := \operatorname{argmax}_{\theta} \mathcal{L}_{\theta} = \sum_{c=1}^{|C|} \left\{ \sum_{j=1}^{\hat{n}} \left\{ P_c(j) \log \left[R(\mathbf{x}_c^{t_j - \Delta}, \theta) w(t_i - t_j | \alpha, \beta) \right] - \int_{t_j}^T R(\mathbf{x}_c^{t_j - \Delta}, \theta) w(t - t_j | \alpha, \beta) dt \right\} \right\}, \text{ where } P_c(j) = \sum_{i=j+1}^{\hat{n}} p_c(i, j). \quad (6.8)$$

Because the last Ψ days are removed from the dataset and we assume that all possible offspring pairs (i, j) have been observed, we can therefore approximate the integrals for the inter-infection time $w(t)$ in Equation 6.6 as is done in [131] by noting that $\int_{t_j}^T w(t - t_j | \alpha, \beta) \approx 1$. The optimization problem is therefore a Poisson regression, where we regress the observations $P_c(j) = \sum_{i=j+1}^{\hat{n}} p_c(i, j)$ against the covariates $\mathbf{x}_c^{t_j}$:

$$\hat{\theta} := \operatorname{argmax}_{\theta} \mathcal{L}_{\theta} = \operatorname{argmax}_{\theta} \sum_{c=1}^{|C|} \left\{ \sum_{j=1}^{\hat{n}} P_c(j) \theta^{\top} \mathbf{x}_c^{t_j - \Delta} - \exp(\theta^{\top} \mathbf{x}_c^{t_j - \Delta}) \right\}. \quad (6.9)$$

The same optimization strategy can be applied on the shape and scale parameters, α and β . The optimization problem can then be solved as a weighted maximum likelihood estimation for the Weibull shape and scale parameters:

$$\hat{\alpha}, \hat{\beta} := \operatorname{argmax}_{\alpha, \beta} \mathcal{L}_{\alpha, \beta} = \operatorname{argmax}_{\alpha, \beta} \sum_{c=1}^{|\mathcal{C}|} \left\{ \sum_{j=1}^{\hat{n}} \left\{ \sum_{i=j+1}^{\hat{n}} p_c(i, j) \log[w(t_i - t_j | \alpha, \beta)] \right\} \right\}. \quad (6.10)$$

where $p_c(i, j)$ is the weight of each inter-infection time observation $t_i - t_j$.

Third, the background rate μ_c is determined analytically:

$$\hat{\mu}_c := \operatorname{argmax}_{\mu_c} \mathcal{L}_{\mu_c} = \operatorname{argmax}_{\mu_c} \sum_{i=1}^{\hat{n}} p_c(i, i) \log(\mu_c) - \int_0^T \mu_c dt, \quad \hat{\mu}_c = \sum_{i=1}^{\hat{n}} \frac{p_c(i, i)}{T}. \quad (6.11)$$

Pseudo code for the EM algorithm is presented in the Algorithm 7.

Algorithm 7 EM algorithm optimization

```

1: procedure HkPRM+( $\mathcal{T}$ ,  $\mathbf{x}$ ,  $\Delta$ )
2:    $T \leftarrow \max \mathcal{T}$ ,  $\alpha \leftarrow 2$ ,  $\beta \leftarrow 2$ . ▷ Initialization
3:    $\mu_c \leftarrow 0.5$ ,  $R_c^t(t) \leftarrow 1$ ,  $\forall c \in \mathcal{C}$  and  $0 < t < T$ .
4:   while  $\|\Delta\theta\|, |\Delta\alpha|, |\Delta\beta|, \|\Delta\mu\| > \text{tol}$  do
5:     Expectation step:
6:     for  $\forall i \geq j$  and  $0 < i, j < T$  and  $\forall c \in \mathcal{C}$  do
7:       if  $i > j$  then
8:          $p_c(i, j) \leftarrow \frac{R_c^{t_j}(\mathbf{x}_c^{t_j - \Delta}, \theta) w(t_i - t_j | \alpha, \beta)}{\lambda_c(t_i)}$ .
9:       else if  $i = j$  then
10:         $p_c(i, i) \leftarrow \frac{\mu_c}{\lambda_c(t_i)}$ .
11:       end if
12:     end for
13:
14:     Maximization step:
15:      $\theta \leftarrow \operatorname{argmax}_{\theta} \sum_{c=1}^{|\mathcal{C}|} \left\{ \sum_{j=1}^n P_c(j) \theta^\top \mathbf{x}_c^{t_j - \Delta} - \exp(\theta^\top \mathbf{x}_c^{t_j - \Delta}) \right\}$ .
16:      $\alpha, \beta \leftarrow \operatorname{argmax}_{\alpha, \beta} \sum_{c=1}^{|\mathcal{C}|} \left\{ \sum_{j=1}^n \left\{ \sum_{i=j+1}^n p_c(i, j) \log[w(t_i - t_j | \alpha, \beta)] \right\} \right\}$ .
17:     for  $\forall c \in \mathcal{C}$  do
18:        $\mu_c \leftarrow \sum_{i=1}^n \frac{p_c(i, i)}{T}$ .
19:     end for
20:   end while
21: end procedure

```

We note that the EM algorithm of the Hawkes process is also connected to the dynamic reproduction number estimator of Wallinga and Teunis [132], as the latter can be viewed as a 1-iteration EM algorithm where a histogram estimator is used for R_c^t with initial guess $R_c^t \equiv 1$. More details are discussed in the following section.

6.1.4 Connection of EM algorithm for Hawkes Process and Dynamic R estimator of Wallinga and Teunis

Here we make the connection between the EM algorithm for the Hawkes process and the popular dynamic reproduction number estimator of Wallinga and Teunis [127], [132], [133]. The dynamic R estimator of Wallinga and Teunis is constructed as follows. The probability that individual i at time t_i was infected by individual j at time t_j is defined to be,

$$p_{ij} = \frac{w(t_i - t_j)}{\sum_{t_i > t_k} w(t_i - t_k)}, \quad (6.12)$$

where the distribution of inter-infection times $w(t_i - t_j)$ is typically modeled as Weibull, Gamma, or log-normal [127]. The expected total number of individuals that j infects is then given by:

$$R_j = \sum_{i > j} p_{ij}. \quad (6.13)$$

Wallinga and Teunis then obtain an estimate of the dynamic reproduction number $R(t)$ by averaging R_j over all observed cases j where the time of infection t_j occurred on day t :

$$R(t) = \frac{1}{N_t} \sum_{t \leq t_j < t+1} R_j, \quad (6.14)$$

(here N_t is the number of observed infections on day t).

On the other hand, for the Hawkes process the intensity (rate) of infections is modeled as

$$\lambda(t) = \mu + \sum_{t > t_i} R(t_i) w(t - t_i), \quad (6.15)$$

where $w(t)$ and $R(t)$ are the inter-infection time distribution and dynamic reproduction number respectively. Rather than modeling $R(t)$ as dependent on mobility, we can instead model $R(t)$ as a piece-wise constant function:

$$R(t) = \sum_{k=1}^B r_k 1\{t \in I_k\}. \quad (6.16)$$

Here the I_k are intervals discretizing time, B is the number of such intervals, and r_k is the estimated reproduction rate in interval k .

Given initial guesses for the model parameters and r_k , the EM algorithm for the Hawkes process iteratively updates the parameters and branching probabilities by alternating between the

E-step update:

$$p_{ij} = R(t_j)w(t_i - t_j)/\lambda(t_i) \quad (6.17)$$

$$p_{ii} = \mu/\lambda(t_i) \quad (6.18)$$

and **M-step update:**

$$w(t) \sim MLE(\{t_i - t_j; p_{ij}\}) \quad (6.19)$$

$$\mu = \sum_i p_{ii}/T \quad (6.20)$$

$$r_k = \sum_{t_i > t_j} p_{ij} 1\{t_j \in I_k\}/N_k \quad (6.21)$$

where T is the total length of the observation period, N_k is the total number of events in interval k , and the $w(t)$ is estimated via weighted MLE (for either a Gamma, Weibull or log-normal) using the inter-event times as observations and branching probabilities as weights. We also drop event pairs (i, j) when j is within $\Phi = 14$ days of the last day of the datasets in consideration of the incubation period.

Finally, we can compare Equation 6.17 to Equation 6.12. The dynamic $R(t)$ estimator in Equation 6.12 is what you obtain with 1 step of the EM algorithm in Equation 6.17 with initial guess $R(t) \equiv 1$, $\mu = 0$ and 1 day chosen as the bin width for the histogram estimator.

6.1.5 Hawkes Process Forecasting

We forecast future events using the branching process representation of the Hawkes process. We first simulate immigrant events through the Poisson process based on the background rate. For each event in the history of the process, we then simulate a Poisson random variable with mean $R(\mathbf{x}_c^{t_j-\Delta}, \theta)$ representing the number of secondary infections caused by event j . For each of these infections we simulate the time of infection by drawing inter-event times from the estimated Weibull distribution. For example, for an event on day 4, it may cause a secondary infection on day 22 if we draw a sample as 18 from the Weibull distribution. Events falling in the future (past the forecasting date) are then used to update the forecasted intensity through Equation 6.1. We simulate multiple realizations of this process (100 times in our application) to estimate a mean intensity forecast along with confidence intervals.

6.2 Experiments and Results

In this section we first provide details on the datasets and baseline models used in our experiments. We then discuss the experimental results of several COVID-19 retrospective forecasting tasks at the U.S. county level. The source code and dataset are included in the supplemental material and are available online in a anonymous repository².

6.2.1 Datasets

Covid-19 Daily Cases and Deaths Reported by The New York Times

The New York Times (NYT) [134]³ releases a daily report of the cumulative numbers of COVID-19 cases in the United States at the county level and over time. While NYT data

²<https://anonymous.4open.science/r/d425dcf9-3cfb-4f82-a08c-ee583ab36291/>

³<https://github.com/nytimes/covid-19-data>

closely tracks data aggregated by a project at Johns Hopkins University [135], NYT county level reporting started earlier and is therefore used in this study. In total, there are 3,217 counties with cases and/or deaths in the dataset. The time series data are compiled from state and local government health departments. In order to have sufficient data for statistical inference, we select the counties with confirmed cases greater than and equal to 10 (denoted by $\mathcal{D}_{\text{conf}}$) and the counties with at least 1 death (denoted by $\mathcal{D}_{\text{death}}$) by 11/10/2020 when the dataset is curated. In total, there are 2,824 and 2,545 counties in these two datasets. Parameter sharing may improve models in counties with less data through variance reduction, but can potentially bias estimates in more populated counties with more cases.

We therefore assess model performance over different subsets of counties grouped by case volume. We first rank counties by the number of confirmed cases and deaths by the cut-off date, 11/30/2020, and we then evaluate forecasting accuracy on the top-10% of counties (denoted by $Q_{10\%}^{\text{top}}$), the top-25% counties (denoted by $Q_{25\%}^{\text{top}}$), and counties between the top-25% and top-50% quantiles (denoted by $Q_{50\%}^{25\%}$).

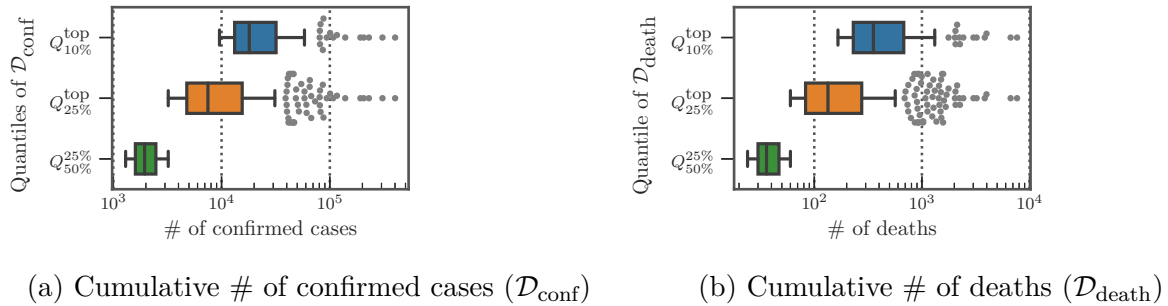


Figure 6.2. Distribution of cumulative cases reported at 11/30/2020 at different quantiles.

In Figure 6.2a and 6.2b, we present the distribution of the cumulative confirmed cases and deaths at three different quantiles up to the cut-off date 11/30/2020. As the counties at the top-50% have more than 1,000 confirmed cases and 10 deaths, some urban counties, mostly at the top-10%, had already surpassed 10,000 confirmed cases and accumulated more than 300 deaths. In Figure 6.3a and 6.3b, we show the daily reported confirmed cases and deaths of top-3 counties in $Q_{10\%}^{\text{top}}$ and $Q_{50\%}^{25\%}$ from $\mathcal{D}_{\text{conf}}$ and $\mathcal{D}_{\text{death}}$, respectively. Given different demographics and different COVID-19 regulations, each state went through different phases.

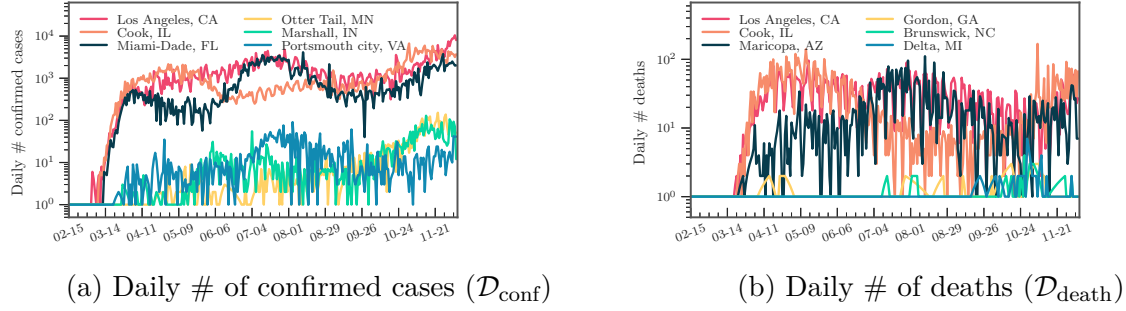


Figure 6.3. Example of the daily # of confirmed cases/deaths.

For example, while Cook, IL seemed to contain the first spike after May, the confirmed cases in Los Angeles, CA seem steadily increase and only slow down after July. The daily death toll of Maricopa, AZ only hit its record high only after August unlike Los Angeles, CA, which had already had their first wave in terms of deaths in April. Overall, the deaths are increasing as the U.S. heads into the winter months. Such differences in infection rates suggest that different public health and social measures may need to be tailored county by county. Therefore, the proposed county-level forecasting model may aid local government policymakers in understanding the demographic and mobility factors that play a role in local reproduction of the virus.

Google Mobility Index Reports

We use Google daily mobility index reports at the county level [136] to estimate a dynamic reproduction number that tracks changes in movement patterns due to stay at home orders (and their staged removal). In total, there are 6 mobility types, including grocery & pharmacy, parks, transit stations, retail & recreation, residential and workplaces. Mobility indices for each category and county are calculated with respect to a baseline value for that day of the week. The baseline day of the week is the median value from the 5-week period from 01/03/2020 to 02/06/2020. That is, the values are the relative number of visitors for counties in each category. Note that during the model training, we introduce the parameter Δ to capture a potential lag between a mobility change and the time t_j of a reported primary infection. As we make forecasts, we use the mobility in training data from the previous Δ

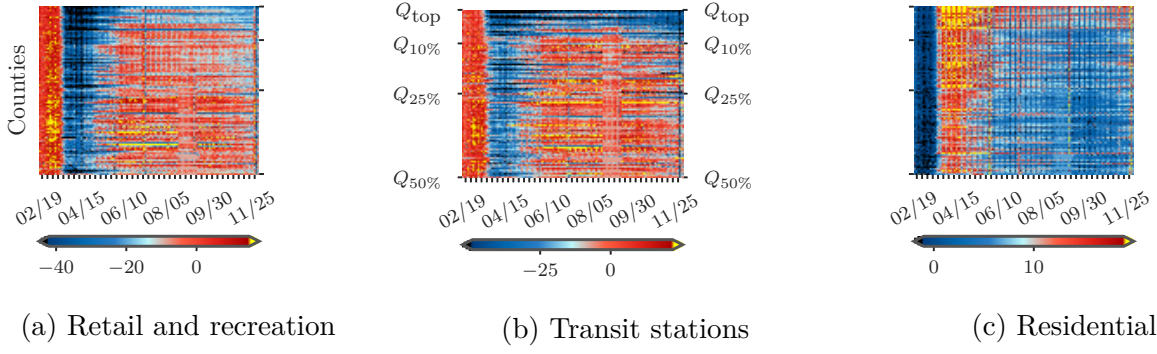


Figure 6.4. Heat map of mobility indices across counties in $\mathcal{D}_{\text{conf}}$ and over time.

days to infer the reproduction number. If the forecast target is more than Δ , we would use the most recent value from the day of the week in the training data.

We drop “workplace” mobility from our analysis due to high collinearity with “residential” mobility. Some mobility data are missing when data is sparse for a given date. To deal with missing values, we adopt multivariate feature imputation⁴, which estimates each missing mobility entry as a function of other mobility types on the same day in the same county. We show some heatmaps of mobility patterns across counties and time in the Figure 6.4, where a major change can be observed coinciding with stay at home orders (the first state-wide stay-at-home order was issued at 03/21/2020). Also, the reopening phase in most of the counties can be seen after May. For counties hit by COVID-19 the most (i.e., those in the top-10 %), we can also observe some strict regulations in the “Retail and recreation” areas and better compliance with stay-at-home orders based on high mobility in “Residential” area.

County-level Demographic Covariates

We incorporate spatial demographic features that may be predictive of symptomatic cases of COVID-19 (which are more likely to result in testing and mortality). The dataset is available in a curated form [137] and is derived from CDC and census datasets. The data is at the county level and includes population, median age, number of hospitals and ICU beds, percentage of smokers and diabetes, and heart disease mortality.

⁴<https://scikit-learn.org/stable/modules/impute.html#multivariate-feature-imputation>

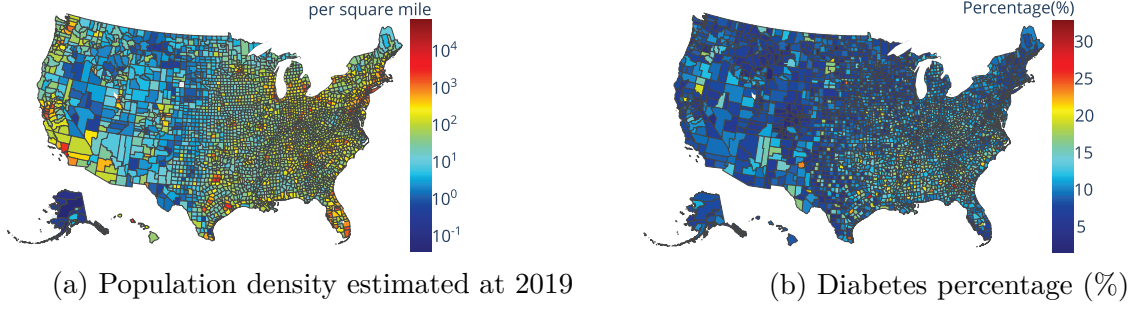


Figure 6.5. Examples of spatial demographic and health features at the county-level.

In Figure 6.5, we present two examples of spatial demographic features at the county-level used to model variations in the reproduction number. In Figure 6.5a we observe that both the east and west coasts of the United States are more densely populated compared to midwestern and western regions. Diabetes percentage (shown in Figure 6.5b), on the other hand, is mostly higher in southern regions of the U.S.

6.2.2 Baseline Models and Experimental Setup for Retrospective Forecasting Comparison

We compare the Hawkes process model in Equation 6.1 with several models including an SEIR model used in a pandemic tracking dashboard ⁵ out of Columbia University [38] (denoted by **PROJ**), an geospatial SEIR Model from the Johns Hopkins University Applied Physics Lab [40] (denoted by **BUCKY**), and an ensemble model with linear and exponential predictors from University of California, Berkeley [137] (denoted by **CLEP**). Note that all three competing models are tested directly from the released source code and we follow the same experimental protocol as for our proposed model. A simplified Hawkes process, denoted by **Hawkes**, where the reproduction number is held constant is used for comparison to demonstrate the effectiveness of tracking the reproduction number dynamically. We also compare our full Hawkes process model, denoted by \mathbf{HkPR}_m^+ , to a Hawkes process, \mathbf{HkPR}_m , with only mobility features to determine the marginal improvement of adding demographics.

We backtest the six competing models on the $\mathcal{D}_{\text{conf}}$ and $\mathcal{D}_{\text{death}}$ datasets using the “walk-forward” validation approach. In particular, for 7-day forecasts we first train the models

⁵<https://covid19forecasthub.org/community/>

based on cases and deaths before the first cut-off date, 04/15/2020, and then forecast through 04/21/2020. We then slide the forecasting window, training on data before 4/22/2020 and forecasting from 04/22/2020 to 04/28/2020. We repeat this process until the final date of 05/19/2020 (a similar approach is used for 14 and 28 day forecasts). The multivariate imputation models are also trained in the same walk forward fashion to avoid possible data leakage. The hyper-parameter of the lag parameter Δ ranges from 7, 14, 21, and 28 days in our experiments. For each of the forecasts, we simulate them 100 times and the point estimate is made through the average.

We evaluate the models according to mean absolute error, **MAE**, averaged across counties and forecasting windows of the same length, along with percentage error, **PE**. Mean absolute error (**MAE**) and the percentage error (**PE**) are calculated as follows:

$$\text{MAE} = \frac{\sum_{c=1}^{|C|} |n_c - \hat{n}_c|}{|C|}, \text{ PE} = \frac{|\sum_{c=1}^{|C|} n_c - \sum_{c=1}^{|C|} \hat{n}_c|}{\sum_{c=1}^{|C|} \hat{n}_c}, \quad (6.22)$$

where \hat{n}_c , and n_c are the number of reported events and predicted events, respectively. We also compare the ranking quality of the competing models using Normalized Discounted Cumulative Gain (**NDCG**) [118], which can be used to evaluate the power of recommendations for counties with potential COVID-19 spikes in the near future.

6.2.3 Experimental Results

Table 6.1. MAE on predicted confirmed cases $\mathcal{D}_{\text{conf}}$

Model	7-days			14-days			28-days		
	$Q_{10\%}^{\text{top}}$	$Q_{25\%}^{\text{top}}$	$Q_{50\%}^{25\%}$	$Q_{10\%}^{\text{top}}$	$Q_{25\%}^{\text{top}}$	$Q_{50\%}^{25\%}$	$Q_{10\%}^{\text{top}}$	$Q_{25\%}^{\text{top}}$	$Q_{50\%}^{25\%}$
PROJ	809.40	415.88	55.30	1664.90	857.93	117.86	3432.57	1779.56	252.43
CLEP	238.30	134.83	33.86	585.81	324.32	88.87	1963.52	1090.36	207.81
BUCKY	404.49	212.80	37.45	883.69	459.77	89.85	2085.88	1116.91	229.33
Hawkes	224.35	120.61	24.02	569.49	300.06	55.45	1803.63	935.83	165.92
HkPR_m	211.59	114.34	22.44	519.00	271.86	49.83	1573.58	835.59	136.60
HkPR_m⁺	210.72	114.69	22.38	522.92	276.28	49.86	1611.48	893.65	132.79

The best performance is marked in **bold**.

Table 6.2. MAE on predicted confirmed cases $\mathcal{D}_{\text{death}}$

Model	7-days			14-days			28-days		
	$Q_{10\%}^{\text{top}}$	$Q_{25\%}^{\text{top}}$	$Q_{50\%}^{25\%}$	$Q_{10\%}^{\text{top}}$	$Q_{25\%}^{\text{top}}$	$Q_{50\%}^{25\%}$	$Q_{10\%}^{\text{top}}$	$Q_{25\%}^{\text{top}}$	$Q_{50\%}^{25\%}$
PROJ	15.56	7.89	1.12	30.66	15.55	2.20	56.85	29.37	4.41
CLEP	10.96	5.83	1.16	19.10	10.58	2.31	78.17	42.99	8.56
BUCKY	8.23	4.55	1.00	16.07	8.70	1.83	29.55	16.56	3.98
Hawkes	8.49	4.59	1.04	17.38	9.18	1.98	47.13	24.29	4.32
HkPR_m	7.19	4.07	1.01	13.40	7.55	1.78	33.30	18.23	3.74
HkPR_m⁺	7.24	4.07	1.01	13.68	7.53	1.77	35.99	19.18	3.60

The best performance is marked in **bold**.

Table 6.3. PE on predicted confirmed cases $\mathcal{D}_{\text{conf}}$

Model	7-days			14-days			28-days		
	$Q_{10\%}^{\text{top}}$	$Q_{25\%}^{\text{top}}$	$Q_{50\%}^{25\%}$	$Q_{10\%}^{\text{top}}$	$Q_{25\%}^{\text{top}}$	$Q_{50\%}^{25\%}$	$Q_{10\%}^{\text{top}}$	$Q_{25\%}^{\text{top}}$	$Q_{50\%}^{25\%}$
PROJ	91.00	90.40	84.07	94.41	94.63	92.83	95.76	96.17	96.94
CLEP	10.23	12.08	41.09	24.60	29.42	90.24	41.19	47.74	515.17
BUCKY	19.61	20.12	35.58	28.05	27.90	69.61	47.91	49.24	97.86
Hawkes	11.52	11.31	14.36	17.33	17.02	19.60	41.25	40.06	39.11
HkPR_m	11.72	10.75	15.44	13.92	15.10	15.08	38.77	38.20	46.38
HkPR_m⁺	10.16	10.35	12.95	15.30	13.45	16.91	41.96	33.33	41.31

The best performance is marked in **bold**.

In Table 6.1 and Table 6.2, we present the experimental results for 7, 14, and 28 days window forecasts of MAE for all models applied to both confirmed cases ($\mathcal{D}_{\text{conf}}$) and deaths ($\mathcal{D}_{\text{death}}$), and in Table 6.3 and Table 6.4, we report the results for PE. In terms of MAE and PE, both of our proposed models, **HkPR_m** and **HkPR_m⁺**, outperform the models, **PROJ** and **CLEP**, by a large margin in all three forecasting periods and across quantile subsets of the data. The improvements of MAE and PE can also be seen in the simplistic baseline Hawkes process, **Hawkes**. This suggests that the Hawkes process approach has a good potential on modeling infectious disease due to the self-exciting properties that lie in the COVID-19 cases.

We found that adding mobility indices improves **Hawkes**, where forecasting accuracy of **HkPR_m** also increases across the subsets and all forecasting window. For example, the improvements on MAE over **Hawkes** can go up to 13%, 11%, and 18% for 28 days forecast when **HkPR_m** is applied to $Q_{10\%}^{\text{top}}$, $Q_{25\%}^{\text{top}}$, and $Q_{50\%}^{25\%}$ in $\mathcal{D}_{\text{conf}}$, respectively. Similar decrease

Table 6.4. PE on predicted confirmed cases $\mathcal{D}_{\text{death}}$

Model	7-days			14-days			28-days		
	$Q_{10\%}^{\text{top}}$	$Q_{25\%}^{\text{top}}$	$Q_{50\%}^{25\%}$	$Q_{10\%}^{\text{top}}$	$Q_{25\%}^{\text{top}}$	$Q_{50\%}^{25\%}$	$Q_{10\%}^{\text{top}}$	$Q_{25\%}^{\text{top}}$	$Q_{50\%}^{25\%}$
PROJ	72.56	72.25	45.10	81.93	81.96	73.62	90.21	90.53	87.16
CLEP	23.39	26.35	18.05	19.23	19.27	24.74	73.77	78.90	173.88
BUCKY	17.64	16.08	14.71	15.63	13.93	20.22	15.36	13.20	36.19
Hawkes	17.97	16.99	15.81	20.03	20.71	16.17	48.79	44.15	28.17
HkPR_m	16.77	15.59	13.80	20.40	17.38	13.72	33.03	52.51	22.04
HkPR_m⁺	17.53	16.92	14.05	18.18	15.23	16.93	38.31	44.78	17.66

The best performance is marked in **bold**.

on MAE can be observed when **HkPR_m** is applied to three quantile subsets in $\mathcal{D}_{\text{death}}$, where **HkPR_m** outperforms **Hawkes** by 29%, 25%, and 13% in MAE, respectively. In terms of PE, **HkPR_m** stays ahead of **Hawkes** with only one exception at $Q_{50\%}^{25\%}$ of $\mathcal{D}_{\text{death}}$ in 28 days forecasting. This shows that by modeling the reproduction number through daily mobility indices we can enhance the forecasting accuracy and obtain more precise estimation on the spikes in the future.

By adding demographic features, we can marginally boost the MAE and PE of **HkPR_m⁺** over **HkPR_m** in some cases. In general, the variation, **HkPR_m⁺**, also shows similar improvements over the competing models. In particular, **HkPR_m⁺** has the best PE enhancement over **HkPR_m** at $Q_{50\%}^{25\%}$ in $\mathcal{D}_{\text{death}}$ for 28 days forecast, which is 20%. This demonstrates that the major forecasting power comes from the joint modeling of mobility indices in the reproduction number while the choices of the background rate and inter-infection distribution may only play a minor part.

Moreover, we notice that model **BUCKY** is a competitive baseline in $\mathcal{D}_{\text{death}}$ where it has better accuracy in a few cases, such as MAE and PE $Q_{10\%}^{\text{top}}$ and $Q_{25\%}^{\text{top}}$ for 28 days forecast. Possible explanation for its advantage could be the CDC-recommended parameters that has been introduced to aid the model training especially for recovery and deaths compartments in its SEIR model. Those parameters include case fatality ratio, case hospitalization ratio, time between death and reporting, etc. However, introducing such pre-trained parameters from CDC may not be practical in real-time forecasting and may potentially bring in the data leakage issue.

Table 6.5. NDCG on predicted confirmed cases $\mathcal{D}_{\text{conf}}$

Model	7-days			14-days			28-days		
	$Q_{10\%}^{\text{top}}$	$Q_{25\%}^{\text{top}}$	$Q_{50\%}^{25\%}$	$Q_{10\%}^{\text{top}}$	$Q_{25\%}^{\text{top}}$	$Q_{50\%}^{25\%}$	$Q_{10\%}^{\text{top}}$	$Q_{25\%}^{\text{top}}$	$Q_{50\%}^{25\%}$
PROJ	0.7225	0.7039	0.8232	0.6946	0.6793	0.8412	0.6696	0.6614	0.8589
CLEP	0.9626	0.9526	0.8620	0.9418	0.9402	0.8704	0.9015	0.8843	0.8739
BUCKY	0.9283	0.9279	0.8600	0.9269	0.9216	0.8768	0.9013	0.8957	0.8813
Hawkes	0.9738	0.9757	0.8680	0.9697	0.9704	0.8926	0.9414	0.9419	0.8879
HkPR_m	0.9706	0.9728	0.8673	0.9715	0.9755	0.8956	0.9502	0.9521	0.8958
HkPR_m⁺	0.9734	0.9759	0.8672	0.9752	0.9758	0.8932	0.9493	0.9503	0.8918

The best performance is marked in **bold**.

Table 6.6. NDCG on predicted confirmed cases $\mathcal{D}_{\text{death}}$

Model	7-days			14-days			28-days		
	$Q_{10\%}^{\text{top}}$	$Q_{25\%}^{\text{top}}$	$Q_{50\%}^{25\%}$	$Q_{10\%}^{\text{top}}$	$Q_{25\%}^{\text{top}}$	$Q_{50\%}^{25\%}$	$Q_{10\%}^{\text{top}}$	$Q_{25\%}^{\text{top}}$	$Q_{50\%}^{25\%}$
PROJ	0.6746	0.6607	0.7057	0.6823	0.6529	0.7666	0.7003	0.6837	0.8050
CLEP	0.9126	0.9010	0.7451	0.9095	0.8945	0.7849	0.8696	0.8240	0.8043
BUCKY	0.9161	0.9160	0.7301	0.9217	0.9222	0.7797	0.9074	0.9095	0.8278
Hawkes	0.9506	0.9493	0.7548	0.9475	0.9469	0.8011	0.9293	0.9297	0.8212
HkPR_m	0.9491	0.9476	0.7598	0.9446	0.9457	0.8007	0.9299	0.9315	0.8195
HkPR_m⁺	0.9504	0.9474	0.7597	0.9502	0.9514	0.7963	0.9368	0.9372	0.8176

The best performance is marked in **bold**.

In Table 6.5 and Table 6.6, we present the NDCG results for the ranking evaluation. Generally, the proposed models SOS – EW have a better NDCG performance when applied to confirmed cases for most of the quantile subsets. In terms of NDCG on the $\mathcal{D}_{\text{death}}$ dataset, the baseline Hawkes process, **Hawkes**, performs better in some cases but proposed method consistently comes in second for most of the forecasting window. By generating rankings with good qualities, SOS – EW can serve as a recommender system for the hotspot counties and the public health policymakers can tailor strategies specifically for each region to contain the virus. We also note that in our model, we are estimating inter-event distributions of observed cases (ignoring asymptomatic cases) and therefore these are observed or “effective” inter-event distributions, rather than true inter-infection distributions based on longitudinal data. We believe this approach is justified by the performance of the model in forecasting observed cases (and this approach is taken in other applications, like seismology where some earthquakes are not observed).

Table 6.7. Model coefficients
($\mathcal{D}_{\text{conf}}$)

Covariate	coef	pValue
Retail/recreation	0.1303	0
Grocery/pharmacy	0.0029	8.46×10^{-09}
Transit stations	-0.0102	1.56×10^{-98}
Parks	-0.0355	0
Residential	-0.1063	0
Population density	0.0220	0
# ICU beds	0.0110	1.20×10^{-247}
# hospitals	0.0106	8.69×10^{-128}
Median age	-0.0049	3.85×10^{-38}
Population est.	-0.0214	0
Smokers %	-0.0361	0
Heart disease mort.	-0.0453	0
Diabetes %	-0.0589	0

The first 5 covariates are mobility indices, followed by static demographic covariates and two types of coefficients are sorted, respectively.

Table 6.8. Model coefficients
($\mathcal{D}_{\text{death}}$)

Covariate	coef	pValue
Retail/recreation	0.1047	4.15×10^{-118}
Grocery/pharmacy	0.0746	8.88×10^{-111}
Transit stations	0.0276	2.48×10^{-11}
Residential	-0.0929	5.04×10^{-212}
Parks	-0.1294	0
# ICU beds	0.0423	2.17×10^{-64}
Population density	0.0409	0
Population est.	0.0062	5.18×10^{-2}
Median age	-0.0157	1.65×10^{-7}
Heart disease mort.	-0.0250	1.29×10^{-8}
# hospitals	-0.0423	6.54×10^{-28}
Diabetes %	-0.1041	1.33×10^{-86}
Smokers %	-0.1448	1.65×10^{-279}

The first 5 covariates are mobility indices, followed by static demographic covariates and two types of coefficients are sorted, respectively.

Importance of Covariates

In Table 6.7 and Table 6.8, we show the dynamic reproduction number coefficients of HkPR_m^+ estimated from the Poisson regression component (Equation 6.2) when applied to $\mathcal{D}_{\text{conf}}$ and $\mathcal{D}_{\text{death}}$, respectively. The p-value is calculated from the Poisson regression analysis in the M-step after the EM algorithm reaches convergence. The absolute value of the coefficients indicates the magnitude of the correlation between the reproduction number and the features. With the exception of population estimation in $\mathcal{D}_{\text{death}}$, the coefficients of all variables are statistically significant at the 10^{-7} level or below. The dynamic reproduction number is positively correlated with “Retail and recreation” while negatively correlated with “Residential”, meaning that as mobility shifted away from commercial areas towards residences, the reproduction number decreased. In terms of spatial covariates, the reproduction number is positively correlated with “Population density” and “# of ICU beds.” This suggests that the regions hit the hardest by COVID-19 are mostly urban areas, where most of intensive treatment units are situated. The reproduction number is also negatively correlated with percent of the population with “Diabetes” and “Heart disease mortality rate.” Several possible explanations for this observation include high-risk individuals are being more cautious or that they tend to live in areas with less cases, potentially with less population.

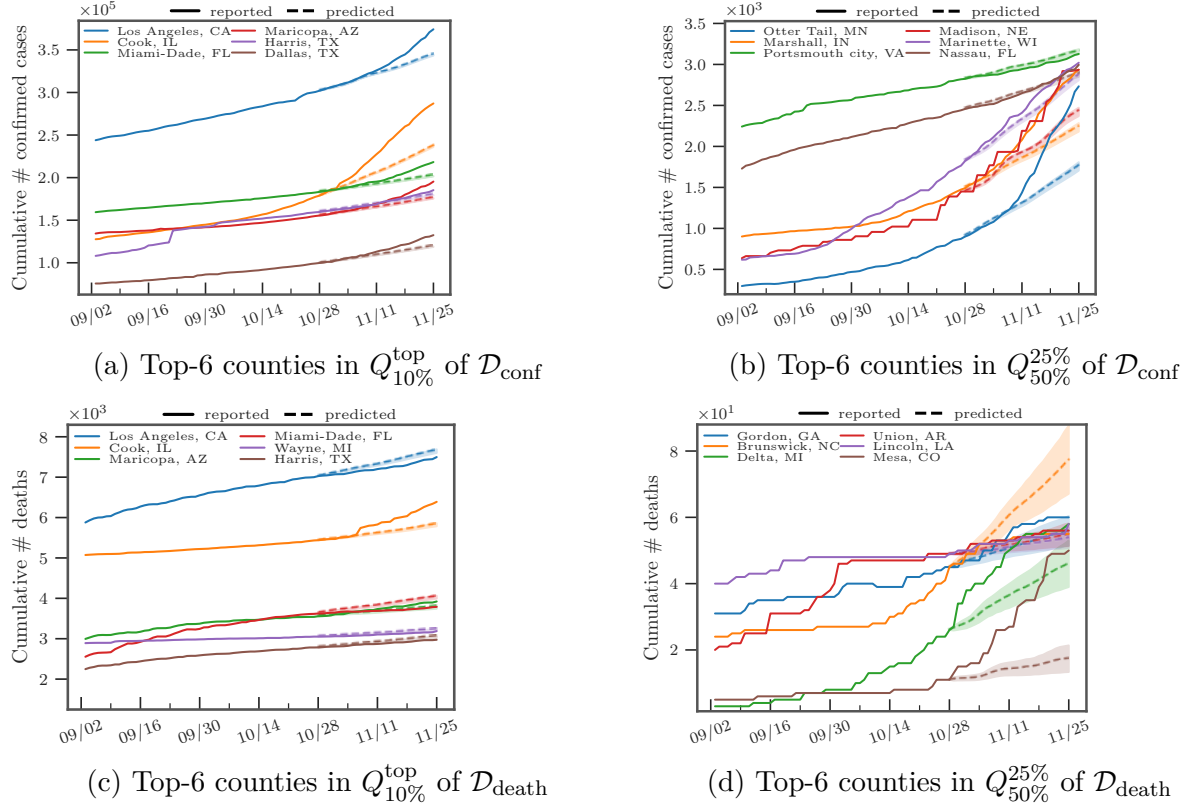


Figure 6.6. Forecasting for 28 days from 10/28/2020 - 11/25/2020

COVID-19 Forecasting and Reproduction Number Analysis

In Figure 6.6, we present an example of 28 days projection made through \mathbf{HkPR}_m^+ from 10/28/2020 - 11/25/2020 for both $\mathcal{D}_{\text{conf}}$ and $\mathcal{D}_{\text{death}}$. We can observe that \mathbf{HkPR}_m^+ has very promising results in making projections, especially for the short term future, When the number of forecasting windows increases, the forecasting error increase as the task also being more difficult. Moreover, the narrow confidence interval calculated through 100 Hawkes processes simulations suggests that the the proposed model can make relatively stable forecasting. Lastly, based on the projections, as the number of confirmed cases soon would hit over 500,000 in the top counties including Los Angeles, CA, Cook, IL, and etc. It is imperative to have a robust framework to help governments to design strategies to combat COVID-19 or even more, prioritize vaccine distribution.

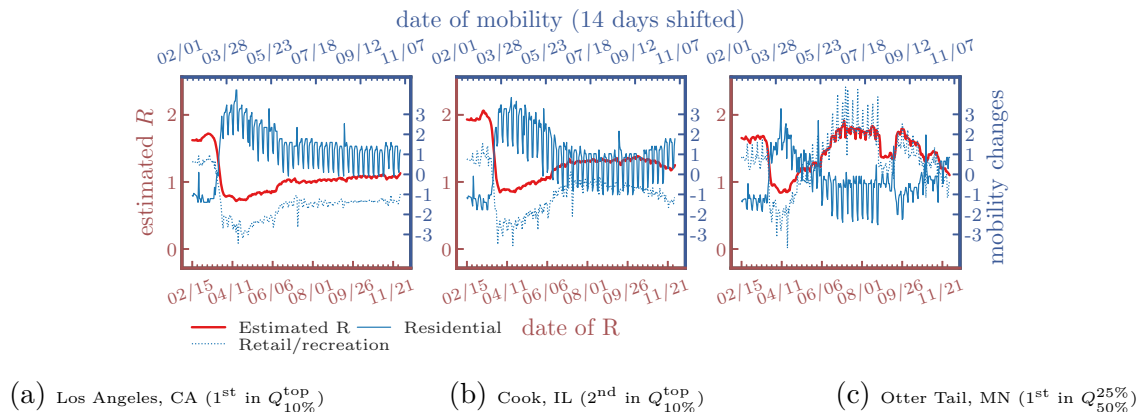


Figure 6.7. Estimated R of confirmed cases $\mathcal{D}_{\text{conf}}$ and lagged mobility changes ($\Delta = 14$ days)

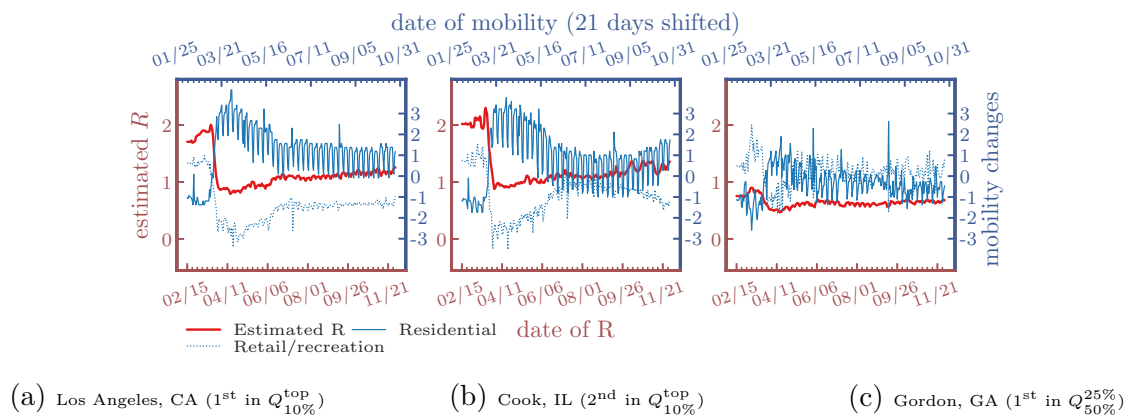


Figure 6.8. Estimated R of deaths $\mathcal{D}_{\text{death}}$ and lagged mobility changes ($\Delta = 21$ days)

In Figure 6.7 and Figure 6.8, we find that the estimated dynamic reproduction number closely tracks lagged mobility, where the optimal lag parameter is determined as $\Delta = 14$ days for $\mathcal{D}_{\text{conf}}$ and $\Delta = 21$ days for $\mathcal{D}_{\text{death}}$. The top-2 counties in $Q_{10\%}^{\text{top}}$ have estimated reproduction number initially above 2.5. After stay-at-home orders (around 04/11/2020), mobility in residential areas increased. On the other hand, mobility in retail and recreation decreased and the reproduction number fell to around 1, which explains why curves were relatively “flat” in many areas in the U.S. after the lockdown. However, as most of states re-opened and lifted up the restrictions, the reproduction number increased after a large population resumed their daily routine, which can be also be observed by the increased mobility in retail and recreation after July. Lastly, to validate the reproduction numbers, we

also compare our results to the ones estimated by Stanford University ⁶ and our estimation match to their findings, which are around 1.5-2.5 initially and 0.5-1.5 up to the beginning of December in 2020.

Example of Estimated Event Intensities and Weekly Forecasts

In Fig. 6.9, we present examples of the estimated intensities for the following four models: **Hawkes**, **HkPR_d**, **HkPR_m** and **HkPR_m⁺**, and we compare them with the number of cases/death in Cook, IL/Los Angeles, CA, respectively. Note that we add **HkPR_d**, a Hawkes model in which only demographics is used. In these models, **HkPR_m** and **HkPR_m⁺** include mobility indices to estimate the reproduction number dynamically, and **Hawkes** and **HkPR_d** have a constant reproduction number for each county. Comparing **Hawkes** and **HkPR_d**, the marginal variance between the intensities suggests that demographic features may not significantly affect modeling the reproduction number in the present data. On the other hand, **HkPR_m** and **HkPR_m⁺** show yield different fitted intensities compared to **Hawkes** and **HkPR_d**, indicating that mobility is playing an important role.

In Fig. 6.10, we present an example of weekly forecasts for all models except **PROJ**, which has relatively poor performance. In addition, we compare the forecasts against the true number of cases/deaths of Los Angeles, CA/Cook, IL respectively to provide a graphical presentation of the model fits. In general, all models can successfully capture the trend of the number of events, especially the valley around June and July and the spike in November, though the Hawkes process forecasts are more accurate than **CLEP** and **BUCKY**.

Dynamic Background Rate μ_c Modeling

In this section, we investigate a potential improvement to the model with the incorporation of a dynamic background rate $\mu_c(t)$. For this purpose we again use mobility as a covariate and estimate the background rate through Poisson regression, where $\mu_c(t) = \exp(\theta_\mu^\top \mathbf{x}_c^{t-\Delta})$. The reasoning behind this choice is that imported case volume is correlated with mobility, especially in transit stations. Estimation for the corresponding parameter, θ_μ , is achieved

⁶<https://web.stanford.edu/~chadj/Covid/Dashboard.html>

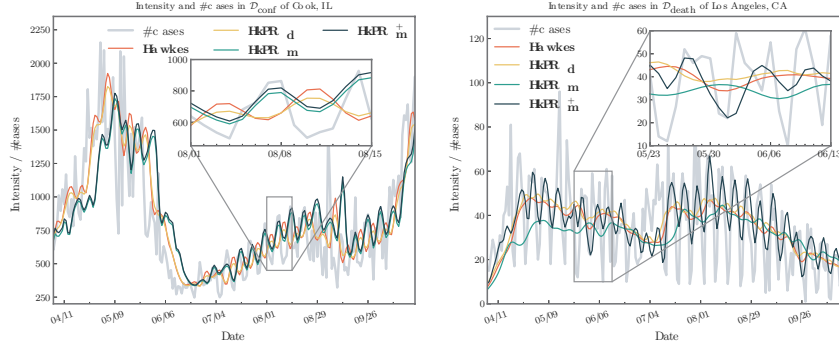


Figure 6.9. Example of the fitted effect from mobility and demographics

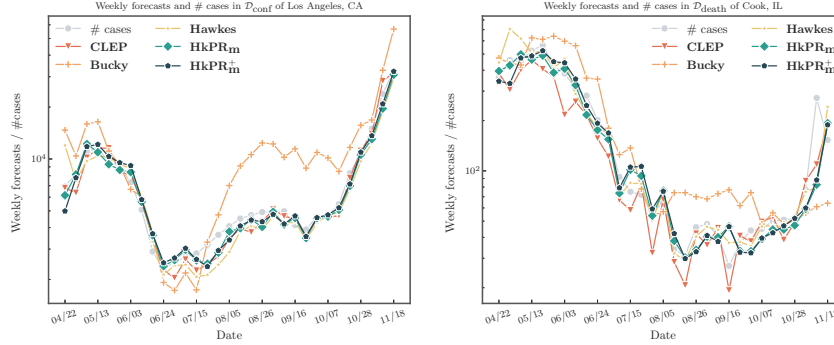


Figure 6.10. Example of the weekly forecasts

through maximum likelihood estimation (MLE) corresponding to Poisson regression in the M-step of the EM algorithm. This new approach can be seen as a variation of our model that we denote as \mathbf{HkPR}_μ . We apply this variation of our $\mathbf{SOS} - \mathbf{EW}$ on the dataset from The New York Times (NYT) and we explore the improvements in the forecasting task for 7 and 14 days.

In Table 6.9, we summarize the performance of the Hawkes model with dynamic background rate, where indicate improvements over the best model from the previous experiments in bold.

In Table 6.9, we can see some marginal improvements over the previous best models, especially for confirmed cases. Further improvements may be possible by monitoring cross-county and cross-state travel patterns, which would be a good direction for future investigation.

Table 6.9. Performance and improvements of \mathbf{HkPR}_μ on $\mathcal{D}_{\text{conf}}$ and $\mathcal{D}_{\text{death}}$

data	evl	7-days				14-days			
		$Q_{10\%}^{\text{top}}$		$Q_{25\%}^{\text{top}}$		$Q_{10\%}^{\text{top}}$		$Q_{25\%}^{\text{top}}$	
$\mathcal{D}_{\text{conf}}$	MAE	206.66	(1.93%)	113.95	(0.34%)	509.88	(1.76%)	271.20	(0.24%)
	PE	11.57	-	10.44	-	14.44	-	15.44	-
	NDCG	0.9761	(0.24%)	0.9768	(0.09%)	0.9735	-	0.9739	-
$\mathcal{D}_{\text{death}}$	MAE	7.12	(0.98%)	4.03	(0.98%)	13.67	-	7.69	-
	PE	18.07	-	16.87	-	16.39	-	16.61	-
	NDCG	0.9492	-	0.9475	-	0.9515	(0.14%)	0.9520	(0.06%)

The performances which have an improvement over the best model from the previous experiments are marked in **bold** and the improvement (%) over the best models from previous performance is included. In this table, “evl” is the evaluation metrics and “dataset” is the set of COVID reports on which we apply the model.

6.2.4 State-level Comparison to COVID-19 Forecast Hub

The COVID-19 Forecast Hub ⁷ is a repository that aggregates COVID-19 forecasts from a number of university and research groups following standardized data and forecasting formats. In specific, such ensemble was created by taking the arithmetic average of each prediction quantile for all eligible models for a given location. Recently, the COVID-19 Forecast Hub [138] has also introduced an ensemble model that combines the various models submitted to the hub into a single ensemble forecast. Comparing to other standalone models, it has demonstrated superior performance in forecasting deaths due to COVID-19 after May 2020 in the 50 states. To better validate the our Hawkes process framework, in this section we compare our model with several individual submissions and the ensemble model from the COVID-19 Forecast Hub.

Several differences between our county level experiments in the previous sections and the format of COVID-19 Forecast Hub submissions are worth noting. In particular, COVID-19 Forecast Hub forecasts are at the state level and some team contributions vary significantly in terms of the number of submissions, which locations are included, and whether cases and/or deaths are forecasted. In addition to the differences between the source of COVID-19 reports ⁸, we also note that only a few teams have complete submissions at each county. Therefore,

⁷<https://covid19forecasthub.org/>

⁸[↑] COVID-19 Forecast Hub has used reports from Johns Hopkins University and we use reports from the New York Times in our previous application

to fairly compare and contribute to the ensemble model, we adapt our framework by training our models at the state-level using reports from the Johns Hopkins University dataset, from 02/15/2020 to 03/21/2021. Also, we incorporate Google mobility index for each state ⁹ and with state-wise demographics ¹⁰ to model the event intensities, reproduction number, and the background rate in Equation 1.

Weighted Interval Score WIS

The COVID-19 Forecast Hub uses a quantile based metric to evaluate forecasts, the weighted interval score (WIS), which considers the uncertainty in the predictive distribution [139]. Given a predictive distribution F in the format of quantiles, WIS can be seen as a measure of closeness between the entire distribution and the ground truth. To evaluate with WIS, we first calculate a single interval score IS_α .

$$IS_\alpha(F, \hat{n}_c) = (u - l) + \frac{2}{\alpha}(l - \hat{n}_c) \cdot 1(\hat{n}_c < l) + \frac{2}{\alpha}(\hat{n}_c - u) \cdot 1(\hat{n}_c > u), \quad (6.23)$$

where $1(\cdot)$ is the indicator function, l and u are the values at $\frac{2}{\alpha}$ and $1 - \frac{2}{\alpha}$ quantiles. We then calculate the weighted sum of interval scores by summarizing accuracy across the entire predictive distribution. The overall WIS is defined as a linear combination of K interval scores:

$$WIS_{\alpha, \mathbf{K}}(F, \hat{n}_c) = \frac{1}{K + 0.5} \left\{ w_0 \cdot |n_c - \hat{n}_c| + \sum_{k=1}^K w_k \cdot IS_{\alpha_k}(F, \hat{n}_c) \right\}, \quad (6.24)$$

where $w_k = \frac{\alpha_k}{2}, k = 1, \dots, K$ and $w_0 = \frac{1}{2}$. In this manuscript, we use $K = 11$ and $\alpha = 0.02, 0.05, 0.1, 0.2, \dots, 0.9$ as in [139].

Selection Criteria and Comparison Results

We first select the models which have passed the screening process in the COVID-19 Forecast Hub [140] based on the following criteria: (1) inclusion of forecasts for at least 25 states

⁹<https://www.google.com/covid19/mobility/>

¹⁰<https://www.census.gov/>

for deaths; (2) a complete set of quantiles; and (3) at least 19 eligible weeks. We further retain 9 models that have a better **WIS** score than the baseline proposed by the COVID-19 Forecast Hub [140]. The forecasting evaluation starts with the week of 05/04/2020 - 05/10/2020 and then moves forward weekly until 03/15/2021 - 03/21/2021. In each weekly submission, each team makes forecasts for 1 to 4 weeks ahead. One challenge is that each model has a different number of states and forecasting weeks in the submission. Therefore, following a similar fashion in [140], we calculate the relative evaluation metric for a fair comparison.

For each state-week combination, we first divide \mathbf{HkPR}_m^+ 's **WIS** and **MAE** by each models' evaluation results, respectively. We then report the geometric mean of relative scores from all state-week combinations in Table 6.10. Note that all hyper-parameters are selected based on the best performance from the previous week for each state-week combination. Therefore, if the value is less than 1, we can suggest that there is an improvement in terms of the error measurement on average.

In terms of confirmed cases (denoted as $\mathcal{D}_{\text{conf}}^{\text{JHU}}$), \mathbf{HkPR}_m^+ has consistently outperformed the selected models in **MAE** and **WIS** except for the COVIDhub-ensemble in the 4th weeks window ahead. Overall, besides \mathbf{HkPR}_m^+ , COVIDhub-ensemble has the most competitive results. COVIDhub-baseline and COVIDhub-ensemble model are designed by the COVID-19 Forecasts Hub [140]. Here, COVIDhub-baseline serves as a reference point and is generated by the median number of cases from the most recent week, and COVIDhub-ensemble aggregates all the submissions to generate an ensemble forecast.

For the COVID-19 Forecast Hub to generate an accurate ensemble, diverse modeling perspectives can be beneficial. The promising results in $\mathcal{D}_{\text{conf}}^{\text{JHU}}$ indicate that forecasts for confirmed cases can benefit from modeling with a Hawkes process that incorporates dynamic covariates. Given that many forecasting groups are using compartmental models, we believe that \mathbf{HkPR}_m^+ can potentially enhance the forecasting accuracy of ensemble forecasts through both its accuracy and diversity. Note that all the weekly forecasts were updated in the anonymous repository¹¹.

¹¹<https://anonymous.4open.science/r/d425dcf9-3cfb-4f82-a08c-ee583ab36291/>

Table 6.10. Relative WIS and MAE on the JHU dataset

Model	$\mathcal{D}_{\text{conf}}^{\text{JHU}}$							
	Relative WIS				Relative MAE			
	1 wk	2 wk	3 wk	4 wk	1 wk	2 wk	3 wk	4 wk
HkPR_m⁺	1.00	1.00	1.00	1.00	1.00	1.00	1.00	1.00
Covid19Sim-Simulator	0.51	0.53	0.60	0.69	0.72	0.70	0.79	0.88
COVIDhub-baseline	0.80	0.74	0.78	0.87	0.91	0.80	0.84	0.91
Karlen-pypm	0.68	0.70	0.73	0.77	0.77	0.73	0.74	0.78
COVIDhub-ensemble	0.94	0.90	0.94	1.01	0.99	0.89	0.94	1.01

Model	$\mathcal{D}_{\text{death}}^{\text{JHU}}$							
	Relative WIS				Relative MAE			
	1 wk	2 wk	3 wk	4 wk	1 wk	2 wk	3 wk	4 wk
HkPR_m⁺	1	1	1	1	1	1	1	1
Covid19Sim-Simulator	0.77	0.89	1.05	1.39	0.88	1.07	1.22	1.61
MOBS-GLEAM.COVID	0.81	0.87	0.97	1.25	0.88	0.99	1.08	1.32
UA-EpiCovDA	0.85	0.83	0.92	1.15	1.19	1.17	1.15	1.49
COVIDhub-baseline	0.86	0.8	0.87	1.11	1.36	1.36	1.35	1.67
GT-DeepCOVID	0.9	0.95	1.01	1.21	0.92	1	1.05	1.18
IHME-CurveFit	0.94	0.92	1.12	1.64	0.95	0.99	1.12	1.64
CMU-TimeSeries	0.96	0.97	1.01	1.08	1.21	1.23	1.39	1.44
YYG-ParamSearch	0.96	1.03	1.19	1.72	1.07	1.24	1.29	1.89
COVIDhub-ensemble	1.05	1.08	1.2	1.52	1.5	1.42	1.56	1.94

The best performance is marked in **bold** and the performances that **HkPR_m⁺** has outperformed are marked in **red**. In this table, “N wk” represents the forecasting for N weeks ahead, and “ $\mathcal{D}_{\text{conf}}^{\text{JHU}}$ ” and “ $\mathcal{D}_{\text{death}}^{\text{JHU}}$ ” are the confirmed cases and deaths collected by Johns Hopkins University, respectively. All the metadata information for the competing models can be found in the following url: <https://github.com/reichlab/covid19-forecast-hub/tree/master/data-processed>.

We note that, in the retrospective evaluation, our model may be slightly favored. Data available when prospective forecasting models were created may have been subject to reporting lags or have been updated at a later date. To completely reconstruct such data is a non-trivial task, therefore we acknowledge this as a limitation of the present work.

6.3 Conclusion

We showed how Hawkes processes can be combined with spatio-temporal covariates to accurately model COVID-19 transmission and forecast future cases and deaths. The model is competitive with several models used to forecast the pandemic, achieving improved MAE and NDCG scores on a majority of the experiments we conducted. Our hope is that this work will encourage more research into Hawkes process models of disease spreading that incorporate

more advanced features and statistical learning principles. As vaccinations are rolled out across the U.S. (given recent FDA approval), local impacts on dynamic reproduction can be flexibly accommodated by our model and used to obtain more accurate and timely forecasts.

One potential direction for future research is investigating the combination of Hawkes process forecasts with compartmental models for improved ensembles. Our results using data from the COVID-19 Forecast Hub indicate this could be a promising direction. Another potential direction for future research is extending the work here to neural network based point process models [44], [45]. These models may be able to capture more complicated relationships between mobility patterns, demographics, and transmission. The challenges of such an approach include the potential for over-fitting with added parameters and determining how best to realistically model transmission in a neural point process (analogous to the SIR-Hawkes process), which will be important if neural point processes are to be used in long-term forecasting.

7. SUMMARY

The self-exciting modeling is a powerful tool to infer the dynamic properties of events occurring in real life. In specific, Hawkes processes can help us to capture the infectivity among the events even more, making forecasting for the future.

In Chapter 3, we introduce a system for early detection of opioids which can be used to tackle the increasing crisis of opioid addictions and overdoses across the U.S. and internationally over the past decade. We first use drug SMILES, one hot encoded molecular substructures, to generate a bag of drug vectors corresponding to each overdose (overdoses are often characterized by multiple drugs taken at the same time). We then use spectral clustering to generate overdose categories and estimate multivariate Hawkes processes for the space-time intensity of overdoses following an initial event. As the productivity parameter of the process depends on the overdose category, this allows us to estimate the magnitude of an overdose spike based on the substances present (e.g., fentanyl leads to more subsequent overdoses compared to Oxycontin). We validate the model using opioid overdose deaths in Indianapolis and show that the model outperforms several recently introduced Hawkes-Topic models based on Dirichlet processes. We also point out that our system could be used in combination with drug test strips to alert drug-using populations of risky batches on the market or to more efficiently allocate naloxone to users and health/social workers.

In Chapter 4, we combine the derivation of the expected number of events for Hawkes processes and the UCB-normal algorithm to build a framework for the non-stochastic multi-armed bandit problem. Given the nature of self-exciting properties, the reward distribution is dynamic and time-varying. By introducing the Hawkes Processes modeling into the decision-making, we build upper confidence bound based on the expected number of events in the future. Several datasets, including crime activities and earthquakes, are used to validate the robustness of the proposed framework. Our model consistently outperforms the baseline methods that are designed to tackle the non-stochastic multi-armed bandit problem. This indicates that modeling temporal information based on their clustering patterns in time is very helpful for retrieving the events of interest within limited resources.

In Chapter 5, we propose a novel framework for integrating Hawkes processes with multi-armed bandit algorithms to solve spatio-temporal event forecasting and detection problems when data may be undersampled or spatially biased. In particular, we introduce an upper confidence bound algorithm using Bayesian spatial Hawkes process estimation for balancing the trade-off between exploiting geographic regions where data has been collected and exploring geographic regions where data is unobserved. We first validate our model using simulated data. We then apply it to the problem of disaster search and rescue using calls for service data from hurricane Harvey in 2017 and the problem of detection and clearance of improvised explosive devices (IEDs) using IED attack records in Iraq. Our model outperforms state-of-the-art baseline spatial MAB algorithms in terms of cumulative reward and several other ranking evaluation metrics.

In Chapter 6, We show that Hawkes processes that are used in statistical modeling for event clustering and causal inference can be viewed as stochastic versions of popular compartmental models used in epidemiology. In our work, we show how to develop accurate models of COVID-19 transmission using Hawkes processes with spatial-temporal covariates. We model the conditional intensity of new COVID-19 cases and deaths in the U.S. at the county level, estimating the dynamic reproduction number of the virus within an EM algorithm through a regression on Google mobility indices and demographic covariates in the maximization step. We validate the approach on both short-term and long-term forecasting tasks, showing that the Hawkes process outperforms several benchmark models currently used to track the pandemic, including an ensemble approach and an SEIR-variant. We also investigate which covariates and mobility indices are most important for building forecasts of COVID-19 in the U.S.

There are many directions to extend our methods. For example, multivariate Hawkes processes can be a good extension of our current framework for COVID-19 and earthquake datasets. A more general regularization method can be used to smooth out the triggering kernel to avoid over-fitting. This allows us to apply our methods to the datasets with aggregated timestamps where a lot of temporal information is lost. Potential side information related to the events should also be included in our application. In specific, we have only drug structures for overdose events. However, demographic information may play an important

part. Regarding the COVID-19 modeling, besides the mobility, the vaccination rate can also be incorporated to model its counter effects on the reproduction number. It will be interesting to see how our approaches can be extended to other applications.

To summarize the work presented in this thesis, we list the main contribution of each project and how its implications for future research benefit from our study.

- **SOS – EW** (Chapter 3): We proposed a framework that leverages the drug chemical structures to make predictions on overdose spikes. This is done by categorizing the overdose events based on the substances found in the victim’s body. We then use Hawkes processes to model the overdose events and make predictions.

Implications for future research

In predictive policing [10] or social service delivery and intervention programming, it can benefit from our model to provide more efficient and immediate help. The public service can also leverage the model to analyze the overdose patterns and offer better deployment of syringe services [141].

- **HpUCB** (Chapter 4): We integrate a multi-armed bandit algorithm with the Hawkes processes model to develop an online learning framework for research rescue. The property of the Hawkes process for each region is learned during the exploration and exploitation. A novel optimistic upper confidence bound for the future number of events is constructed for decision making. The reward performance shows that the model can collect the most events during the search.

Implications for future research

Our model provides a great algorithm to model human planning in a life-like search-and-rescue mission [142]. Online learning poses an important role in routing and scheduling of search-and-rescue teams [143]. By formulating such an online learning process in the form of a multi-armed bandit problem, our model can generate the optimal decisions that consider the self-exciting properties of natural disaster events. Moreover, many research works have been proposed to investigate how social media can be used to predict criminal activities [144]. Especially, the Hawkes process has

been adopted to investigate the influence of pathogenic social media posts [145]. We believe our model can enrich this line of work and provide a more robust framework.

- **HpSpUCB** (Chapter 5): On top of HpUCB, we introduce a new strategy to include spatial information. Another innovation is how we use Hawkes process simulation to fill up the gap between observations. Basically, we build upper temporal confidence bound and incorporate it with spatial UCB. Experiments show its advantage over the other baseline when we apply it to the temporally and spatially clustered events.

Implications for future research While most multi-armed bandit algorithms consider that each reward observation is independent of the other, our model provides an insight to bridge the gap between the observations. A few research paper has tried to tackle the problem in this domain. They either use the side information to create a standard learning problem without missing observations [146] or leverage the context with observation to make inference [147]. I believe this work can be a pilot study for filling the observation gaps in the MAB setting.

- **HawkPR** (Chapter 6):

In this project, an effective and robust Hawkes process model has been proposed to make forecasting for future COVID cases. A mobility index is seamlessly integrated into the modeling for infectivity as long as the spatial information in the form of demographic dataset.

Implications for future research

We contributed our work to the COVID-19 Forecast Hub ¹ as we believe our work can be included in the ensemble model and increase the precision of the overall forecast. Our project also aspired some research work that models the COVID cases on a very a fine-scale by leveraging a high-resolution spatio-temporal model [148]. As one of the pilot studies that use the Hawkes process to model COVID-19 progression, our project can certainly serve as a strong baseline model for many similar approaches [149], and [150]. We also shed some light on the research community on how mobility

¹<https://covid19forecasthub.org/>

affects infectivity as one of the pioneers that model the cases with human activity [151]. Many follow-up research has showed the promising results by using similar mobility datasets [152].

In conclusion, our models are designed to facilitate the policymakers to make a decision. Model **SOS – EW** (Chapter 4) proposed an algorithm to predict the overdose spike. Policymakers can use the model to dynamically arrange the resources, such as drug disposal facilities, naloxone and naloxone training, or public health and harm reduction programs more efficiently. The distribution of syringe services can also be done more ideally to prevent waste. The enforcers can also use our model to deploy the beat based on the spike patterns. Models **HpSpUCB** (Chapter 5) and **HpUCB** (Chapter 4) have provide an online learning strategy for natural disaster rescue. For example, during the strikes of Hurricanes, the coast guard can leverage our system to send out their teams and explore the blind spots in the city with better chances to rescue people. In the most earth-quake-prone area, the United States Geological Survey (USGS) and USAID Earthquake Disaster Assistance Team (EDAT) can monitor and support places identified with seismic hazards as they take the preventative procedures to mitigate these hazards. Model **HawkPR** (Chapter 6) is a powerful tool to indicate the COVID outbreaks in the near future at a county level. With the aid of our model, the policymakers can identify the hot spot to limit the public gatherings or pose mask mandates. Mover over, the policymakers can also evaluate the necessity of traveling restrictions for high-risk regions that our model identifies.

REFERENCES

- [1] G. Mohler, J. Carter, and R. Raje, “Improving social harm indices with a modulated hawkes process,” *International Journal of Forecasting*, vol. 34, no. 3, pp. 431–439, 2018.
- [2] K.-L. Tsui, S. Y. Wong, W. Jiang, and C.-J. Lin, “Recent research and developments in temporal and spatiotemporal surveillance for public health,” *IEEE Transactions on Reliability*, vol. 60, no. 1, pp. 49–58, 2011.
- [3] H.-L. Yu, A. Kolovos, G. Christakos, J.-C. Chen, S. Warmerdam, and B. Dev, “Interactive spatiotemporal modelling of health systems: The seks-gui framework,” *Stochastic Environmental Research and Risk Assessment*, vol. 21, no. 5, pp. 555–572, 2007.
- [4] D. Weisburd, “The law of crime concentration and the criminology of place,” *Criminology*, vol. 53, no. 2, pp. 133–157, 2015.
- [5] J. Hibdon and E. R. Groff, “What you find depends on where you look: Using emergency medical services call data to target illicit drug use hot spots,” *Journal of contemporary criminal justice*, vol. 30, no. 2, pp. 169–185, 2014.
- [6] J. Hibdon, C. W. Telep, and E. R. Groff, “The concentration and stability of drug activity in seattle, washington using police and emergency medical services data,” *Journal of quantitative criminology*, vol. 33, no. 3, pp. 497–517, 2017.
- [7] J. G. Carter, G. Mohler, and B. Ray, “Spatial concentration of opioid overdose deaths in indianapolis: An application of the law of crime concentration at place to a public health epidemic,” *Journal of Contemporary Criminal Justice*, p. 1 043 986 218 803 527, 2018.
- [8] M. Townsley, R. Homel, and J. Chaseling, “Infectious burglaries. a test of the near repeat hypothesis,” *British Journal of Criminology*, vol. 43, no. 3, pp. 615–633, 2003.
- [9] A. M. Zeoli, J. M. Pizarro, S. C. Grady, and C. Melde, “Homicide as infectious disease: Using public health methods to investigate the diffusion of homicide,” *Justice quarterly*, vol. 31, no. 3, pp. 609–632, 2014.
- [10] G. O. Mohler, M. B. Short, S. Malinowski, M. Johnson, G. E. Tita, A. L. Bertozzi, and P. J. Brantingham, “Randomized controlled field trials of predictive policing,” *Journal of the American statistical association*, vol. 110, no. 512, pp. 1399–1411, 2015.
- [11] P. Seth, L. Scholl, R. A. Rudd, and S. Bacon, “Overdose deaths involving opioids, cocaine, and psychostimulants—united states, 2015–2016,” *Morbidity and Mortality Weekly Report*, vol. 67, no. 12, p. 349, 2018.

- [12] D. Ciccarone, “Fentanyl in the us heroin supply: A rapidly changing risk environment,” *International Journal of Drug Policy*, vol. 46, pp. 107–111, 2017.
- [13] T. J. Cicero, M. S. Ellis, H. L. Surratt, and S. P. Kurtz, “The changing face of heroin use in the united states: A retrospective analysis of the past 50 years,” *JAMA psychiatry*, vol. 71, no. 7, pp. 821–826, 2014.
- [14] R. A. Rudd, L. J. Paulozzi, M. J. Bauer, R. W. Burleson, R. E. Carlson, D. Dao, J. W. Davis, J. Dudek, B. A. Eichler, J. C. Fernandes, *et al.*, “Increases in heroin overdose deaths—28 states, 2010 to 2012,” *MMWR. Morbidity and mortality weekly report*, vol. 63, no. 39, p. 849, 2014.
- [15] G. K. Strickler, K. Zhang, J. M. Halpin, A. S. Bohnert, G. Baldwin, and P. W. Kreiner, “Effects of mandatory prescription drug monitoring program (pdmp) use laws on prescriber registration and use and on risky prescribing,” *Drug and Alcohol Dependence*, 2019.
- [16] R. M. Gladden, “Fentanyl law enforcement submissions and increases in synthetic opioid-involved overdose deaths—27 states, 2013–2014,” *MMWR. Morbidity and mortality weekly report*, vol. 65, 2016.
- [17] C. M. Jones, E. B. Einstein, and W. M. Compton, “Changes in synthetic opioid involvement in drug overdose deaths in the united states, 2010–2016,” *Jama*, vol. 319, no. 17, pp. 1819–1821, 2018.
- [18] D. B. Kandel, M.-C. Hu, P. Griesler, and M. Wall, “Increases from 2002 to 2015 in prescription opioid overdose deaths in combination with other substances,” *Drug and alcohol dependence*, vol. 178, pp. 501–511, 2017.
- [19] C. McCall Jones, G. T. Baldwin, and W. M. Compton, “Recent increases in cocaine-related overdose deaths and the role of opioids,” *American journal of public health*, vol. 107, no. 3, pp. 430–432, 2017.
- [20] W. Fernandez, H. Hackman, L. Mckeown, T. Anderson, and B. Hume, “Trends in opioid-related fatal overdoses in massachusetts, 1990–2003,” *Journal of substance abuse treatment*, vol. 31, no. 2, pp. 151–156, 2006.
- [21] J. M. Hoppe-Roberts, L. M. Lloyd, and P. A. Chyka, “Poisoning mortality in the united states: Comparison of national mortality statistics and poison control center reports,” *Annals of emergency medicine*, vol. 35, no. 5, pp. 440–448, 2000.
- [22] J. G. Linakis and K. A. Frederick, “Poisoning deaths not reported to the regional poison control center,” *Annals of emergency medicine*, vol. 22, no. 12, pp. 1822–1828, 1993.

- [23] D. K. Wysowski, “Surveillance of prescription drug-related mortality using death certificate data,” *Drug Safety*, vol. 30, no. 6, pp. 533–540, 2007.
- [24] C. J. Ruhm, “Corrected us opioid-involved drug poisoning deaths and mortality rates, 1999–2015,” *Addiction*, vol. 113, no. 7, pp. 1339–1344, 2018.
- [25] M. Warner and H. Hedegaard, *Identifying opioid overdose deaths using vital statistics data*, 2018.
- [26] T. P. Gilson, “The medical examiner’s role in addressing the opioid crisis,” *US Att’ys Bull.*, vol. 66, p. 47, 2018.
- [27] D. Chakrabarti, R. Kumar, F. Radlinski, and E. Upfal, “Mortal multi-armed bandits,” in *Advances in neural information processing systems*, 2009, pp. 273–280.
- [28] L. Zhou and E. Brunskill, “Latent contextual bandits and their application to personalized recommendations for new users,” *arXiv preprint arXiv:1604.06743*, 2016.
- [29] L. Qin, S. Chen, and X. Zhu, “Contextual combinatorial bandit and its application on diversified online recommendation,” in *Proceedings of the 2014 SIAM International Conference on Data Mining*, SIAM, 2014, pp. 461–469.
- [30] A. Durand, C. Achilleos, D. Iacovides, K. Strati, G. D. Mitsis, and J. Pineau, “Contextual bandits for adapting treatment in a mouse model of de novo carcinogenesis,” in *Machine Learning for Healthcare Conference*, 2018, pp. 67–82.
- [31] W. R. Smith, K. K. Stephens, B. Robertson, J. Li, and D. Murthy, “Social media in citizen-led disaster response: Rescuer roles, coordination challenges, and untapped potential,” in *Proceedings of the... International ISCRAM Conference*, 2018.
- [32] S. Goswami, S. Chakraborty, S. Ghosh, A. Chakrabarti, and B. Chakraborty, “A review on application of data mining techniques to combat natural disasters,” *Ain Shams Engineering Journal*, vol. 9, no. 3, pp. 365–378, 2018.
- [33] B. Merz, H. Kreibich, and U. Lall, “Multi-variate flood damage assessment: A tree-based data-mining approach,” *Natural Hazards and Earth System Sciences (NHESS)*, vol. 13, no. 1, pp. 53–64, 2013.
- [34] M. S. Tehrany, B. Pradhan, and M. N. Jebur, “Spatial prediction of flood susceptible areas using rule based decision tree (dt) and a novel ensemble bivariate and multivariate statistical models in gis,” *Journal of Hydrology*, vol. 504, pp. 69–79, 2013.
- [35] F. Cheong and C. Cheong, “Social media data mining: A social network analysis of tweets during the 2010-2011 australian floods,” *PACIS*, vol. 11, pp. 46–46, 2011.

- [36] N. M. Ferguson, D. Laydon, G. Nedjati-Gilani, N. Imai, K. Ainslie, M. Baguelin, S. Bhatia, A. Boonyasiri, Z. Cucunubá, G. Cuomo-Dannenburg, *et al.*, “Impact of non-pharmaceutical interventions (npis) to reduce covid-19 mortality and healthcare demand. 2020,” *DOI*, vol. 10, p. 77482, 2020.
- [37] I. COVID, C. J. Murray, *et al.*, “Forecasting covid-19 impact on hospital bed-days, icu-days, ventilator-days and deaths by us state in the next 4 months,” *medRxiv*, 2020.
- [38] S. Pei and J. Shaman, “Initial simulation of sars-cov2 spread and intervention effects in the continental us,” *medRxiv*, 2020.
- [39] M. Smith, K. Yourish, S. Almukhtar, K. Collins, D. Ivory, A. McCann, *et al.*, “Coronavirus in the us: Latest map and case count,” *The New York Times*, 2020.
- [40] M. Kinsey, K. Tallaksen, O. R.F., L. Asher, C. Costello, M. Kelbaugh, and S. Wilson, *Bucky model: A spatial seir model for simulating covid-19 at the county level*. [Online]. Available: <https://buckymodel.com/>.
- [41] D. Zou, L. Wang, P. Xu, J. Chen, W. Zhang, and Q. Gu, “Epidemic model guided machine learning for covid-19 forecasts in the united states,” *medRxiv*, 2020.
- [42] M.-A. Rizoïu, S. Mishra, Q. Kong, M. Carman, and L. Xie, “Sir-hawkes: Linking epidemic models and hawkes processes to model diffusions in finite populations,” in *Proceedings of the 2018 World Wide Web Conference*, 2018, pp. 419–428.
- [43] K. Zhou, H. Zha, and L. Song, “Learning triggering kernels for multi-dimensional hawkes processes,” in *International Conference on Machine Learning*, 2013, pp. 1301–1309.
- [44] H. Mei and J. M. Eisner, “The neural hawkes process: A neurally self-modulating multivariate point process,” in *Advances in Neural Information Processing Systems*, 2017, pp. 6754–6764.
- [45] T. Omi, K. Aihara, *et al.*, “Fully neural network based model for general temporal point processes,” in *Advances in Neural Information Processing Systems*, 2019, pp. 2120–2129.
- [46] G. Mohler and M. D. Porter, “Rotational grid, pai-maximizing crime forecasts,” *Statistical Analysis and Data Mining: The ASA Data Science Journal*, vol. 11, no. 5, pp. 227–236, 2018.
- [47] H. Xu and H. Zha, “A dirichlet mixture model of hawkes processes for event sequence clustering,” in *Advances in Neural Information Processing Systems*, 2017, pp. 1354–1363.

- [48] N. Du, M. Farajtabar, A. Ahmed, A. J. Smola, and L. Song, “Dirichlet-hawkes processes with applications to clustering continuous-time document streams,” in *Proceedings of the 21th ACM SIGKDD International Conference on Knowledge Discovery and Data Mining*, 2015, pp. 219–228.
- [49] H. Xu, M. Farajtabar, and H. Zha, “Learning granger causality for hawkes processes,” in *International Conference on Machine Learning*, 2016, pp. 1717–1726.
- [50] U. Upadhyay, A. De, and M. G. Rodriguez, “Deep reinforcement learning of marked temporal point processes,” in *Advances in Neural Information Processing Systems*, 2018, pp. 3168–3178.
- [51] S. Li, S. Xiao, S. Zhu, N. Du, Y. Xie, and L. Song, “Learning temporal point processes via reinforcement learning,” in *Advances in neural information processing systems*, 2018, pp. 10 781–10 791.
- [52] A. Sancetta, “Estimation for the prediction of point processes with many covariates,” *Econometric Theory*, vol. 34, no. 3, pp. 598–627, 2018.
- [53] A. Reinhart and J. Greenhouse, “Self-exciting point processes with spatial covariates: Modelling the dynamics of crime,” *Journal of the Royal Statistical Society: Series C (Applied Statistics)*, vol. 67, no. 5, pp. 1305–1329, 2018.
- [54] P. Han, J. Zhuang, K. Hattori, C.-H. Chen, F. Febriani, H. Chen, C. Yoshino, and S. Yoshida, “Assessing the potential earthquake precursory information in ulf magnetic data recorded in kanto, japan during 2000–2010: Distance and magnitude dependences,” *Entropy*, vol. 22, no. 8, p. 859, 2020.
- [55] J. Zhuang, Y. Ogata, D. Vere-Jones, L. Ma, and H. Guan, “Statistical modeling of earthquake occurrences based on external geophysical observations: With an illustrative application to the ultra-low frequency ground electric signals observed in the beijing region,” in *Seismic Imaging, Fault Damage and Heal*, De Gruyter, 2014, pp. 351–378.
- [56] F. P. Schoenberg, “A note on the consistent estimation of spatial-temporal point process parameters,” *Statistica Sinica*, pp. 861–879, 2016.
- [57] J. Molyneux, J. Gordon, and F. Schoenberg, “Assessing the predictive accuracy of earthquake strike angle estimates using nonparametric hawkes processes,” *Environmetrics*, vol. 29, no. 2, e2491, 2018.
- [58] B. Mark, G. Raskutti, and R. Willett, “Network estimation from point process data,” *IEEE Transactions on Information Theory*, vol. 65, no. 5, pp. 2953–2975, 2018.

- [59] E. Lewis and G. Mohler, “A nonparametric em algorithm for multiscale hawkes processes,” *preprint*, 2011.
- [60] E. C. Hall and R. M. Willett, “Tracking dynamic point processes on networks,” *IEEE Transactions on Information Theory*, vol. 62, no. 7, pp. 4327–4346, 2016.
- [61] M. Tokic and G. Palm, “Value-difference based exploration: Adaptive control between epsilon-greedy and softmax,” in *Annual Conference on Artificial Intelligence*, Springer, 2011, pp. 335–346.
- [62] L. Tran-Thanh, A. Chapman, E. M. de Cote, A. Rogers, and N. R. Jennings, “Epsilon-first policies for budget-limited multi-armed bandits,” in *Twenty-Fourth AAAI Conference on Artificial Intelligence*, 2010.
- [63] A. Gopalan, S. Mannor, and Y. Mansour, “Thompson sampling for complex online problems,” in *International Conference on Machine Learning*, 2014, pp. 100–108.
- [64] D. Eckles and M. Kaptein, “Thompson sampling with the online bootstrap,” *arXiv preprint arXiv:1410.4009*, 2014.
- [65] N. Gupta, O.-C. Granmo, and A. Agrawala, “Thompson sampling for dynamic multi-armed bandits,” in *2011 10th International Conference on Machine Learning and Applications and Workshops*, IEEE, vol. 1, 2011, pp. 484–489.
- [66] V. Kuleshov and D. Precup, “Algorithms for multi-armed bandit problems,” *arXiv preprint arXiv:1402.6028*, 2014.
- [67] L. Li, W. Chu, J. Langford, and R. E. Schapire, “A contextual-bandit approach to personalized news article recommendation,” in *Proceedings of the 19th international conference on World wide web*, 2010, pp. 661–670.
- [68] W. Chu, L. Li, L. Reyzin, and R. Schapire, “Contextual bandits with linear payoff functions,” in *Proceedings of the Fourteenth International Conference on Artificial Intelligence and Statistics*, 2011, pp. 208–214.
- [69] A. Krause and C. S. Ong, “Contextual gaussian process bandit optimization,” in *Advances in neural information processing systems*, 2011, pp. 2447–2455.
- [70] C. M. Wu, E. Schulz, M. Speekenbrink, J. D. Nelson, and B. Meder, “Mapping the unknown: The spatially correlated multi-armed bandit,” *bioRxiv*, p. 106 286, 2017.

- [71] E. W. Fox, F. P. Schoenberg, J. S. Gordon, *et al.*, “Spatially inhomogeneous background rate estimators and uncertainty quantification for nonparametric hawkes point process models of earthquake occurrences,” *The Annals of Applied Statistics*, vol. 10, no. 3, pp. 1725–1756, 2016.
- [72] E. Bacry, I. Mastromatteo, and J.-F. Muzy, “Hawkes processes in finance,” *Market Microstructure and Liquidity*, vol. 1, no. 01, p. 1550005, 2015.
- [73] W.-H. Chiang, B. Yuan, H. Li, B. Wang, A. Bertozzi, J. Carter, B. Ray, and G. Mohler, “Sos-ew: System for overdose spike early warning using drug mover’s distance-based hawkes processes,” in *Joint European Conference on Machine Learning and Knowledge Discovery in Databases*, Springer, 2019, pp. 538–554.
- [74] G. O. Mohler, M. B. Short, P. J. Brantingham, F. P. Schoenberg, and G. E. Tita, “Self-exciting point process modeling of crime,” *Journal of the American Statistical Association*, vol. 106, no. 493, pp. 100–108, 2011.
- [75] E. M. Lowder, B. R. Ray, P. Huynh, A. Ballew, and D. P. Watson, “Identifying unreported opioid deaths through toxicology data and vital records linkage: Case study in marion county, indiana, 2011–2016,” *American journal of public health*, vol. 108, no. 12, pp. 1682–1687, 2018.
- [76] P. Phalen, B. Ray, D. P. Watson, P. Huynh, and M. S. Greene, “Fentanyl related overdose in indianapolis: Estimating trends using multilevel bayesian models,” *Addictive behaviors*, vol. 86, pp. 4–10, 2018.
- [77] B. Ray, K. Quinet, T. Dickinson, D. P. Watson, and A. Ballew, “Examining fatal opioid overdoses in marion county, indiana,” *Journal of urban health*, vol. 94, no. 2, pp. 301–310, 2017.
- [78] M. Hirohara, Y. Saito, Y. Koda, K. Sato, and Y. Sakakibara, “Convolutional neural network based on smiles representation of compounds for detecting chemical motif,” *BMC bioinformatics*, vol. 19, no. 19, p. 526, 2018.
- [79] A. Y. Ng, M. I. Jordan, and Y. Weiss, “On spectral clustering: Analysis and an algorithm,” in *Advances in neural information processing systems*, 2002, pp. 849–856.
- [80] Y. Rubner, C. Tomasi, and L. J. Guibas, “The earth mover’s distance as a metric for image retrieval,” *International journal of computer vision*, vol. 40, no. 2, pp. 99–121, 2000.
- [81] G. O. Mohler, M. B. Short, P. J. Brantingham, F. P. Schoenberg, and G. E. Tita, “Self-exciting point process modeling of crime,” *Journal of the American Statistical Association*, vol. 106, no. 493, pp. 100–108, 2011.

- [82] S. Flaxman, M. Chirico, P. Pereira, and C. Loeffler, “Scalable high-resolution forecasting of sparse spatiotemporal events with kernel methods: A winning solution to the nij” real-time crime forecasting challenge,” *arXiv preprint arXiv:1801.02858*, 2018.
- [83] S. Shirota, A. E. Gelfand, *et al.*, “Space and circular time log gaussian cox processes with application to crime event data,” *The Annals of Applied Statistics*, vol. 11, no. 2, pp. 481–503, 2017.
- [84] C. Li, Z. Song, and X. Wang, “Nonparametric method for modeling clustering phenomena in emergency calls under spatial-temporal self-exciting point processes,” *IEEE Access*, vol. 7, pp. 24 865–24 876, 2019, ISSN: 2169-3536. DOI: [10.1109/ACCESS.2019.2900340](https://doi.org/10.1109/ACCESS.2019.2900340).
- [85] A. Zammit-Mangion, M. Dewar, V. Kadirkamanathan, and G. Sanguinetti, “Point process modelling of the afghan war diary,” *Proceedings of the National Academy of Sciences*, vol. 109, no. 31, pp. 12 414–12 419, 2012.
- [86] P. Gao, D. Guo, K. Liao, J. J. Webb, and S. L. Cutter, “Early detection of terrorism outbreaks using prospective space–time scan statistics,” *The Professional Geographer*, vol. 65, no. 4, pp. 676–691, 2013.
- [87] E. L. Lai, D. Moyer, B. Yuan, E. Fox, B. Hunter, A. L. Bertozzi, and P. J. Brantingham, “Topic time series analysis of microblogs,” *IMA Journal of Applied Mathematics*, vol. 81, no. 3, pp. 409–431, 2016.
- [88] N. Du, M. Farajtabar, A. Ahmed, A. J. Smola, and L. Song, “Dirichlet-hawkes processes with applications to clustering continuous-time document streams,” in *Proceedings of the 21th ACM SIGKDD International Conference on Knowledge Discovery and Data Mining*, ACM, 2015, pp. 219–228.
- [89] M. Farajtabar, Y. Wang, M. G. Rodriguez, S. Li, H. Zha, and L. Song, “Coevolve: A joint point process model for information diffusion and network co-evolution,” in *Advances in Neural Information Processing Systems*, 2015, pp. 1954–1962.
- [90] M. Kusner, Y. Sun, N. Kolkin, and K. Weinberger, “From word embeddings to document distances,” in *International Conference on Machine Learning*, 2015, pp. 957–966.
- [91] M. Levandowsky and D. Winter, “Distance between sets,” *Nature*, vol. 234, no. 5323, p. 34, 1971.
- [92] G. J. Lieberman and F. Hillier, *Introduction to mathematical programming*. McGraw-Hill, 1995.

- [93] U. Von Luxburg, “A tutorial on spectral clustering,” *Statistics and computing*, vol. 17, no. 4, pp. 395–416, 2007.
- [94] B. Yuan, H. Li, A. L. Bertozzi, P. J. Brantingham, and M. A. Porter, “Multivariate spatiotemporal hawkes processes and network reconstruction,” *arXiv preprint arXiv:1811.06321*, 2018.
- [95] G. Mohler, “Marked point process hotspot maps for homicide and gun crime prediction in chicago,” *International Journal of Forecasting*, vol. 30, no. 3, pp. 491–497, 2014.
- [96] J. Zhuang, Y. Ogata, and D. Vere-Jones, “Analyzing earthquake clustering features by using stochastic reconstruction,” *Journal of Geophysical Research: Solid Earth*, vol. 109, no. B5, 2004.
- [97] Y. Ogata, “On lewis’ simulation method for point processes,” *IEEE Transactions on Information Theory*, vol. 27, no. 1, pp. 23–31, 1981.
- [98] S. Kim, P. A. Thiessen, E. E. Bolton, J. Chen, G. Fu, A. Gindulyte, L. Han, J. He, S. He, B. A. Shoemaker, *et al.*, “Pubchem substance and compound databases,” *Nucleic acids research*, vol. 44, no. D1, pp. D1202–D1213, 2015.
- [99] G. Landrum, *Rdkit: Open-source cheminformatics software*, 2016.
- [100] S. Peker and A. Kocyigit, “Mrhr: A modified reciprocal hit rank metric for ranking evaluation of multiple preferences in top-n recommender systems,” in *International Conference on Artificial Intelligence: Methodology, Systems, and Applications*, Springer, 2016, pp. 320–329.
- [101] J. L. Glick, T. Christensen, J. N. Park, M. McKenzie, T. C. Green, and S. G. Sherman, “Stakeholder perspectives on implementing fentanyl drug checking: Results from a multi-site study,” *Drug and alcohol dependence*, vol. 194, pp. 527–532, 2019.
- [102] M. Karamouzian, C. Dohoo, S. Forsting, R. McNeil, T. Kerr, and M. Lysyshyn, “Evaluation of a fentanyl drug checking service for clients of a supervised injection facility, vancouver, canada,” *Harm reduction journal*, vol. 15, no. 1, p. 46, 2018.
- [103] M. C. Frost, E. C. Williams, S. Kingston, and C. J. Banta-Green, “Interest in getting help to reduce or stop substance use among syringe exchange clients who use opioids,” *Journal of addiction medicine*, vol. 12, no. 6, pp. 428–434, 2018.
- [104] R. Fisher, D. O’Donnell, B. Ray, and D. Rusyniak, “Police officers can safely and effectively administer intranasal naloxone,” *Prehospital Emergency Care*, vol. 20, no. 6, pp. 675–680, 2016.

- [105] B. R. Ray, E. M. Lowder, A. J. Kivisto, P. Phalen, and H. Gil, “Ems naloxone administration as non-fatal opioid overdose surveillance: 6-year outcomes in marion county, indiana,” *Addiction*, vol. 113, no. 12, pp. 2271–2279, 2018.
- [106] L. Cui, A. Hawkes, and H. Yi, “An elementary derivation of moments of hawkes processes,” *Advances in Applied Probability*, vol. 52, no. 1, pp. 102–137, 2020.
- [107] K. H. Zhao, “Regret-based algorithms for multi-armed bandits,” Ph.D. dissertation, 2020.
- [108] P. Auer, N. Cesa-Bianchi, and P. Fischer, “Finite-time analysis of the multi-armed bandit problem,” *Machine learning*, vol. 47, no. 2, pp. 235–256, 2002.
- [109] P. Auer, N. Cesa-Bianchi, Y. Freund, and R. E. Schapire, “The nonstochastic multi-armed bandit problem,” *SIAM journal on computing*, vol. 32, no. 1, pp. 48–77, 2002.
- [110] L. Kocsis and C. Szepesvári, “Discounted ucb,” in *2nd PASCAL Challenges Workshop*, vol. 2, 2006, pp. 51–134.
- [111] Y. Cao, Z. Wen, B. Kveton, and Y. Xie, “Nearly optimal adaptive procedure with change detection for piecewise-stationary bandit,” in *The 22nd International Conference on Artificial Intelligence and Statistics*, PMLR, 2019, pp. 418–427.
- [112] U. S. G. Survey, *Usgs real-time earthquake data*. [Online]. Available: <http://earthquake.usgs.gov/earthquakes/map/>.
- [113] E. Bacry, M. Bompairé, S. Gaïffas, and S. Poulsen, “Tick: A python library for statistical learning, with a particular emphasis on time-dependent modelling,” *arXiv preprint arXiv:1707.03003*, 2017.
- [114] J. G. Rasmussen, “Bayesian inference for hawkes processes,” *Methodology and Computing in Applied Probability*, vol. 15, no. 3, pp. 623–642, 2013.
- [115] G. O. Roberts, A. Gelman, W. R. Gilks, *et al.*, “Weak convergence and optimal scaling of random walk metropolis algorithms,” *The annals of applied probability*, vol. 7, no. 1, pp. 110–120, 1997.
- [116] C. Rasmussen and C. Williams, *Gaussian processes for machine learning the mit press*, 2006.
- [117] J. Møller and J. G. Rasmussen, “Perfect simulation of hawkes processes,” *Advances in applied probability*, vol. 37, no. 3, pp. 629–646, 2005.

- [118] K. Järvelin and J. Kekäläinen, “Cumulated gain-based evaluation of ir techniques,” *ACM Transactions on Information Systems (TOIS)*, vol. 20, no. 4, pp. 422–446, 2002.
- [119] G. Hripcsak and A. S. Rothschild, “Agreement, the f-measure, and reliability in information retrieval,” *Journal of the American Medical Informatics Association*, vol. 12, no. 3, pp. 296–298, 2005.
- [120] A. C. Miller, N. J. Foti, J. A. Lewnard, N. P. Jewell, C. Guestrin, and E. B. Fox, “Mobility trends provide a leading indicator of changes in sars-cov-2 transmission,” *medRxiv*, 2020.
- [121] A. L. Lloyd, “Destabilization of epidemic models with the inclusion of realistic distributions of infectious periods,” *Proceedings of the Royal Society of London. Series B: Biological Sciences*, vol. 268, no. 1470, pp. 985–993, 2001.
- [122] N. Imai, A. Cori, I. Dorigatti, M. Baguelin, C. A. Donnelly, S. Riley, and N. M. Ferguson, “Report 3: Transmissibility of 2019-ncov,” *Imperial College London*, pp. 1–6, 2020.
- [123] A. L. Bertozzi, E. Franco, G. Mohler, M. B. Short, and D. Sledge, “The challenges of modeling and forecasting the spread of covid-19,” *Proceedings of the National Academy of Sciences*, vol. 117, no. 29, pp. 16 732–16 738, 2020, ISSN: 0027-8424. DOI: [10.1073/pnas.2006520117](https://doi.org/10.1073/pnas.2006520117). eprint: <https://www.pnas.org/content/117/29/16732.full.pdf>. [Online]. Available: <https://www.pnas.org/content/117/29/16732>.
- [124] D. Marsan and O. Lengline, “Extending earthquakes’ reach through cascading,” *Science*, vol. 319, no. 5866, pp. 1076–1079, 2008.
- [125] D. Marsan and O. Lengliné, “A new estimation of the decay of aftershock density with distance to the mainshock,” *Journal of Geophysical Research: Solid Earth*, vol. 115, no. B9, 2010.
- [126] A. Veen and F. P. Schoenberg, “Estimation of space–time branching process models in seismology using an em–type algorithm,” *Journal of the American Statistical Association*, vol. 103, no. 482, pp. 614–624, 2008.
- [127] T. Obadia, R. Haneef, and P.-Y. Boëlle, “The r0 package: A toolbox to estimate reproduction numbers for epidemic outbreaks,” *BMC medical informatics and decision making*, vol. 12, no. 1, p. 147, 2012.
- [128] B. J. Cowling, M. S. Lau, L.-M. Ho, S.-K. Chuang, T. Tsang, S.-H. Liu, P.-Y. Leung, S.-V. Lo, and E. H. Lau, “The effective reproduction number of pandemic influenza: Prospective estimation,” *Epidemiology (Cambridge, Mass.)*, vol. 21, no. 6, p. 842, 2010.

- [129] J. Hellewell, S. Abbott, A. Gimma, N. I. Bosse, C. I. Jarvis, T. W. Russell, J. D. Munday, A. J. Kucharski, W. J. Edmunds, F. Sun, *et al.*, “Feasibility of controlling COVID-19 outbreaks by isolation of cases and contacts,” *The Lancet Global Health*, 2020.
- [130] E. Lewis and G. Mohler, “A nonparametric em algorithm for multiscale hawkes processes,” *Journal of Nonparametric Statistics*, vol. 1, no. 1, pp. 1–20, 2011.
- [131] F. P. Schoenberg, “Facilitated estimation of etas,” *Bulletin of the Seismological Society of America*, vol. 103, no. 1, pp. 601–605, 2013.
- [132] J. Wallinga and P. Teunis, “Different epidemic curves for severe acute respiratory syndrome reveal similar impacts of control measures,” *American Journal of epidemiology*, vol. 160, no. 6, pp. 509–516, 2004.
- [133] S. Cauchemez, P.-Y. Boëlle, C. A. Donnelly, N. M. Ferguson, G. Thomas, G. M. Leung, A. J. Hedley, R. M. Anderson, and A.-J. Valleron, “Real-time estimates in early detection of sars,” *Emerging infectious diseases*, vol. 12, no. 1, p. 110, 2006.
- [134] *The new york times*, *coronavirus in the u.s.: Latest map and case count*, Mar. 2020. [Online]. Available: <https://www.nytimes.com/interactive/2020/us/coronavirus-us-cases.html>.
- [135] E. Dong, H. Du, and L. Gardner, “An interactive web-based dashboard to track covid-19 in real time,” *The Lancet Infectious Diseases*, 2020.
- [136] Google, *Covid-19 community mobility report*, 2020. [Online]. Available: <https://www.google.com/covid19/mobility/>.
- [137] N. Altieri, R. L. Barter, J. Duncan, R. Dwivedi, K. Kumbier, X. Li, R. Netzorg, B. Park, C. Singh, Y. S. Tan, T. Tang, Y. Wang, C. Zhang, and B. Yu, “Curating a covid-19 data repository and forecasting county-level death counts in the united states,” *Harvard Data Science Review*, Feb. 8, 2021, <https://hdsr.mitpress.mit.edu/pub/p6isyf0g>. DOI: 10.1162/99608f92.1d4e0dae. [Online]. Available: <https://hdsr.mitpress.mit.edu/pub/p6isyf0g>.
- [138] E. L. Ray, N. Wattanachit, J. Niemi, A. H. Kanji, K. House, E. Y. Cramer, J. Bracher, A. Zheng, T. K. Yamana, X. Xiong, *et al.*, “Ensemble forecasts of coronavirus disease 2019 (covid-19) in the us,” *MedRxiv*, 2020.
- [139] J. Bracher, E. L. Ray, T. Gneiting, and N. G. Reich, “Evaluating epidemic forecasts in an interval format,” *PLoS computational biology*, vol. 17, no. 2, e1008618, 2021.

- [140] E. Y. Cramer, V. K. Lopez, J. Niemi, G. E. George, J. C. Cegan, I. D. Dettwiller, W. P. England, M. W. Farthing, R. H. Hunter, B. Lafferty, *et al.*, “Evaluation of individual and ensemble probabilistic forecasts of covid-19 mortality in the us,” *medRxiv*, 2021.
- [141] Y. Li, A. Hyder, L. T. Southerland, G. Hammond, A. Porr, and H. J. Miller, “311 service requests as indicators of neighborhood distress and opioid use disorder,” *Scientific reports*, vol. 10, no. 1, pp. 1–11, 2020.
- [142] Z. Yang, M. Kryven, H. Shrobe, and J. Tenenbaum, “Modeling human planning in a life-like search-and-rescue mission,” in *Proceedings of the Annual Meeting of the Cognitive Science Society*, vol. 43, 2021.
- [143] D. Shiri, V. Akbari, and F. S. Salman, “Online routing and scheduling of search-and-rescue teams,” *OR Spectrum*, vol. 42, no. 3, pp. 755–784, 2020.
- [144] R. A. Bolla, *Crime pattern detection using online social media*. Missouri University of Science and Technology, 2014.
- [145] H. Alvari and P. Shakarian, “Hawkes process for understanding the influence of pathogenic social media accounts,” in *2019 2nd International Conference on Data Intelligence and Security (ICDIS)*, IEEE, 2019, pp. 36–42.
- [146] J. Langford and T. Zhang, “The epoch-greedy algorithm for multi-armed bandits with side information,” *Advances in neural information processing systems*, vol. 20, 2007.
- [147] D. Bouneffouf, S. Upadhyay, and Y. Khazaeni, “Contextual bandit with missing rewards,” *arXiv preprint arXiv:2007.06368*, 2020.
- [148] S. Zhu, A. Bukharin, L. Xie, M. Santillana, S. Yang, and Y. Xie, “High-resolution spatio-temporal model for county-level covid-19 activity in the us,” *ACM Transactions on Management Information Systems (TMIS)*, vol. 12, no. 4, pp. 1–20, 2021.
- [149] M. Garetto, E. Leonardi, and G. L. Torrisi, “A time-modulated hawkes process to model the spread of covid-19 and the impact of countermeasures,” *Annual reviews in control*, vol. 51, pp. 551–563, 2021.
- [150] A. Schwabe, J. Persson, and S. Feuerriegel, “Predicting covid-19 spread from large-scale mobility data,” in *Proceedings of the 27th ACM SIGKDD Conference on Knowledge Discovery & Data Mining*, 2021, pp. 3531–3539.
- [151] S. Rambhatla, S. Zeighami, K. Shahabi, C. Shahabi, and Y. Liu, “Toward accurate spatiotemporal covid-19 risk scores using high-resolution real-world mobility data,” *ACM Transactions on Spatial Algorithms and Systems (TSAS)*, vol. 8, no. 2, pp. 1–30, 2022.

- [152] P. Wang, K. Liu, Y. Zhou, and Y. Fu, “Unifying human mobility forecasting and trajectory semantics augmentation via hawkes process based lstm,” in *Proceedings of the 2022 SIAM International Conference on Data Mining (SDM)*, SIAM, 2022, pp. 711–719.

VITA

Wen-Hao graduated from National Chiao Tung University and received his bachelor of science from the department of Electronic Engineering in 2012. He went ahead and received his master of science degree from the department of Electronic Engineering in National Taiwan University in 2014. He started to pursue his Ph.D. in the department of Computer Science in Indiana University–Purdue University Indianapolis in 2018.

PUBLICATIONS

1. W. Chiang, X. Liu, and G. Mohler, “Hawkes process modeling of covid-19 with mobility leading indicators and spatial covariates,” *International journal of forecasting*, 38(2), 505-520, 2022.
2. W. Chiang, B. Yuan, H. Li, B. Wang, A. Bertozzi, J. Carter, B. Ray and G. Mohler, “Sos-ew: System for overdose spike early warning using drug mover’s distance-based hawkes processes,” *Joint European conference on machine learning and knowledge discovery in databases*. Springer, Cham, 2019.
3. W. Chiang and G. Mohler. “Hawkes process multi-armed bandits for disaster search and rescue, ” preprint.